

AD-A184 888

PSI TR-379
DRAFT FORM

2

HARDENING MATERIALS TO REPETITIVELY PULSED LASERS

Final Report

Phase II

DNA SINGLE PULSE PROGRAM

For the Period

15 December 1982 - 15 December 1983

DTIC
ELECTE
SEP 16 1987
S D

Evan Pugh
G. Simons
G. Weyl
N. Kemp

May 1984

Submitted to

Naval Research Laboratory
Washington, D.C. 20375

Under Contract No. N00014-81-C-2394 - Modification P00006

DISTRIBUTION STATEMENT A

Approved for public release
Distribution Unlimited

PHYSICAL SCIENCES INC.

RESEARCH PARK, ANDOVER, MA 01810

PSI TR-379
DRAFT FORM

HARDENING MATERIALS TO REPETITIVELY PULSED LASERS

Final Report

Phase II

DNA SINGLE PULSE PROGRAM

For the Period

15 December 1982 -15 December 1983

Evan Pugh
G. Simons
G. Weyl
N. Kemp

March 1984

Submitted to

Naval Research Laboratory
Washington, D.C. 20375
Under Contract No. N00014-81-C-2394 - Modification P00006

Physical Sciences Inc.
Research Park, P.O. Box 3100
Andover, MA 01810

Unclassified

SECURITY CLASSIFICATION OF THIS PAGE

ADA184888

REPORT DOCUMENTATION PAGE

1a. REPORT SECURITY CLASSIFICATION Unclassified			1b. RESTRICTIVE MARKINGS		
2a. SECURITY CLASSIFICATION AUTHORITY			3. DISTRIBUTION/AVAILABILITY OF REPORT Approved for Public Release; Distribution Unlimited		
2b. DECLASSIFICATION/DOWNGRADING SCHEDULE					
4. PERFORMING ORGANIZATION REPORT NUMBER(S) PSI TR-379			5. MONITORING ORGANIZATION REPORT NUMBER(S)		
6a. NAME OF PERFORMING ORGANIZATION Physical Sciences Inc.		6b. OFFICE SYMBOL (If applicable)	7a. NAME OF MONITORING ORGANIZATION		
8a. ADDRESS (City, State and ZIP Code) Research Park, P.O. Box 3100 Andover, MA 01810			7b. ADDRESS (City, State and ZIP Code)		
9a. NAME OF FUNDING/SPONSORING ORGANIZATION Naval Research Laboratory		9b. OFFICE SYMBOL (If applicable) N/A	9. PROCUREMENT INSTRUMENT IDENTIFICATION NUMBER N00014-81-C-2394		
10a. ADDRESS (City, State and ZIP Code) Washington, D.C. 20375			10. SOURCE OF FUNDING NOS.		
			PROGRAM ELEMENT NO.	PROJECT NO.	TASK NO.
11. TITLE (Include Security Classification) HARDENING MATERIALS TO REPETITIVELY PULSED LASERS			P.R. 66-9302-83		
12. PERSONAL AUTHOR(S) Evan PUGH					
13a. TYPE OF REPORT Final Report		13b. TIME COVERED FROM 12/15/82 TO 12/15/83		14. DATE OF REPORT (Yr., Mo., Day) May 1984	
15. PAGE COUNT 111 pages					
16. SUPPLEMENTARY NOTATION					
17a. COSATI CODES			18. SUBJECT TERMS (Continue on reverse if necessary and identify by block number)		
FIELD	GROUP	SUB. GR.			
19. ABSTRACT (Continue on reverse if necessary and identify by block number) PSI, in support of the DNA single pulse program, considered the following four areas; plasma ignition, pressure at the wall, impulse and supersonic radiation waves. In all of these areas theory was compared with data with generally excellent agreement and the overall conclusion of this work is that the understanding of the phenomena important for single pulse damage in atmosphere is in hand. The data and conclusions of this work was presented in a timely manner throughout the program and it is the purpose of the report to bring it all together in a single volume.					
20. DISTRIBUTION/AVAILABILITY OF ABSTRACT Unclassified/Unlimited <input checked="" type="checkbox"/> SAME AS RPT. <input type="checkbox"/> DTIC USERS <input type="checkbox"/>			21. ABSTRACT SECURITY CLASSIFICATION Unclassified		
22a. NAME OF RESPONSIBLE INDIVIDUAL Dr. T.J. Wieting			22b. TELEPHONE NUMBER (Include Area Code) (202) 767-2101		22c. OFFICE SYMBOL NRL/Code 1232

SUMMARY

PSI, in support of the DNA single pulse program, considered the following four areas; plasma ignition, pressure at the wall, impulse and supersonic radiation waves. In all of these areas theory was compared with data with generally excellent agreement and the overall conclusion of this work is that the understanding of the phenomena important for single pulse damage in atmosphere is in hand.

The data and conclusions of this work was presented in a timely manner throughout the program and it is the purpose of the report to bring it all together in a single volume.



Accession For	
NTIS CRA&I	<input checked="" type="checkbox"/>
DTIC TAB	<input type="checkbox"/>
Unannounced	<input type="checkbox"/>
Justification	
By <i>per ttr</i>	
Distribution/	
Availability Codes	
Dist	Avail and/or Special
<i>A-1</i>	

TABLE OF CONTENTS

SUMMARY	PAGE i
LIST OF FIGURES	iii
1. PLASMA IGNITION - E. Pugh, G. Weyl	1
1.1 Laser Induced Breakdown of Grafoil™ Surfaces	5
1.2 Heating to Vaporization	5
1.3 Vaporization of Grafoil™	10
1.4 Breakdown of the Vapor	14
1.5 Breakdown Prediction for Experiments at NRL	21
PLASMA IGNITION REFERENCES	24
2. PRESSURE AT THE WALL - N. Kemp, E. Pugh	25
2.1 Calculation of Wall Pressure	29
2.2 Laser Absorption Coefficient	31
2.3 Equation of State	32
2.4 Laser Intensity	33
2.5 Model for High Temperature Air	35
PRESSURE AT THE WALL REFERENCES	42
3. IMPULSE SCALING - E. Pugh	43
IMPULSE SCALING REFERENCES	53
4. SUPERSONIC RADIATION WAVES - E. Pugh	55
4.1 Analysis of Streak Photograph Data	68
SUPERSONIC RADIATION WAVES REFERENCES	73
APPENDIX A SYMPTOTIC THEORY FOR THE MOMENTUM TRANSFER TO A SURFACE WHEN IRRADITIED BY A HIGH POWER LASER G. Simons	75

LIST OF FIGURES

Figure No.		Page
1.1	Theory for ignition of 10.6 μ radiation on Al	2
1.2	Summary of ignition data	3
1.3	Summary of ignition data	4
1.4	Pulse shape of ETI CO ₂ laser	6
1.5	Complex index of refraction of graphite	9
1.6	Surface temperature versus incident fluence	11
1.7	Geometry for vapor expansion	12
1.8	Composition of saturated carbon vapor	13
1.9	Mass flow rate versus surface temperature	15
1.10	Loss rate by vaporization and radiation	16
1.11	Inverse bremsstrahlung cross section in monatomic carbon vapor	18
1.12	Threshold fluence for breaking down the vapor	20
1.13	Steady state surface temperature and breakdown fluence as a function of laser intensity at focus	22
2.1	Laser intensity used in wall pressure calculation	26
2.2	Pressure vs time	27
2.3	Change in LSD wave pressure with velocity	28
2.4	Pressure vs time	30
3.1	Laser intensity used in wall pressure calculation	44
3.2	One-dimensional unsteady motion of a gas	46
3.3	Pressure behind spherical blast wave	47
3.4	Impulse Coupling 1.06 μ	50
3.5	Impulse Coupling 1.06 μ	51
3.6	Impulse Coupling 1.06 μ	52
4.1	Shock Hugonolt	58
4.2	Radiation forward drives wave	59
4.3	Supersonic radiation wave	61
4.4	Supersonic radiation wave	62
4.5	Theory and Experiment	63
4.6	Supersonic radiation wave	65
4.7	Supersonic radiation waves 10.6 μ	66
4.8	Theory and experiment 10.6 μ	67
4.9	Streak photographs	69
4.10	Distance vs velocity	70
4.11	-----	71
4.12	X at 200 ns versus velocity	72

1. PLASMA IGNITION

The ignition of a plasma over a target has been found to consist of two steps, the vaporizing of a small quantity of the target material followed by the breakdown of the vapor. The intensities are of course below the breakdown thresholds of clean air.¹ The production of aluminum vapor can arise from the heating of the bulk aluminum material and this is indicated in the theory plot of Fig. 1.1 by the line labeled bulk. This heating process in which the surface temperature is proportional to the intensity and the square root of the time $T \propto I/t$ when combined with the fact that $\phi = It$ for top hat pulses, leads to a criterion that $\phi I > 6 \times 10^8 \text{ J}^2/\text{cm}^4 \text{ s}$. The other mechanism for producing vapor that has been identified for aluminum is the vaporization of flakes, small thermally insulated pieces of aluminum lying on the aluminum surface. It has been found that 2 J/cm^2 is required to vaporize such small flakes,¹ (independent of intensity) and this point appears as the horizontal line labeled FLAKES in Fig. 1.1. The curves marked 1-D and 3-D refer to the breakdown in the vapor where it is seen that the time to breakdown the vapor is small compared to the time to generate the vapor at high intensities and can be neglected.

When the breakdown threshold curves are compared to the conditions obtainable in the present 10.6μ tests, Fig. 1.2, it is seen that the flake limit should prevail. There was considerable scatter in the results as an exact determination of the ignition time was quite difficult, however the data did tend to center around a value of 2 J/cm^2 , Fig. 1.3, indicating that flakes did indeed dominate the ignition process.

The situation for grafoil is less clear. The ignition times appear very similar to those on aluminum with an ignition on fluence of perhaps 4 J/cm^2 being more appropriate. Using a philosophy similar to that for aluminum, namely that the ignition process is dominated by the production of the vapor, this value is quite consistent with our estimates of the joules per cm^2 required to produce carbon vapor. However predictions of the time, and therefore energy, required to breakdown the vapor were not negligible as in the aluminum case, and the physical mechanisms responsible for the breakdown of the carbon vapor must be considered unknown at the present time. The details of PSI's examination of the problem are covered in the next section.

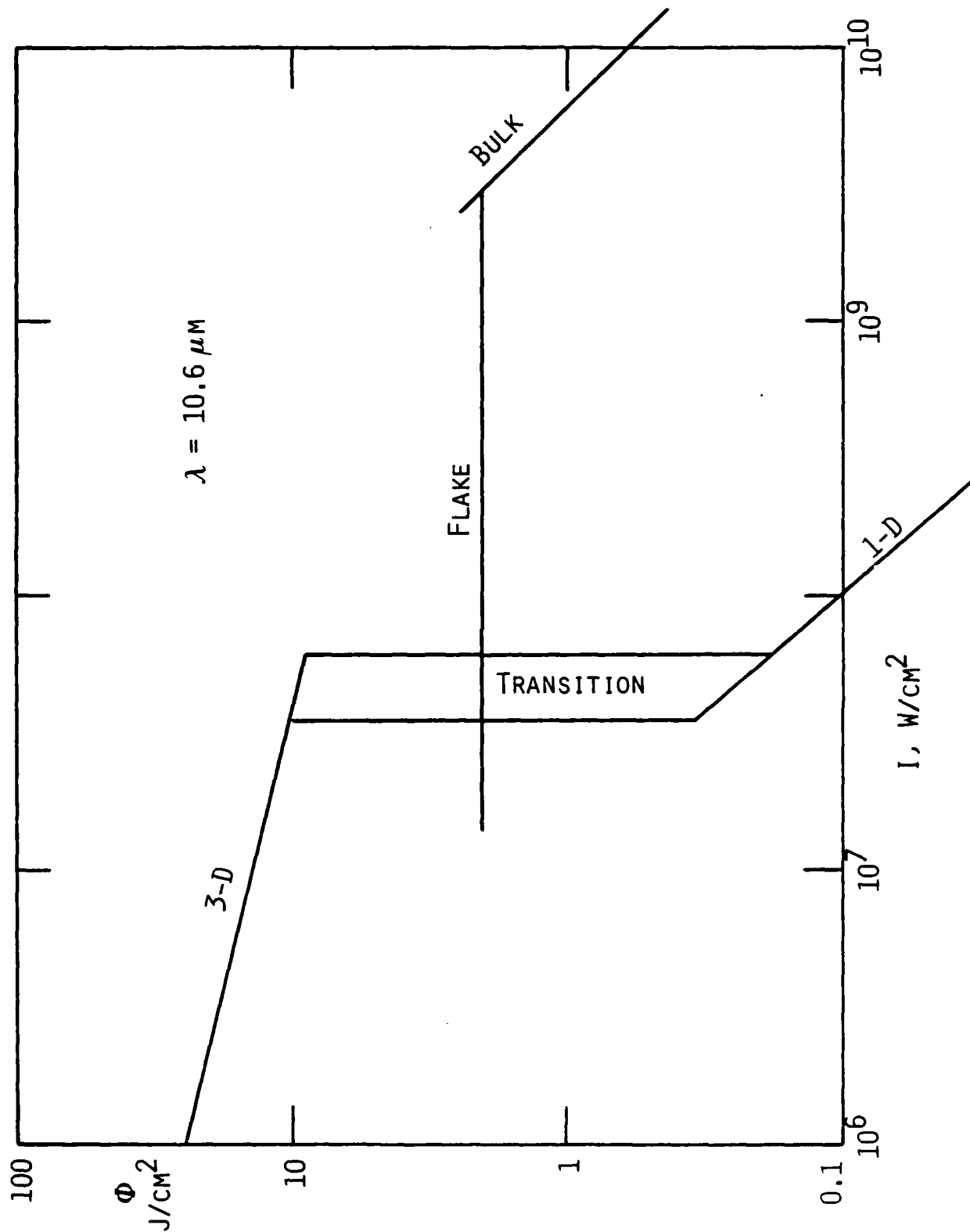


Fig. 1.1 Theory for ignition of 10.6 μ radiation on Al.

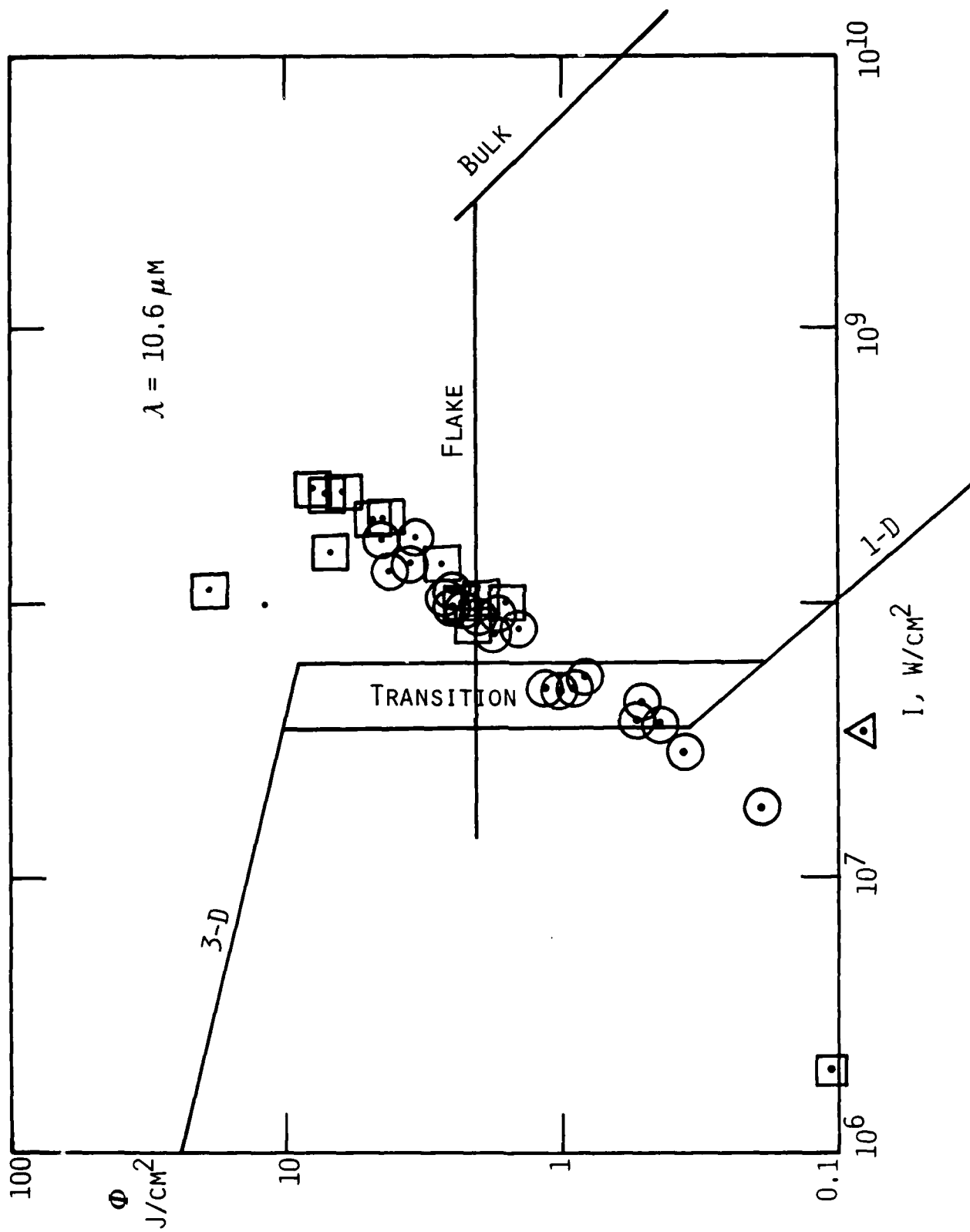


Fig. 1.2 Summary of ignition data.

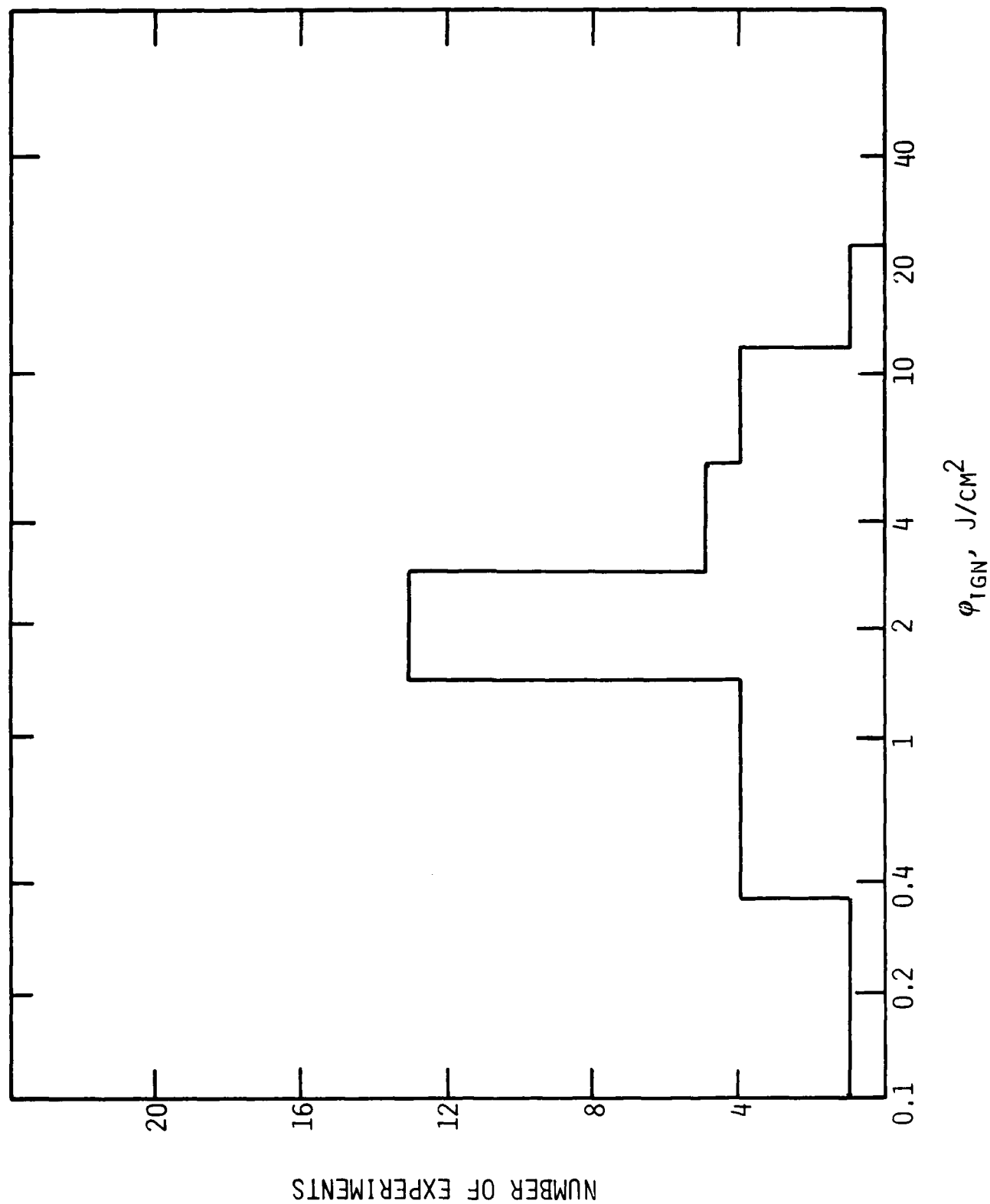


Fig. 1.3 Summary of ignition data.

1.1 Laser Induced Breakdown of Grafoil™ Surfaces

In this section, we predict the threshold intensity (or fluence) to cause breakdown above a Grafoil™ surface. The wavelength considered is 10.6 μm and the pulse shape, corresponding to the CO_2 laser used at NRL, is shown in Fig. 1.4.

Our model for breakdown is as follows. The laser energy absorbed in a small layer of Grafoil™ material below the surface results in a heating of this layer till vaporization occurs. The vapor that comes off the surface drives a shock into the air. We assume that breakdown occurs in the carbon vapor due to inverse bremsstrahlung absorption by the electrons in the vapor. This causes an increase in vapor temperature, which in turn causes an increase in the number density of electrons. Breakdown is assumed to have occurred if, by the end of the pulse, a critical ionization level has been achieved ($n_e/n > 1\%$). The work performed here is an extension to 10.6 μm of a model developed for shorter wavelengths ($\lambda = 1.06 \mu\text{m}$ and $\lambda = 0.35 \mu\text{m}$).² In Section 1.1, we analyze the heating of the material to vaporization. We then discuss in Section 1.2, the vapor properties before breakdown. Our vapor breakdown model is presented in Section 1.3 and results of specific calculations for the pulse shape shown in Fig. 1.4 are presented in Section 1.4.

1.2 Heating to Vaporization

The response of the solid material to laser radiation, in the absence of radiation and vaporization losses is given by the heat conduction equation

$$\rho \frac{C}{\partial t} \frac{\partial T}{\partial x} = \frac{\partial}{\partial x} \left(K \frac{\partial T}{\partial x} \right) + \frac{(1 - R)}{\ell} I e^{-x/\ell} \quad (1.1)$$

where ρ , C and K are the density, specific heat and thermal conductivity of the material, I is the incident laser intensity, T is the temperature, R is the surface reflectivity and ℓ the absorption length in the material.

Grafoil™ is a form of graphite in which thin lamellae of graphite layers composed of microscopic crystals all having their c axis perpendicular to the lamellae are pressure bonded to each other. Though pure graphite has a

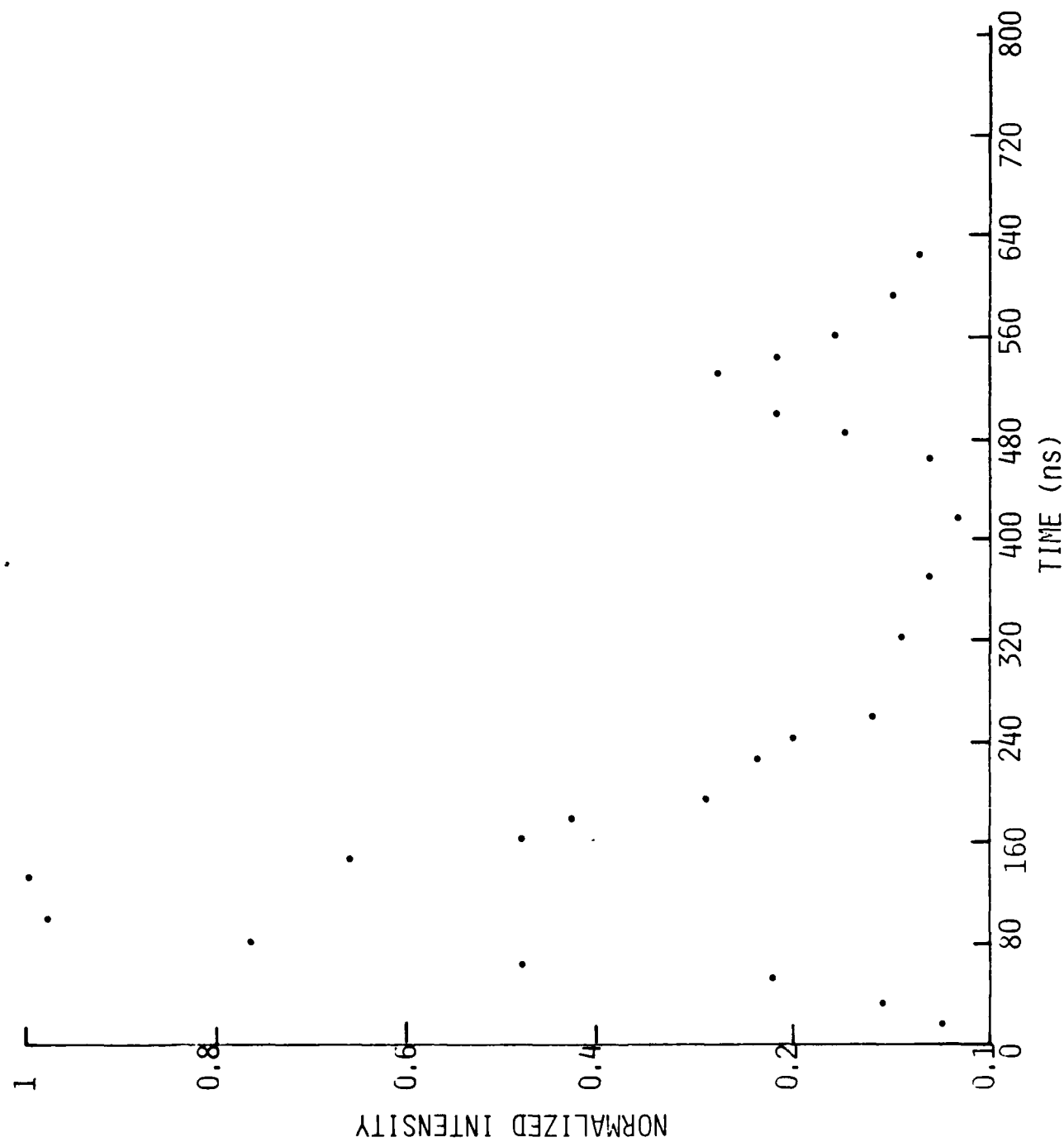


Fig. 1.4 Pulse shape of ETI CO₂ laser.

density of 2.2 g/cm³, the density of Grafoil™ is a factor of two lower due to the voids between lamellae. The thermal properties of Grafoil™ are shown in Table 1.1. We have also shown in this table the thermal properties of a pure graphite single crystal, as well as the properties of commercial grade polycrystalline ATJ Graphite, which is actually a composite of micro crystals with preferred orientation due to the forming process. Note that a single graphite crystal has a thermal conductivity in the a direction that is one hundred times that in the c direction and that is comparable to the thermal conductivity of a metal. Thermal conductivity of bulk graphite, which is composed of many crystals, is less anisotropic. The conductivity of Grafoil™ in the direction normal to the lamellae, is much smaller than that of monocrystalline graphite in the c direction due to the voids between lamellae.

A simplification of Eq. (1.1) can be obtained by comparing the thermal diffusion length $\ell_D = [K \tau_p / (\rho c)]^{1/2}$ during the pulse time (τ_p) to the absorption length ℓ . If $\ell_D \ll \ell$ then thermal conduction during the pulse is negligible and the temperature at any time during the pulse, obtained by integration of Eq. (1.1), is:

$$\int_{T_0}^T \rho(T) C(T) dT = \frac{(1-R)}{\ell} e^{-x/\ell} \int_0^t I dt'$$

or

$$h(T(x)) = h(T_0) + \frac{1-R}{\rho \ell} e^{-x/\ell} \Phi(t) \quad (1.2)$$

where h is the enthalpy per unit mass, Φ the incident fluence and when we neglected variation of absorption length and reflectivity with temperature. Equation (1.2) can readily be solved to obtain T as a function of Φ . We show in Fig. 1.5 the complex index of refraction of graphite as measured by Foster and Howarth.³ Extrapolating the curves up to $\lambda = 10.6 \mu\text{m}$, we find $n = n_1 + in_2 = 3.9 + i 0.7$ from which we calculate the reflection coefficient

$$R = \frac{(n_1 - 1)^2 + n_2^2}{(n_1 + 1)^2 + n_2^2} = 0.36$$

TABLE 1.1
Thermal Properties of Graphite

Material	ρ (g/cm ³)	C (J/gK)	K_C W/(cm K)	K_a W/(cm K)
Grafoil [†]	1.1	1.8	0.03	0.42
Polycrystalline ATJ [†] Graphite	2.2	1.8	0.3	0.4
Graphite Single* Crystal	2.2	0.7 (T=300 K) 2 (T = 1000°C)	0.08	20.0

[†]Union Carbide Data Sheet, T = 1100°C

[†]Touloukian, page 1, T = 1100°C

*A. J. deCombarieu, J. Phys. (France) 28, 931 (1968)

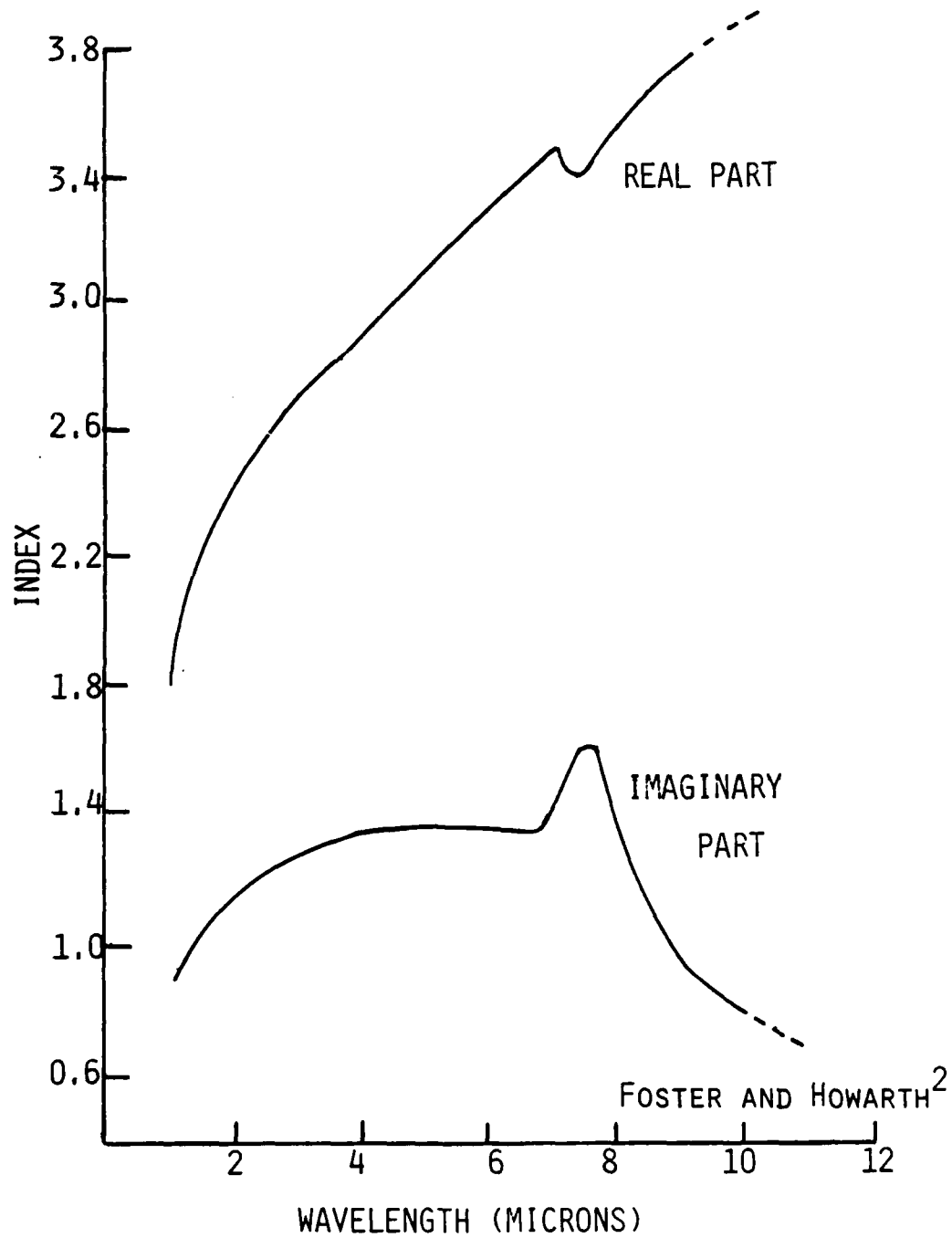


Fig. 1.5 Complex index of refraction of graphite.

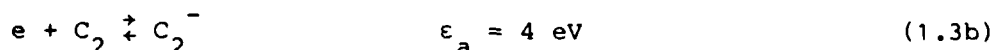
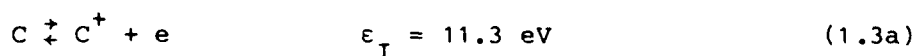
and the absorption length

$$\ell = \lambda / (4\pi n_2) = 1.2 \text{ } \mu\text{m} \quad .$$

This length is to be compared with the diffusion distance during the pulse ℓ_D . Taking $\tau_p = 2 \times 10^{-7}$ s and considering a monocrystal near the surface, we find in the c direction $\ell_D = 0.14 \text{ } \mu\text{m}$ and in the a direction $\ell_D = 1.2 \text{ } \mu\text{m}$. If the lateral (i.e., in the a direction parallel to the surface) dimensions of the micro crystals exceed a few microns the response of Grafoil™ during the laser pulse will be the same as that of an aggregate of microcrystals that are uncoupled from each other. The main point to be made here, however, is that whatever thermal conductivity we choose in the c direction (normal to the surface), we will have $\ell_D \ll \ell$ so that Eq. (1.2) holds. The surface temperature reached by the Grafoil™ is shown in Fig. 1.6 as a function of incident fluence, using $\ell = 1.2 \text{ } \mu\text{m}$, $R = 0.4$ and tabulated values of C for graphite. An incident fluence of 3.3 J/cm^2 is required to heat the surface to $T = 4000 \text{ K}$ at which point the vapor pressure reaches 1 atm.

1.3 Vaporization of Grafoil™

Once the vapor pressure above the surface exceeds 1 atm (i.e., $T_s > 4000 \text{ K}$), the carbon vapor that leaves the surface drives a shock into the air. We will have a situation as shown in Fig. 1.7. Zone 1 is the region of shocked air. Zone 2 is the region where the vapor is expanding at a uniform velocity \vec{u} away from the surface and is in pressure equilibrium with the shocked air. Zone 3 is the Knudsen layer where the half Maxwellian distribution in velocity space of particles leaving the surface is converted into a full Maxwellian centered around \vec{u} . We use the model developed by C. Knight^{5,6} to solve for the mass flow rate as a function of surface temperature T_s . The initial composition of the vapor as a function of T_s is assumed to be the same as that of saturated vapor at T_s and is obtained by use of a chemical equilibrium code that uses the JANAF thermochemical properties of the vapor constituents. We show the concentration of the vapor species in Fig. 1.8. The electron concentration is given by the balance of the two reactions:



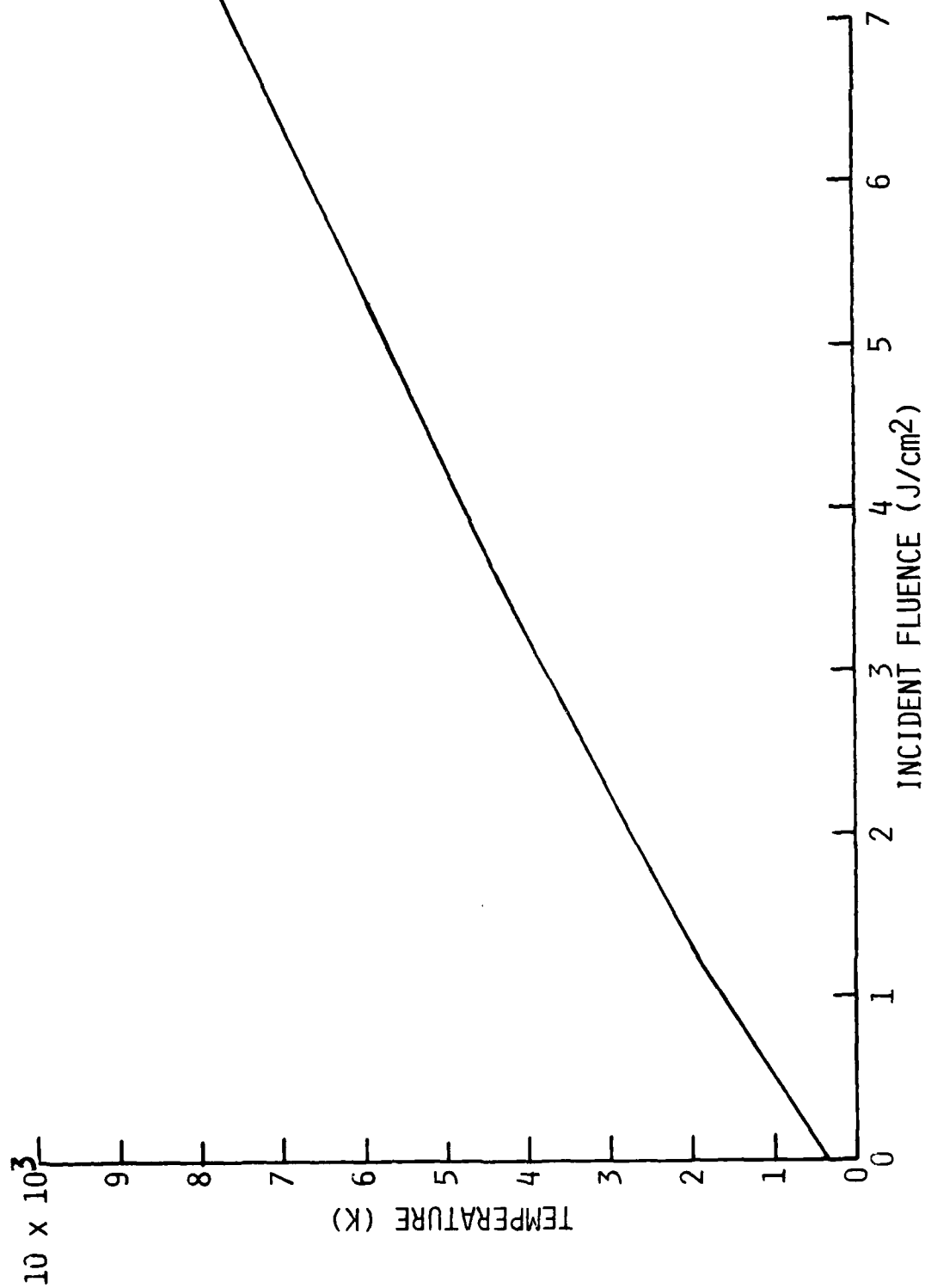


Fig. 1.6 Surface temperature versus incident fluence.

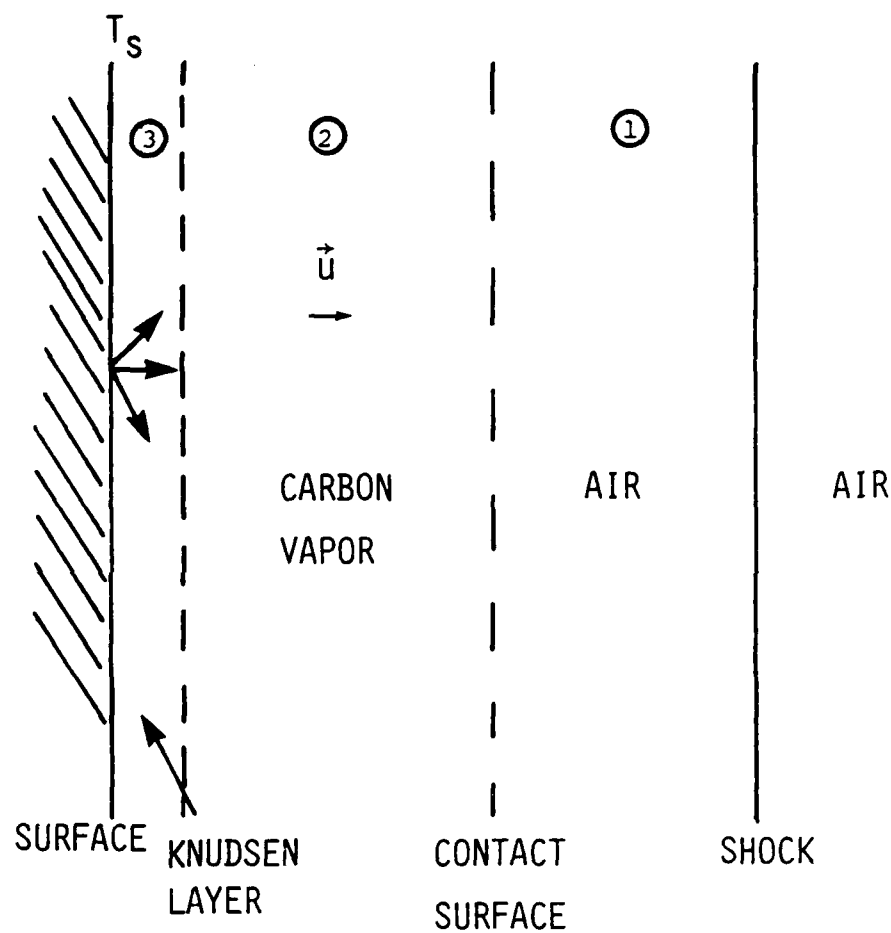


Fig. 1.7 Geometry for vapor expansion.

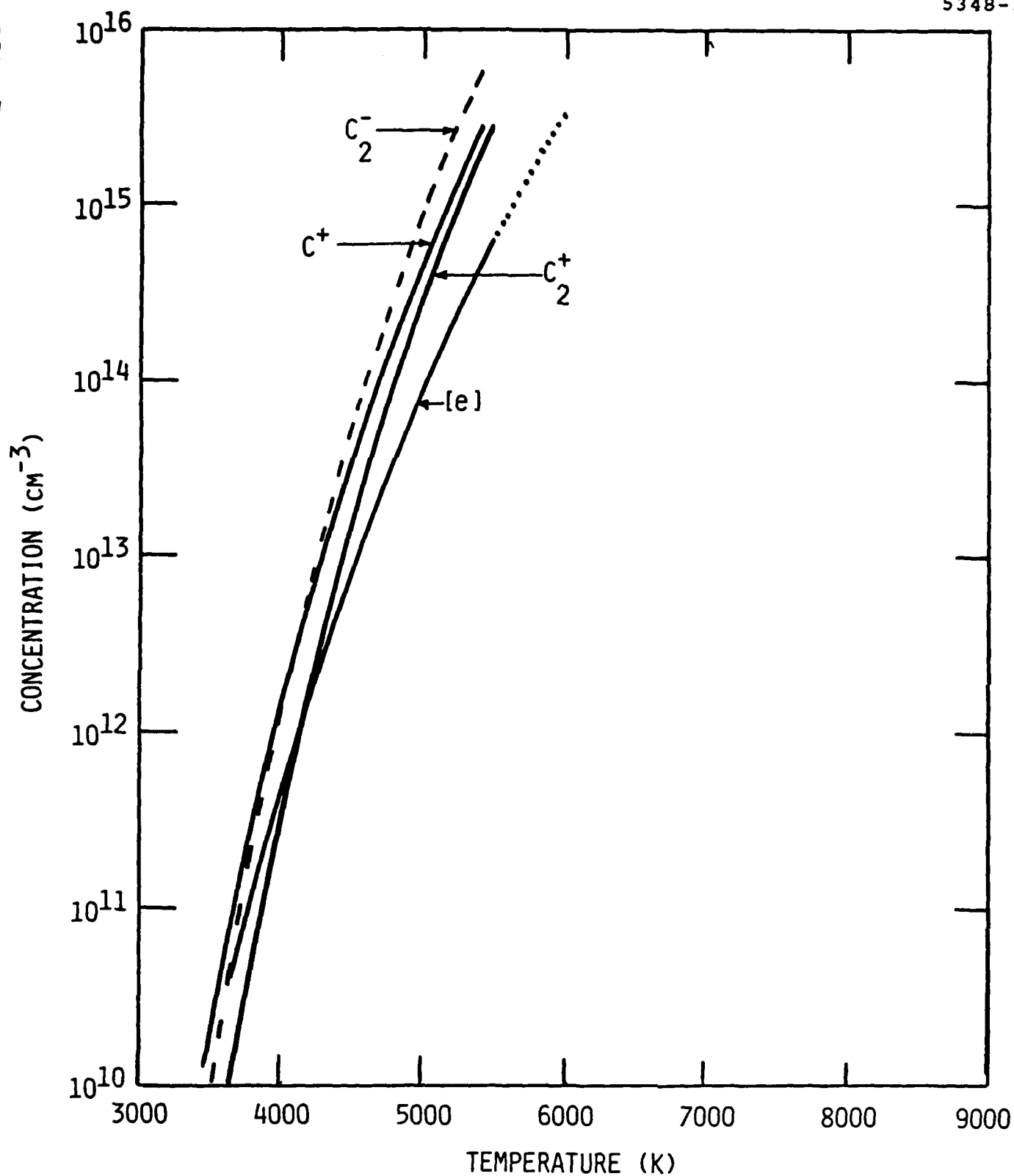


Fig. 1.8 Composition of saturated carbon vapor.

n_e , the electron density, is well approximated over the temperature range studied by the relation¹

$$n_e = 3.2 \times 10^{16} T^{3/2} \exp(-92,800/T) \quad (1.4)$$

The vapor blowing rate \dot{m} was obtained by solving the Knudsen layer and continuity equations given by C. Knight.⁵ A computer program that solves these equations was developed at PSI by Les Popper.² We show the results in Fig. 1.9. The γ of the vapor was taken to be 1.2 and the saturated vapor pressure was taken to be

$$p(T_s) = 9 \times 10^9 \exp(-94,000/T_s) \quad \text{atm}.$$

The vapor chokes and the flow becomes supersonic when the temperature exceeds 5100 K.

In the absence of laser induced breakdown in the vapor (causing absorption of the laser beam by the vapor), the surface temperature eventually reaches an asymptotic value for which the rate of enthalpy loss by vaporization balances the power absorbed from the laser beam at the surface. We have plotted this rate of enthalpy loss by multiplying the mass loss rate \dot{m} , shown in Fig. 1.9, by $(\Delta h_v + \int C_d T')$ where Δh_v is the heat of vaporization (~23 kJ/g) and $\int C_d T'$ the enthalpy rise in the solid to reach the vaporization temperature. This power loss rate is shown in Fig. 1.10. We have also plotted in Fig. 1.10 the radiative losses from the surface (which are several orders of magnitude lower).

1.4 Breakdown of the Vapor

The electrons absorb laser radiation due to inverse bremsstrahlung collisions with the neutrals. At sufficiently high laser fluence some electrons may gain a sufficient amount of energy that upon impact they can ionize the vapor leading to avalanche ionization. A proper calculation of the ionization rate would involve numerical solution of the Boltzman equation. The cross sections for the various inelastic processes in carbon are however unknown. Because the saturated vapor above a carbon target is mainly composed

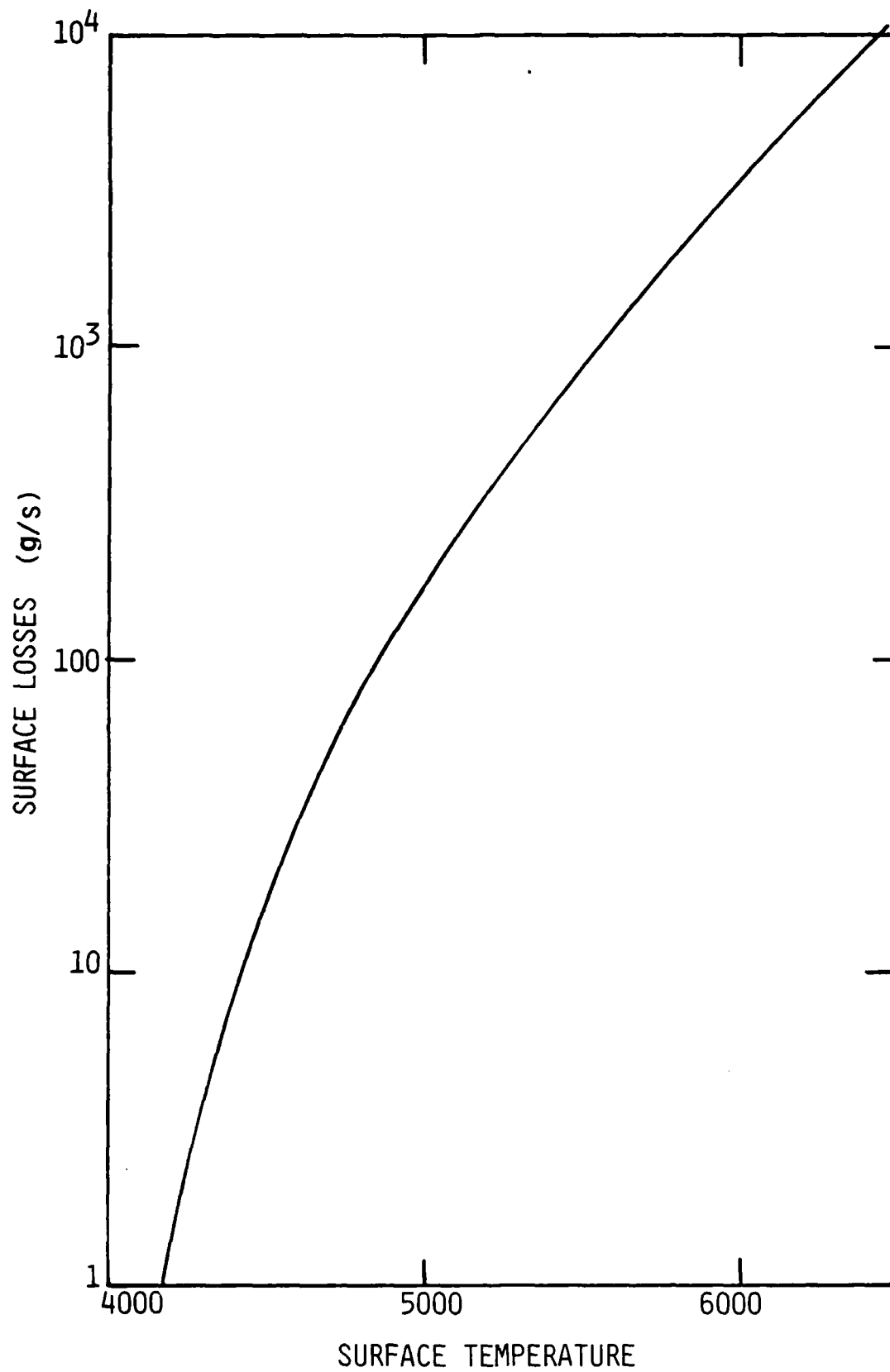


Fig. 1.9 Mass flow rate versus surface temperature.

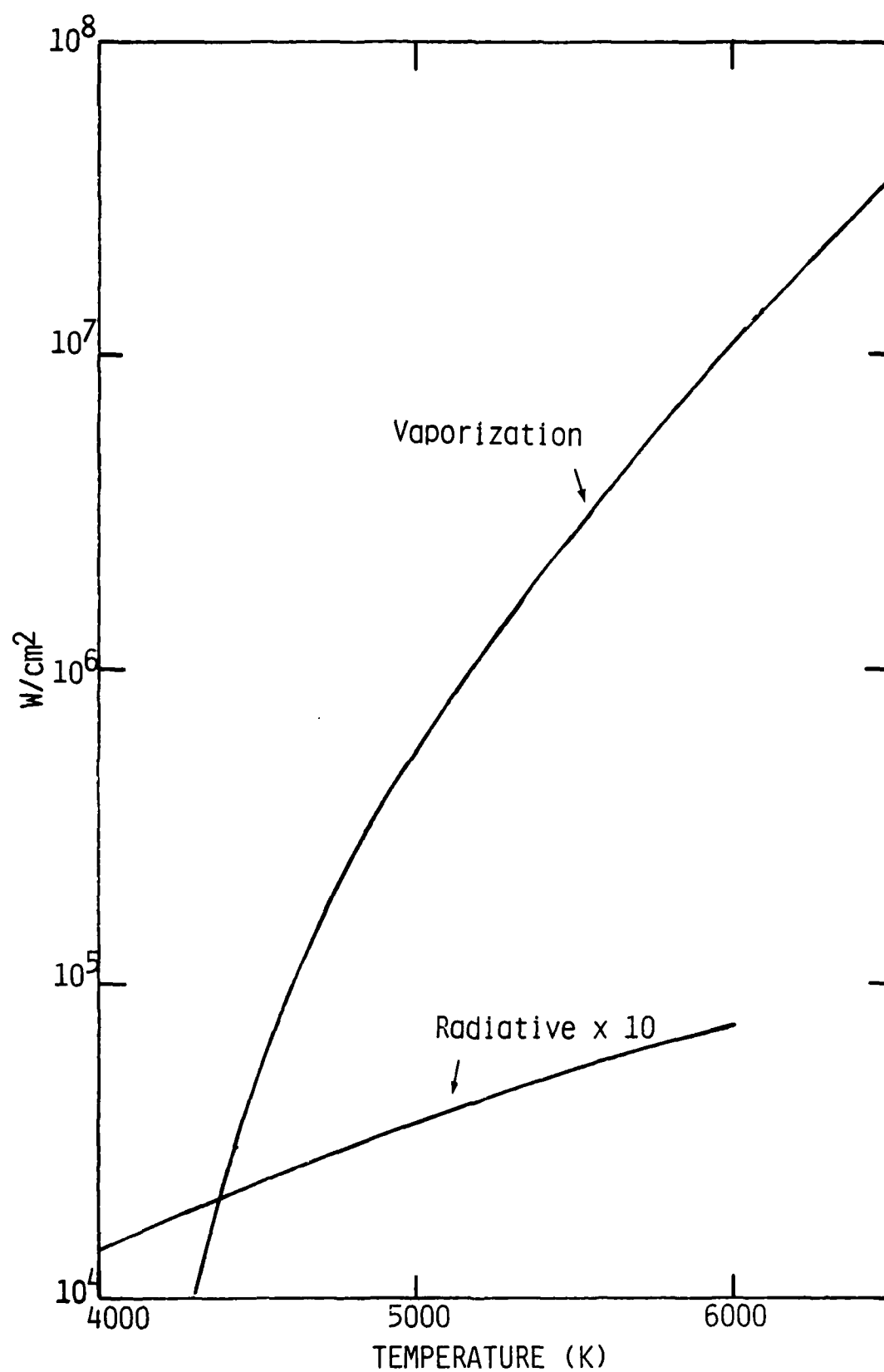


Fig. 1.10 Loss rate by vaporization and radiation.

of molecules and because the effective ionization potential of carbon ($\epsilon_I + \epsilon_a = 15.3$ eV) is close to that of N_2 ($\epsilon_I = 15.9$ eV) we believe that laser induced breakdown of carbon will not differ too significantly from that of nitrogen and oxygen, the breakdown thresholds of which are known. Even though the vapor is hot, super-elastic collisions will not lower the threshold significantly below room temperature values since $kT \ll \epsilon_I, \epsilon_a$. The effect of super-elastic collisions in N_2 has been studied by making electron distribution predicts 5000 K, taking into account super-elastic collisions. We found the threshold at $T = 5,000$ K to differ insignificantly from the room temperature value of 3×10^9 W/cm².

Based on the above arguments, we model the breakdown of the vapor at laser fluxes below 10^9 W/cm² as a heating of the vapor through inelastic and elastic collisions of vapor molecules/atoms with electrons. The electrons, as we mentioned above, get heated by inverse bremsstrahlung absorption. The absorption coefficient for collisions with carbon atoms has been calculated by Geltman⁷ and we show his results in Fig. 1.8. Due to the large number of lower lying electronic states of carbon and to energy losses in excitation of rotational and vibrational degrees of freedom of the gas, we consider that the electron temperature does not depart significantly from the vapor temperature. This assumption should be well verified at fluxes below 10^8 W/cm². We consider that the electron concentration is initially that given by using Saha equilibrium in the saturated vapor. We can neglect recombination of electrons with ions during the expansion through the Knudsen layer when the electron density is below 10^{14} cm⁻³ (i.e., $T_s < 5000$ K) because the three body recombination rate is small. At higher densities, we will also neglect recombination because the laser beam will always maintain $T_e > T_g$. The heating of the gas is given by the following relation.

$$n \bar{m} c_v \frac{dT}{dt} = \chi(1 - e^{-h\nu/kT}) n_e n I(1 + R) \quad (1.5)$$

where \bar{m} is the average molecular weight. The absorption cross section (corrected for stimulated emission) $\chi(1 - e^{-h\nu/kT})$ is plotted in Fig. 1.11. We assume that the electron concentration is given by the Saha equation

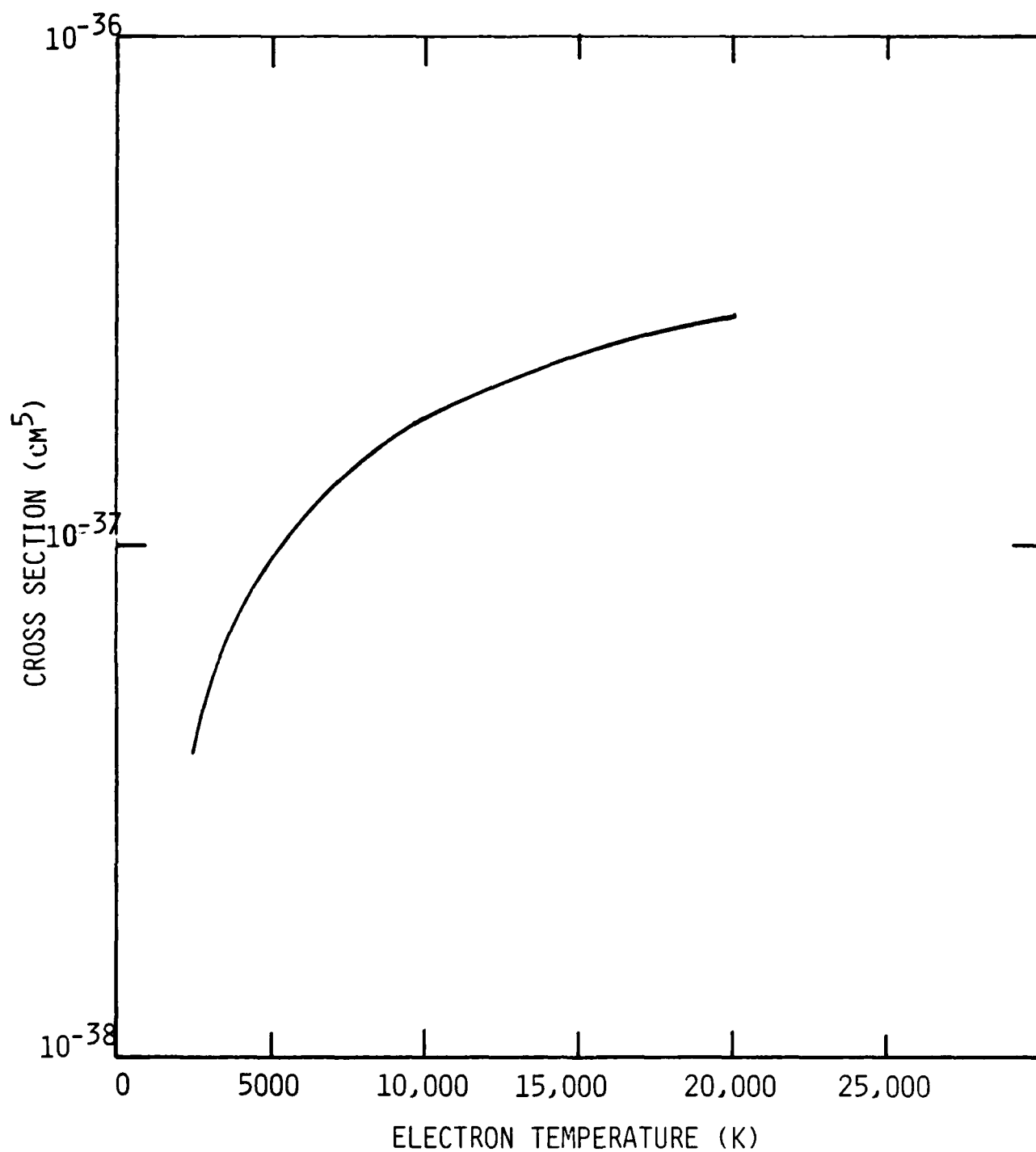


Fig. 1.11 Inverse bremsstrahlung cross section in monatomic carbon vapor.

$$\frac{n_e^2}{n} = AT^{3/2} e^{-(\epsilon_I + \epsilon_a)/kT}. \quad (1.6)$$

where we have added to the ionization potential ϵ_I the attachment energy ϵ_a because of the second reaction (1.3b). It can be shown⁶ that the breakdown time is equal to the time it takes to e-fold the electron density once, assuming equilibrium gas properties. Taking the leading term of the logarithmic derivative of n_e from Eq. (1.6), we obtain

$$\frac{d n_e}{n_e} = \frac{\epsilon_I + \epsilon_a}{2 kT^2} dT$$

Then setting $d n_e/n_e = 1$, we obtain the temperature rise necessary for one e-fold in electron density and inserting this into Eq. (1.5) we find

$$\tau_{VB} = \frac{2(kT)^2}{(\gamma - 1)(\epsilon_I + \epsilon_a)\chi(1 - e^{-h\nu/kT}) n_e(1 + R)I} \quad (1.7)$$

We evaluate Eq. (1.7) using the following values of the parameters:

$$\chi(1 - e^{-h\nu/kT}) = 10^{-37} \left(\frac{T}{5000}\right)^{0.8} \text{ cm}^5$$

$$R = 0.4$$

$$\gamma = 1.16$$

$$\epsilon_I + \epsilon_a = 15.3$$

$$\epsilon_I = 13 \text{ eV} =$$

$$n_e = \eta n_{e0} = 3.2 \times 10^{16} \eta T_s^{3/2} \exp(-92,800/T_s)$$

where η is the density decrease ($\eta = n_e/n_{e0}$) through the Knudsen layer which has the lower bound of 0.3 when the flow is choked ($T_s > 5000 \text{ K}$). We find

$$\phi_{VB} = I\tau_{VB} = \frac{1.4 \times 10^{-5}}{\eta} \left(\frac{T_s}{5000}\right)^{-0.3} \exp\{18.5(\frac{5000}{T_s})\} \text{ J/cm}^2 \quad (1.8)$$

The threshold flux for breaking down the vapor as a function of surface temperature is plotted in Fig. 1.12.

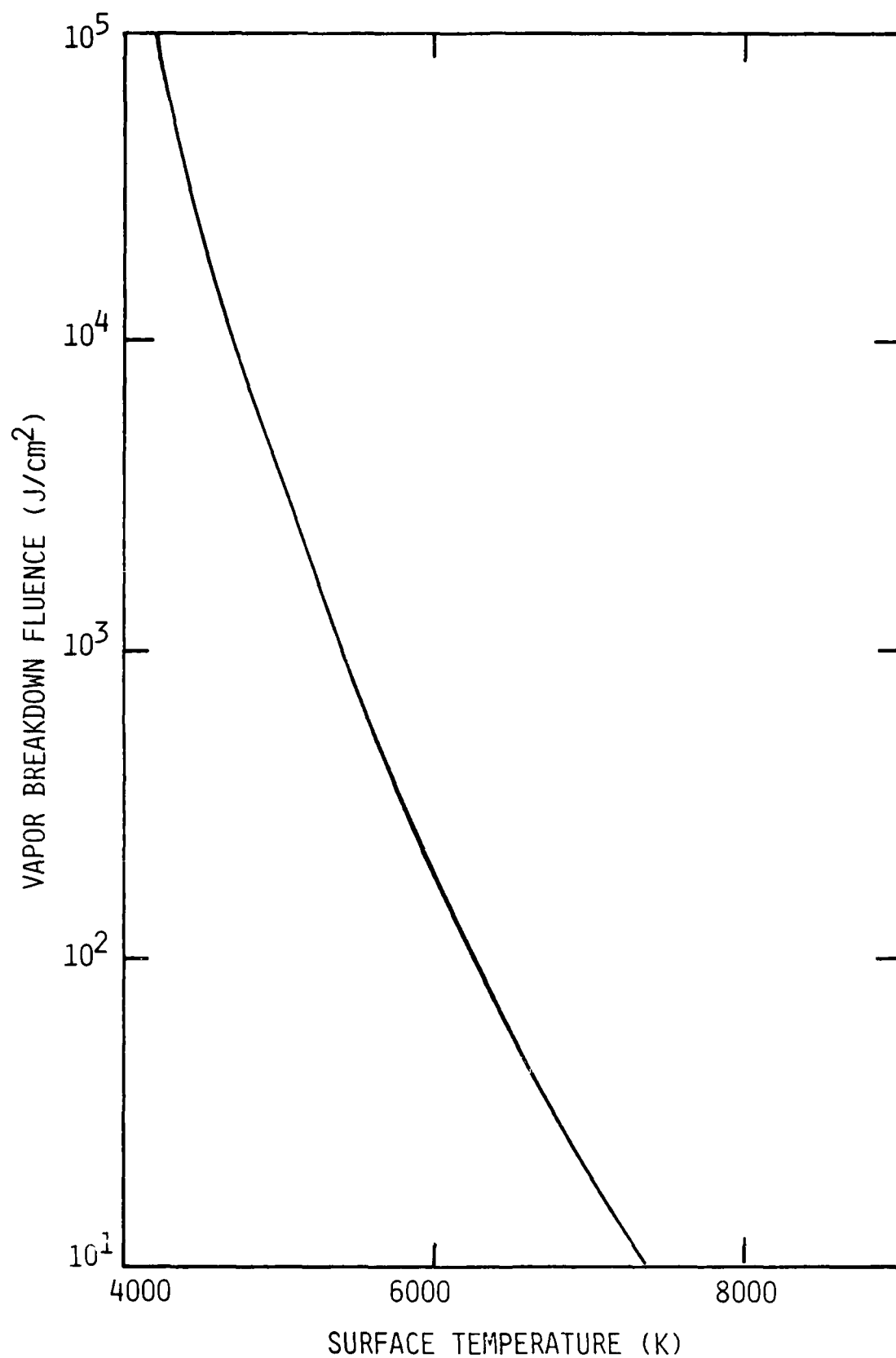


Fig. 1.12 Threshold fluence for breaking down the vapor.

1.5 Breakdown Prediction for Experiments at NRL

We are now in a position to make breakdown predictions for the pulse shape shown in Fig. 1.4. The thresholds for breakdown that we present in this section were calculated as follows. A fluence ϕ_1 , given by Eq. (1.2), is required to raise the surface of the Grafoil[™] to T_s and an extra fluence $\phi_{VB}(T_s)$ given by Eq. (1.8) is required to breakdown the vapor. The total fluence to breakdown is thus

$$\phi_{TOT} = \phi_H + \phi_{VB}(T_s) \quad (1.9)$$

Given the pulse profile and the peak intensity in the pulse I_p , it is straightforward to calculate when in the pulse a total fluence ϕ_{TOT} has been delivered and therefore to calculate the time to breakdown. The fluence ϕ in Eq. (1.9), however, must be treated as a parameter because during the pulse, as ϕ increases, the vapor is coming off at higher and higher pressures and temperatures, so that as T_s increases, $\phi_{VB}(T_s)$ decreases (see Fig. 1.9). We have therefore solved for the minimum value of ϕ_{TOT} as ϕ_1 is varied in Eq. (1.9). This gives us a minimum breakdown time as a function of I_p (or of total pulse fluence which is proportional to I_p). As I_p is decreased from some large value, we find that breakdown occurs later and later in the pulse till below some threshold I_{th} we cannot find a solution. Our results are shown in Fig. 1.13, as a function of peak intensity, I_p , in the pulse. The main assumption made in specifying Fig. 1.13 is that the rise in intensity to $I = I_p$ occurs fast enough that vaporization losses can be neglected during the rise time. The steady state temperature that the surface would reach if I remained constant during the pulse is shown in Fig. 1.13a. The incident fluence, ϕ_H , required to heat the surface to T_s is shown in Fig. 1.13b and is in the 4 to 6 J/cm² over the intensities of interest. The additional fluence ϕ_{VB} required to breakdown the vapor leaving the surface at T_{ss} is also plotted in Fig. 1.13b. The sum $\phi_H + \phi_{VB}$ becomes less than the pulse fluence when $I_p > 4 \times 10^8$ W/cm² and this occurs at a pulse fluence of 65 J/cm².

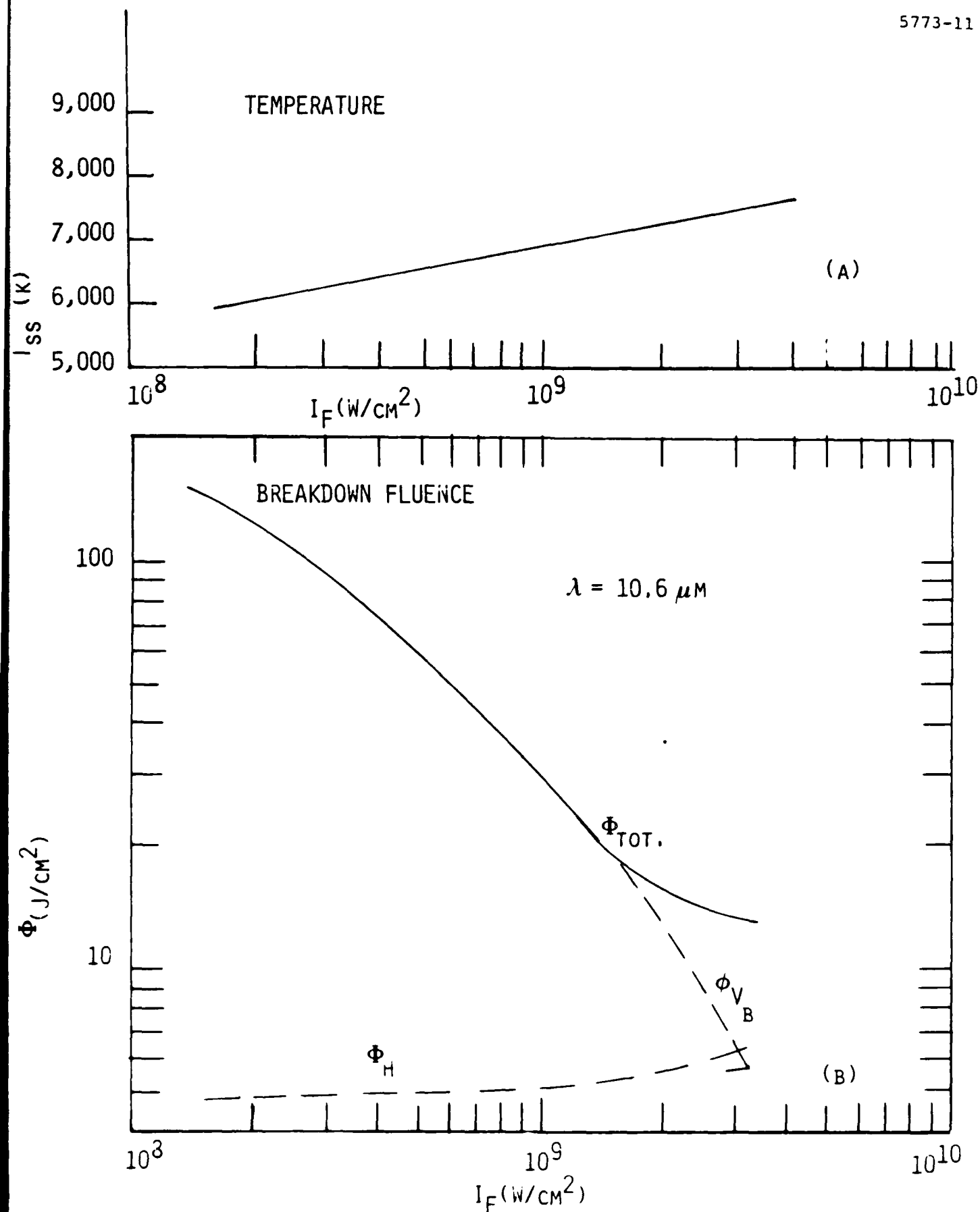


Fig. 1.13 Steady state surface temperature and breakdown fluence as a function of laser intensity at focus. (A) Steady state temperature of surface. B) fluence to breakdown.

Our theoretical estimate is to be compared with an experimentally observed threshold of 2×10^8 W/cm² and pulse fluence of 5 J/cm². A factor of two difference in peak intensity may arise from the poor measurement of laser pulse profile since a gain switch spike a factor of two higher than the measured peak may well be apparent with a faster detector. The larger factor observed in impulse fluence to breakdown cannot be explained in this manner. We have used a theoretical inverse Bremsstrahlung absorption cross section calculated by Geltman for monatomic carbon. The main species in the vapor is C₃ and it is not inconceivable that the cross section could be a factor of 3 higher or more. If we increase the cross section by a factor of three we now calculate for $I_p = 4 \times 10^8$ W/cm², a breakdown fluence $\phi_{VBr} = 17$ J/cm² and $\phi_H + \phi_{VBr} = 22$ J/cm² in much better agreement with the data. Note also that we gave extended saturated vapor pressure data to temperatures and pressures well beyond the range where the thermodynamic data has been measured.

PLASMA IGNITION
REFERENCES

1. Weyl, G., Pirri, A., Root, R., "Laser Ignition of Plasma off Aluminum Surfaces," AIAA Journal, 19,4, April 1981, p. 460.
2. Weyl, G. and Popper, L., "Addendum to: Laser Induced Breakdown Studies at 1.06 μm and 0.35 μm " PSI TR-320, Physical Sciences Inc., Research Park, P. O. Box 3100, Andover, MA 01810
3. Foster, P. J. and Howarth, C. R., Carbon 6, 719 (1968).
4. JANAF Thermochemical Tables
5. C. Knight, AIAA J. 17, 519, (1979).
6. Pirri, A., "Analytical Solution of Plasma Absorption above Laser Irradiated Surfaces," PSI TR-15 (1974).
7. Geltman S., J. Quant. Spectroscop. Radiat. Transfer 13, 601 (1973).

2. PRESSURE AT THE WALL

Lindberg¹ showed that the damage to re-entry vehicles depends upon both the impulse and the impulse per unit area, the later being the integral over-time of the peak pressure. In the simplest of cases this pressure is determined by LSD shock wave jump conditions during the laser pulse followed by an expansion first in one and then in three-dimensions.

Measurements of this pressure during the present test series were complicated by the effects of a finite ignition time and a time varying intensity. The issue was further complicated by the high intensities used which produced shock waves in which radiation was important, and this also affected the pressure and its time history. The details of this early time history determine the impulse per unit area and are thus important for damage.

The PSI code LSDNS calculates the quasi-one-dimensional non-steady flow with laser heat addition and real gas effects. It does not include radiation transport and therefore cannot make the transition to radiation-driven waves expected at the highest intensities. It has been used to determine the effects of the finite ignition time and the time varying intensity on the pressure measured at the wall.

The time history of the laser pulse is shown in Fig. 2.1. The pressure behind the shock wave P_s and the pressure at the wall P_w are shown in Fig. 2.2. The difference between these two pressures, a factor of 3, is in good agreement with what would be expected from simple theory; $(P_w/P_s = (\gamma+1/2\gamma)2\gamma/\gamma-1 = .35$ where $\gamma = 1.2)$, and indicates that the variation of intensity with time has little effect on the peak pressure at the wall. However the measured pressures are somewhat lower and might be indicative of the importance of radiation on the wave.

The effect of radiation is to produce higher wave velocities than would be predicted using a LSD wave criteria and this is discussed in more length in the section on Supersonic Radiation Waves. The effect of a higher wave velocity is a lower pressure behind the wave and this is illustrated in Fig. 2.3. It is important to note that the fall off in pressure behind the is to some extent compensated for by the decrease in the pressure ratio be-

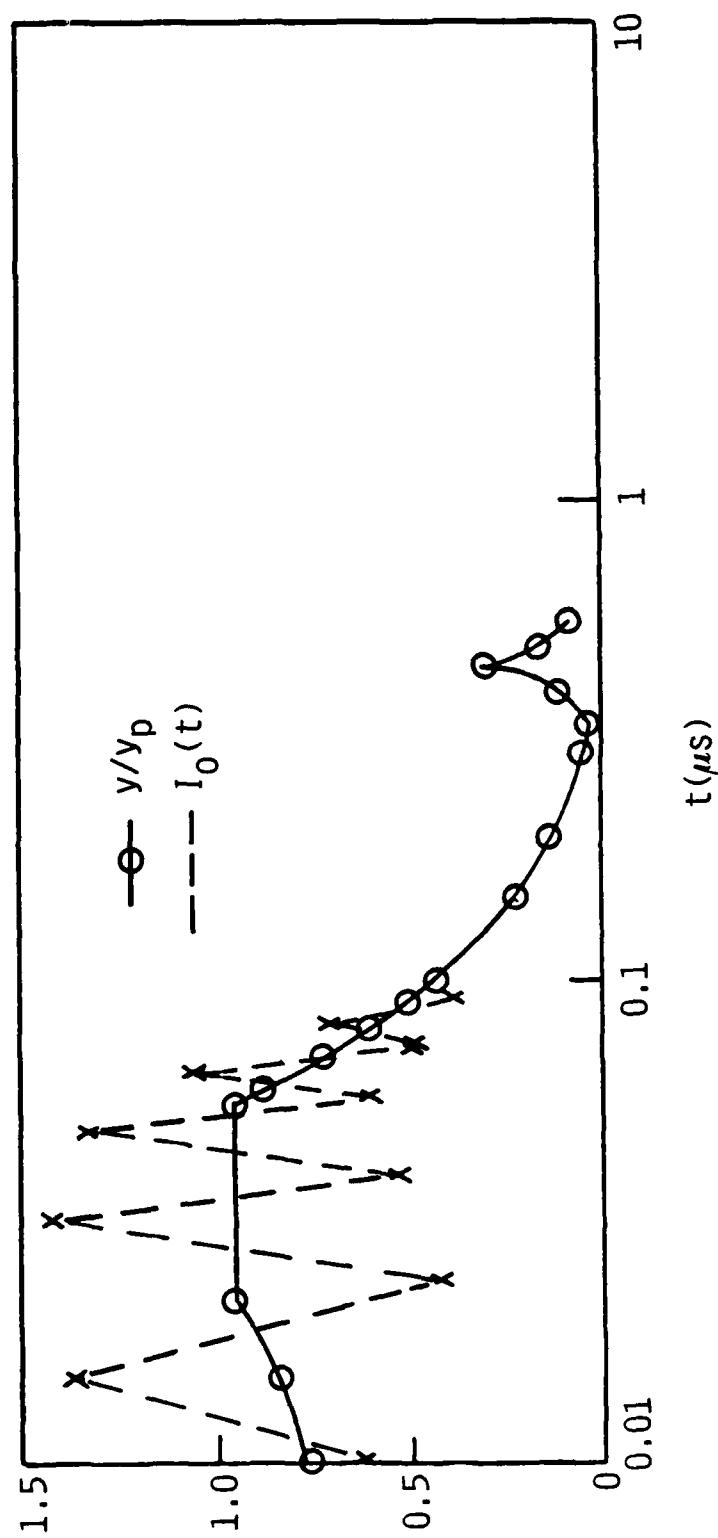


Fig. 2.1 Laser intensity used in wall pressure calculation.

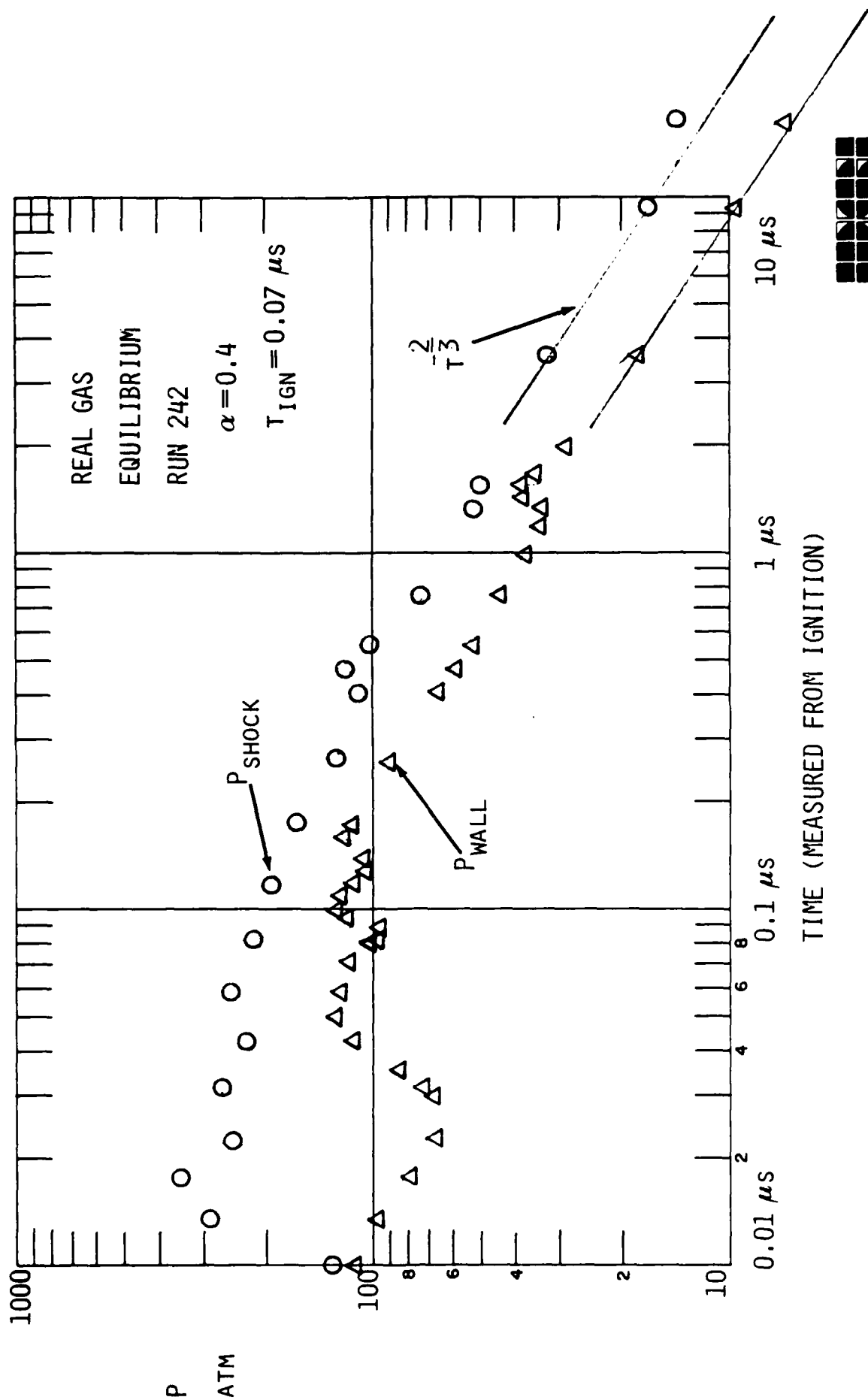


Fig. 2.2 Pressure vs time.

CHANGE IN LSD WAVE PRESSURE WITH VELOCITY

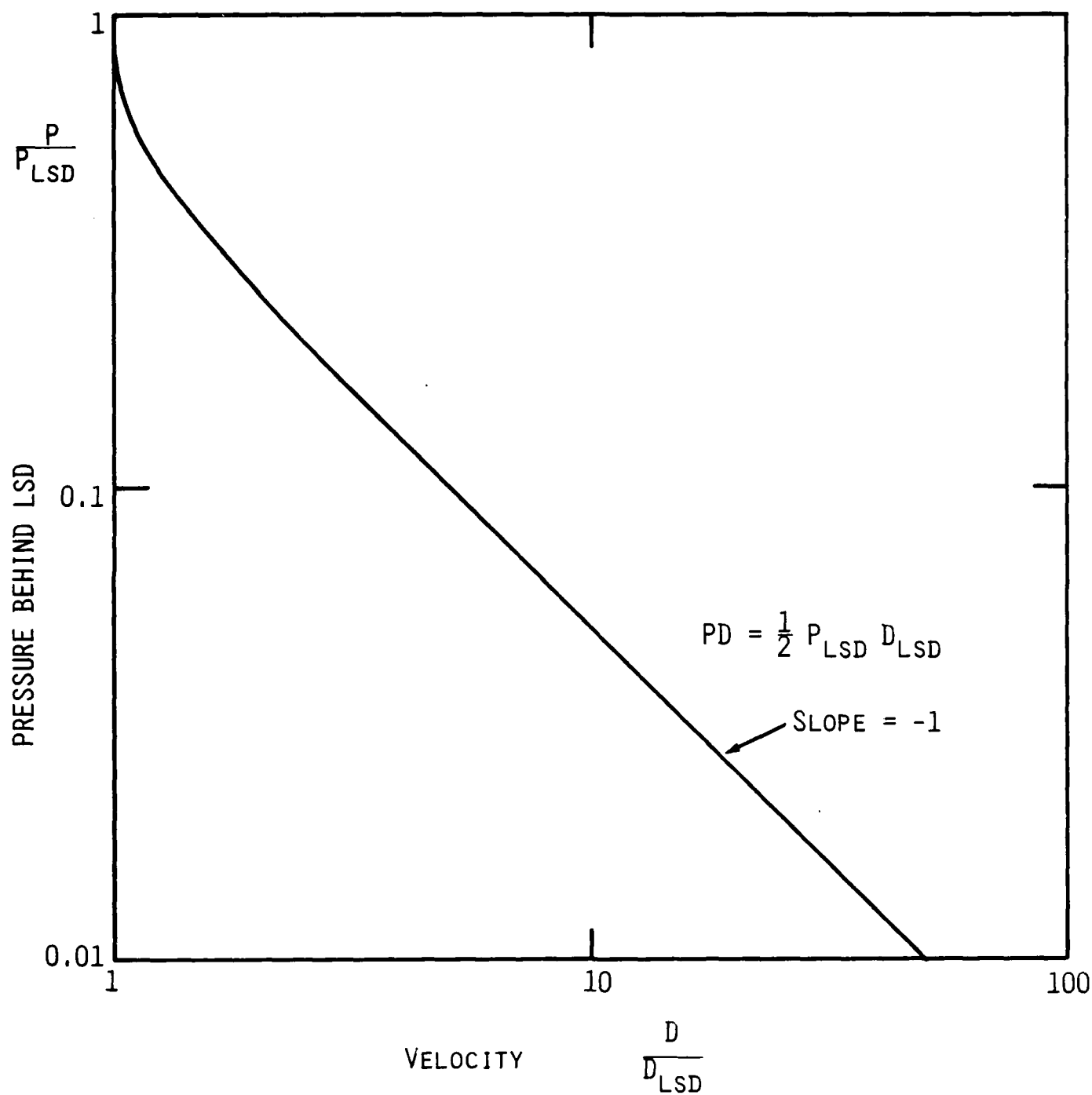


Fig. 2-3 Change in LSD wave pressure with velocity.

tween the wave and the wall for small increases in wave velocity. This is because the faster wave velocity produces a lower gas velocity behind the wave. The onset of radiation effects on wave velocity is best detected by measurements of the wave velocity.

However the presence of a lower gas velocity shortens the communication time between the shock wave and the wall. The pressure increase that occurs at the shock front due to an increase in laser intensity, for example that caused by the secondary pulse occurring at about $0.5 \mu\text{s}$ in Fig. 2.1, must propagate upstream against the gas flow to reach the wall. The shortening in time is evident in the measurements where the measured time of the pressure increase at the wall due to the secondary pulse at $1 \mu\text{s}$ (see Fig. 2.4) is considerably shorter than the calculated time $1.5 \mu\text{s}$ as shown in Fig. 2.2. This should be considered indicative of high intensity radiation wave phenomena, and is important for calculating the impulse per unit area.

A description of LSDNS and the modifications made to it to do these calculations is presented in the next section and the manner in which we handled the real gas is described in the following section.

2.1 Calculation of Wall Pressure

PSI has a computer code called LSDNS which calculates quasi-one-dimensional non-steady flow with laser heat addition. This code has been used to calculate the fluid mechanics phenomena occurring in pulsed laser propulsion thrusters, for example. It has the ability to capture a laser-supported detonation wave caused by the absorption of laser energy. The thermodynamic properties of the gas which is absorbing the laser energy are input as a table, so the code can handle gases in thermochemical equilibrium. The absorption coefficient of the gas at laser wavelengths is specified as a function of the thermodynamic state of the gas.

The development and application of this code to the fluid mechanics of pulsed laser propulsion is described in Refs. 2 and 3. In the present work, the code was used to calculate the pressure at $x = 0$, where a reflection boundary condition is imposed. This boundary condition represents the condition at a solid wall, so p at $x = 0$ is the wall pressure.

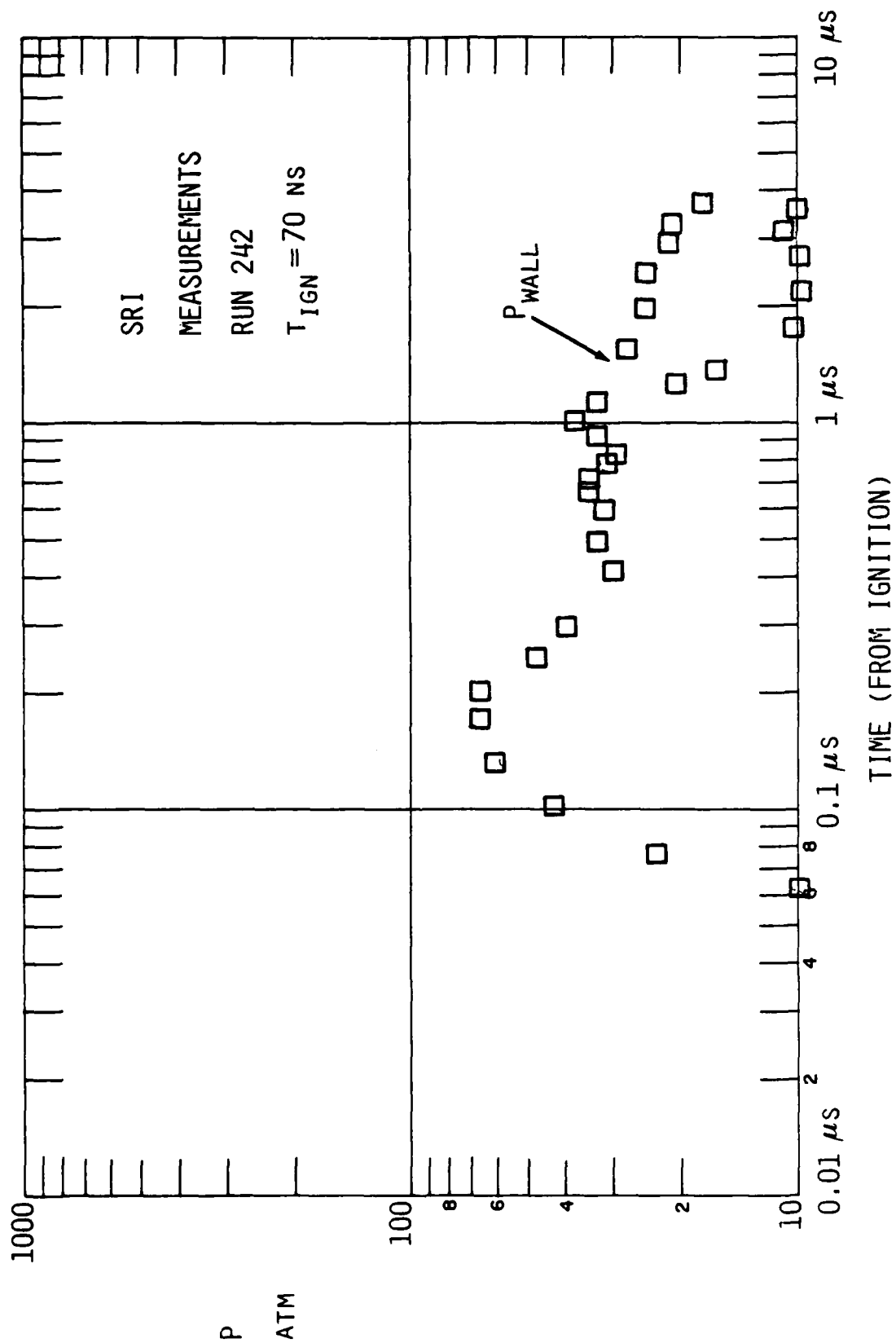


Fig. 2-4 Pressure vs time.

In the present case, the code was used in its purely one-dimensional form. The equations of conservation of mass, momentum and energy are:

$$\frac{\partial \rho}{\partial t} + \frac{\partial \rho u}{\partial x} = 0$$

$$\frac{\partial \rho u}{\partial t} + \frac{\partial}{\partial x} (\rho + \rho u^2) = 0$$

$$\frac{\partial}{\partial t} \left[\rho \left(e + \frac{u^2}{2} \right) \right] + \frac{\partial}{\partial x} \left[\rho u \left(e + \frac{p}{\rho} + \frac{u^2}{2} \right) \right] = \frac{\partial I}{\partial x}$$

Here ρ , p , u , e are density, pressure, velocity and internal energy per unit mass, respectively. I is the laser intensity, which obeys the radiation transport equation in the absence of emission.

$$dI/dx = k_L I ,$$

where k_L is the laser energy absorption coefficient. The solution of this transport equation is

$$I = I_0(t) \exp \left(- \int_x^{\infty} k_L dx \right) ,$$

where the incoming laser intensity I_0 is at $x = \infty$. Notice that the sign of the transport equation is chosen so that the laser intensity decreases with decreasing x , since the laser beam is propagating in the negative x direction, toward the wall.

To complete the formulation of the problem, we must specify the time dependence of I_0 , the dependence of k_L on the gas state, and the thermal and caloric equations of state, $p(\rho, e)$, $T(\rho, e)$. Then solution of the equations will provide the desired wall pressure $p(x = 0, t)$.

2.2 Laser Absorption Coefficient

The choice of the absorption coefficient was made with a view toward simplicity. The only real purpose of k_L is to get the energy into the gas, so an elaborate formulation was neither necessary or possible within the constraints of the present effort. A further reason for simplicity was suggested

by the size of the equation of state table that would be needed. For the solution of the flow equations only p and T as functions of ρ and e are needed. If k_L requires species concentrations, then they would also have to be in the table.

Based on these factors, k_L was chosen as

$$k_L = 10^{-3} \text{ for } T < 5000 \text{ K}$$

$$= 10^3 \left(\frac{p T_o}{p_o T} \right)^2 \text{ for } T > 5000 \text{ K ,}$$

where p_o and T_o are the conditions before the laser pulse. The quadratic dependence on p/T is suggested by the dependence of inverse bremsstrahlung absorption on the product of the electron and ion number densities.

2.3 Equation of State

Air is the gas of interest in the present work. The natural variables for the flow equations are seen to be ρ and e . From these two thermodynamic variables, all the others can be obtained under conditions of thermochemical equilibrium. Of course, e cannot be used as an independent variable directly. The equations for equilibrium air can be formulated using ρ and T as independent variables. Then an iteration scheme can be used to find T for a given ρ and e . With this T , p and any other desired variables can be found. The method of solution of the flow equations requires use of the local speed of sound to determine the time step, so the speed of sound is included in the equilibrium calculation.

During the solution of the flow equations, the expressions $T(\rho, e)$ and $p(\rho, e)$ must be evaluated many times. To avoid having to iterate on e each time, a table of T , p , and a (speed of sound) is constructed, using ρ and e as independent variables. This table is constructed by the iteration process, but the number of entries is several orders of magnitude less than the number of evaluations of T , p , and a needed in the course of solution. For these evaluations, quadratic interpolation in the table is used.

The formulation of a model of equilibrium air is described in the next section. The air is taken as a mixture of oxygen and nitrogen, with no trace elements included. Up to 20,000 K, species included are N, N⁺, NO, NO⁺, N₂, N₂⁺, O, O⁺, O⁻, O₂, O₂⁺, O₂⁻, and E. An equilibrium program is used which utilizes fits to the partition functions good up to 20,000 K, and takes ρ and T as independent variables. Above 20,000 K, a different equilibrium program is used, which deals only with atoms and ions, but no molecules. It handles a mixture of two ionizing monatomic gases, and in the present calculations used 6 ions of each atom, oxygen, and nitrogen. It includes lowering of the ionization potential. It uses as input the energy levels and weights of the internal state of each atom and ion, suitably grouped.

Using this model of air, the table of T, p, and a as a function of ρ and e was constructed for use in the solution of the flow equations.

2.4 Laser Intensity

Laser intensity was modeled by fitting the experimental intensity provided. A table was available providing y/y_p vs. time, from 21 to 729 ns. A log-log plot showed that the curve could be represented by five straight line segments. Least square fits to these five segments provided the following equations:

$$\begin{array}{lll} 64 < t < 94: & y/y_p = 2.214 \times 10^{-4} t^{1.8536} & (1) \\ 94 < t < 125: & y/y_p = 0.949 & (2) \\ 125 < t < 409: & y/y_p = 3.847 \times 10^5 t^{-2.67} & (3) \\ 409 < t < 521: & y/y_p = 4.6125 \times 10^{-28} t^{9.869} & (4) \\ 521 < t < 625: & y/y_p = 1.8075 \times 10^{20} t^{-7.65} & (5) \end{array}$$

Here t is in nanoseconds.

The fit was made between 64 and 625 ns because the values after 625 ns appeared to be zero, and we allowed the first 70 ns for the ignition process. The flow field code LSDNS was started at the 70 ns point, and the laser was turned off at 625 ns.

Equations (1-5) were used over intervals determined by the fits, with the joining points chosen where the fitting equations were equal. The range of t for each of the equations is the following:

$$\begin{aligned} 70. < t < 91.09. & (1) \\ 91.09 < t < 126. & (2) \\ 126. < t < 422. & (3) \\ 422. < t < 521. & (4) \\ 521. < t < 625. & (5) \end{aligned}$$

In addition to the mean values just modeled, an oscillation was imposed, of the form

$$F = 1 + Ae^{-Bt} \cos Dt.$$

Where t is specified in ns. The constant D was chosen so as to produce a complete oscillation in 17 ns, so that $D = 2\pi/17 = 0.3696$. The other two constants were chosen by specifying that the amplitude of the oscillation at the end of 4 cycles (68 ns) was 1.79, and at the end of 8 cycles (136 ns), it was 1.32. These result in the values $B = 0.01329$ and $A = 1.950$. Therefore, F was taken as

$$F = 1 + 1.950 e^{-0.01329t} \cos 0.3696t.$$

The final intensity was then

$$I_0(t) = KF(y/y_p)$$

starting at 70 ns, where K is a scaling constant.

A plot of y/y_p and $I_0(t)$ is shown in Fig. 2.1, with $K = 1$.

The total fluence incident up to any time is just the time integral of I_0 . Although the expression can be integrated analytically, it is simpler to just evaluate I_0 at small time intervals and perform the summation. The scaling constant K is used to specify the fluence desired by using the integral of I_0 between the desired times.

2.5 Model for High Temperature Air

This appendix describes the model used for high temperature air. The model involves two different temperature regimes, above and below 20,000 K.

Below 20,000 K PSI has a standard equilibrium program which uses curve fits to the partition functions to determine the equilibrium constants for a gas mixture. For use below 6000 K, the data in the JANAF tables are used. For certain species, curve fits applicable up to 20,000 K have been constructed. These fits were made in a form compatible with the analytical expressions for the partition functions. The natural logarithm of the partition function Q was expressed as

$$\begin{aligned}\ln Q = & L_1' + L_2' \ln T - L_3'/T + L_4'/T^2 + L_5' T \\ & + L_6' T^2 + L_7' T^3 + v(T)\end{aligned}$$

The constants were determined by a combination of analytical expressions and curve fitting. At moderate temperatures, Q is a combination of rotational, vibrational and electronic partition functions:

$$Q = Q_t Q_r Q_v Q_e.$$

The expressions for the component partition functions are:

$$Q_t = (2\pi mkT/h_p)^{3/2}$$

$$Q_r = T/\sigma\theta_r$$

$$Q_v = (1 - e^{-\theta_v/T})^{-1}$$

$$Q_e = ge^{-D/T}$$

Here m is the species mass, k is Boltzmann's constant, h_p is Planck's constant, θ_r is the rotational temperature for diatomics, σ is unity except for homonuclear molecules for which $\sigma = 2$, θ_v is the vibrational temperature for diatomics, g is the degeneracy of the ground electronic state, and D is the energy of the species at zero temperature, expressed in K.

The constants $L_1' - L_3'$ and $v(T)$ were used to agree with these simple expressions:

$$L_1' = 1.5 \ln(2\pi mk/h_p^2) + \ln(g/\sigma\theta_r)$$

$$L_2' = 2.5 \text{ for diatomic species}$$

$$= 1.5 \text{ for monatomic species}$$

$$L_3' = D$$

$$v(T) = -\ln(1 - e^{-\theta_v/T}) \text{ for diatomic species}$$

$$= 0 \quad \text{for monatomic species}$$

The remaining constants $L_4' - L_7'$ were used to fit the expression for $\ln Q$ to a calculation of Q which included many terms in the electronic partition function, anharmonicity in vibration, and vibration-rotation coupling, but not lowering of the ionization potential. This method of fitting provided good fits, and also small values of the constants $L_4' - L_7'$.

Air is taken to be a mixture of oxygen and nitrogen, in the molar composition of 78.849% N₂, 21.151% O₂, a ratio of 0.26825 O₂ to each N₂. The species which have been fitted include N, N⁺, NO, NO⁺, N₂, N₂⁺, O, O⁺, O⁻, O₂, O₂⁺, O₂⁻, E.

Above 20,000 K, there are no molecules present. We assume that only atomic species and their positive ions are present. Therefore, air is represented as a mixture of 2 monatomic ionizing gases. A computer program for the equilibrium state of such a mixture was developed, based on a previous program for a single monatomic ionizing gas.

We consider a mixture of two gases, denoted by superscripts 1 and 2. For each gas, there are atoms and $N-1$ ions, plus electrons, a total of $2N + 1$ species. The number densities are $n_A^1 = n_1^1$, $n_A^2 = n_1^2$, n_i^1 , n_i^2 ($i = 2, 3, \dots, N$) and n_E . The corresponding masses are $m_A^1 = m_1^1$, $m_A^2 = m_1^2$, $m_i = m_A - (i - 1)m_E$ for both species 1 and 2, and m_E . The charges are 0, $(i - 1)$ and -1 electronic charges.

The total number density is

$$n = n_A^1 + n_A^2 = n_E + \sum_{i=2}^N (n_i^1 + n_i^2) \quad (2.1)$$

charge conservation requires

$$-n_E + \sum_{i=1}^N (i - 1)(n_i^1 + n_i^2) = 0 \quad (2.2)$$

The density of the mixture is

$$\begin{aligned} \rho = & m_A^1 n_A^1 + m_A^2 n_A^2 + m_E n_E + \sum_{i=2}^N [n_i^1 (m_A^1 - (i - 1)m_E) \\ & + n_i^2 (m_A^2 - (i - 1)m_E)] \end{aligned}$$

The use of charge conservation simplifies this to

$$\rho = m_A^1 (n_A^1 + \sum_{i=2}^N n_i^1) + m_A^2 (n_A^2 + \sum_{i=2}^N n_i^2) \quad (2.3)$$

The mole ratio of the mixture is defined to be

$$f_n = (n_A^2 + \sum_{i=2}^N n_i^2) / (n_A^1 + \sum_{i=2}^N n_i^1) \quad (2.4)$$

which allows the total number density to be written as

$$n = (n_A^1 + \sum_{i=2}^N n_i^1)(1 + f_n) + n_E \quad (2.5)$$

If we also define the mass ratio as

$$f_m = m_A^2 / m_A^1 \quad (2.6)$$

the density Eq. (2.3) becomes

$$\rho = m_A^1 (n - n_E) (1 + f_n f_m) / (1 + f_n) \quad (2.7)$$

The gas law is

$$p = nkT = \frac{k}{m_A^1} \frac{\rho T}{1 - n_E/n} \frac{1 + f_n}{1 + f_n f_m} \quad (2.8)$$

The equilibrium state is specified by the Law of Mass Action relating the partial pressures of the i -th and $(i+1)$ -th ions to the electron partial pressure:

$$p_E p_i + 1/p_i = f_{ip}(T)$$

Here f_{ip} is the equilibrium constant for the ionization of the i -th ion, which will be defined later.

If we introduce the normalized reaction variables

$$\alpha_i = n_i/n = P_i/P \quad (2.9)$$

then Mass Action becomes

$$\alpha_E \alpha_{i+1} / \alpha_i = f_{ip} / P \quad (2.10)$$

which is the form appropriate to the use of P and T as independent variables. For the present application, we need ρ , T as independent variables, so we re-write Eq. (2.10) using the gas law Eq. (2.8):

$$\frac{\alpha_E}{1 - \alpha_E} \frac{\alpha_{i+1}}{\alpha_i} = \frac{f_{ip}}{\rho T} \frac{m_A^1}{k} \frac{1 + f_n f_m}{1 + f_n} \quad (2.11)$$

There are $N-1$ ions of each species, and an equation like this for the formation of each ion. Thus there are $2(N-1)$ such equations.

In terms of the α variables, the number density relation, Eq. (2.1), the charge conservation relation, Eq. (2.2), and the mole ratio relation, Eq. (2.4), may be written

$$1 = \alpha_A^1 + \alpha_A^2 + \alpha_E + \sum_{i=2}^N (\alpha_i^1 + \alpha_i^2) \quad (2.12)$$

$$-\alpha_E + \sum_{i=2}^N (i-1)(\alpha_i^1 + \alpha_i^2) = 0 \quad (2.13)$$

$$\alpha_A^2 + \sum_{i=2}^N \alpha_i^2 = (\alpha_A^1 + \sum_{i=2}^N \alpha_i^1) f_n \quad (2.14)$$

The lowering of the ionization potential is calculated using the Debye-Huckel theory. The decrement in the potential is given by

$$\Delta I_i = 2ie^3 \left(\frac{\pi}{kT} \right)^{1/2} \left(\sum_{j=2}^N (n_j^1 + n_j^2)(j-1)^2 + n_E \right)^{1/2} \quad (2.18)$$

where e is the electron charge in esu. If ΔI_i is expressed in ergs, $2e^3\sqrt{\pi/k} = 3.343 \times 10^{-20}$, while if it is expressed in cm^{-1} , one divides by hpc so the constant is $2e^3\sqrt{\pi/k}/hpc = 1.683 \times 10^{-4}$.

Since ΔI_i involves n_i^1 , n_i^2 and n_E , while I_{Li} is needed on the right side of Eq. (2.18) to calculate these quantities, the solution must clearly be iterative. However, solving for the α is already iterative. The procedure followed was simply to use the current values of the number densities to calculate the ΔI_i used to find the next iteration on α . In view of the approximate nature of the ΔI_i correction, this procedure is sufficiently accurate.

The internal energy per unit mass of each species is expressed in terms of the internal partition function by

$$e_i = \frac{kT}{m_i} \left[\frac{3}{2} + \frac{T d \ln Q_{i,int}}{dT} \right], \quad e_E = \frac{3}{2} = \frac{kT}{m_E} \quad (2.19)$$

where the first term is the translational part. The mixture internal energy is then

$$e = \sum_i e_i \rho_i / \rho + e_E \rho_E / \rho, \quad \rho_i = m_i n_i \quad (2.20)$$

Using Eq. (2.16) in Eq. (2.19) and performing the sum in Eq. (2.20), we find

$$e = \frac{3}{2} \frac{p}{\rho} + \sum_i \frac{n_i}{\rho} \left[\epsilon_i^* + \frac{\sum_j g_{ij} \epsilon_{ij} e^{-\epsilon_{ij}/kT}}{\sum_j g_{ij} e^{-\epsilon_{ij}/kT}} \right] \quad (2.21)$$

The sum over i is carried out over all the atoms and ions, $2N$ terms, but not over the electrons which have no internal energy.

The enthalpy per unit mass is found from e as

$$h = e + p/\rho \quad (2.22)$$

The formulation so far has treated multiple-ionizing atoms. If we are interested in using this model to represent the high temperature state of a mixture of diatomic molecules, where there are no molecules present, the question of the energy reference level arises. So far, the energy reference level has been that of the atoms at zero degrees K. However, in most application to diatomic molecules the reference level used is the molecules at zero degrees K. This requires the addition of energy to the expressions for e and h , to refer them to the correct level. This is simply done by adding to each atom and ion one half the dissociation energy per molecule. If these dissociation energies are denoted by D^1 , D^2 , then the internal energy and enthalpy referred to the molecule is related to the values in Eqs. (2.21) and (2.22) by

$$e^* = e + \sum_{i=1}^N (n_i^1 D^1 + n_i^2 D^2) / 2\rho \quad (2.23)$$

$$h^* = h + \sum_{i=1}^N (n_i^1 D^1 + n_i^2 D^2) / 2\rho \quad (2.24)$$

The speed of sound can be found from the specific heats and derivatives of p with respect to the independent variables ρ and T . The specific heat at constant volume is

$$c_v = (\partial e / \partial T)_\rho \quad (2.25)$$

while the specific heat at constant pressure is related to c_v by

$$c_p = c_v + \frac{T}{\rho^2} \left(\frac{\partial p}{\partial T} \right)_\rho^2 / \left(\frac{\partial p}{\partial \rho} \right)_T \quad (2.26)$$

The speed of sound squared is

$$a^2 = \frac{c_p}{c_v} \left(\frac{\partial p}{\partial \rho} \right)_T \quad (2.27)$$

These relations express c_p , c_v and a^2 entirely in terms of derivatives which use ρ and T as independent variables. These derivatives can be found by finite difference expressions once e (or e^*) and p are known from Eqs. (2.21) (or 2.23) and (2.3). The same finite difference representations of the derivatives can be used with the low temperature model to find the specific heats and sound speeds.

With these models, the equilibrium state of air (the mixture of oxygen and nitrogen) can be obtained as a function of ρ, T . In particular, p , e and a can be found, as well as the number densities of the atoms and all ions one chooses to include.

To obtain the state as a function of ρ and e (or e^*), one can perform an iteration on T until the desired value of e or e^* is found. This was the procedure used to construct a table of p , T and a using ρ and e^* as independent variables. This table was used to supply the equation of state for the LSDNS Code.

PRESSURE AT THE WALL
REFERENCES

1. H.E. Lindberg, "Critical Loads to Destroy Reentry Vehicles with X-Rays, Blast, or Directed Beams," J. Defense Research, 9,1, April 1977, p. 1.
2. D. I. Rosen, et al., "Final Technical Report Pulsed Laser Propulsion Studies, Vol. I: Thruster Physics and Performance," TR-184, Physical Sciences Inc., Andover, MA, October 1982.
3. D. I. Rosen, et al., "Final Technical Report Studies of a Repetitively-Pulsed Laser Powered Thruster," TR-358, Physical Sciences Inc., Andover, MA, January 1983.

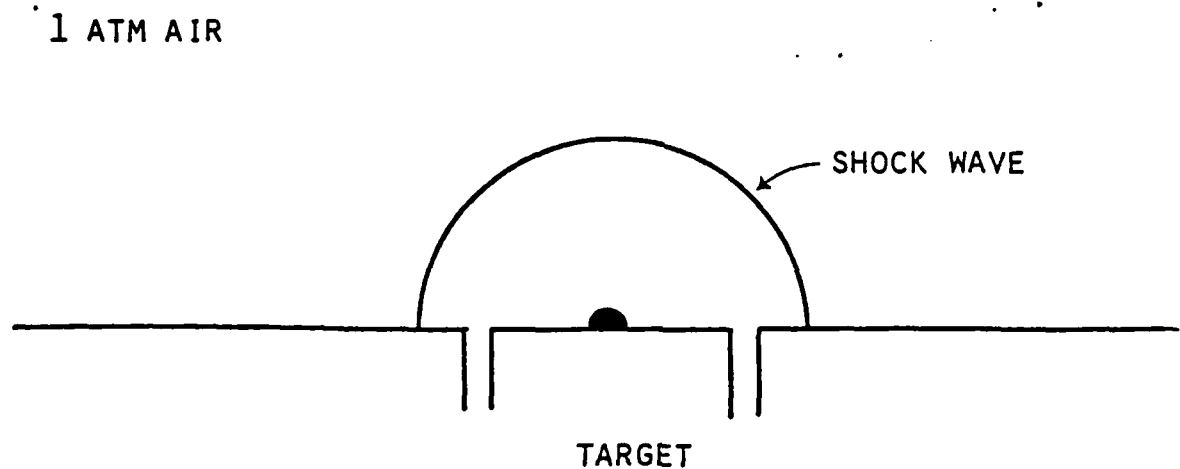
3. IMPULSE SCALING

Although the pressure time history on the target during and immediately after the laser pulse is very much dependent on the details of the laser interaction, LSD or radiation wave for example, the pressure at late times depends mainly on the total energy absorbed. Thus the impulse, the integral over time of the force, becomes independent of the laser interaction details in many cases, and valuable insight into the scaling with density and energy of the impulse can be obtained from quite simple ideas.

It will be found that these simple ideas lead to the scaling laws for the impulse as measured by the pendulum. It is important to note here that Lindbergs¹ work on the damage thresholds for re-entry vehicles found that the impulse was not the only determinant of failure but that the impulse per unit area was also important. He found that if the level of impulse required for a given spot area was determined and then the spot area was reduced by say a factor of ten the impulse required did not stay the same. It did not go down by ten as might be expected if it was mainly the impulse per unit area, the integral of pressure over time, that was important; rather, it went down a factor of three. They are both equally important. The insight these damage experiments give us about what to expect for impulse per unit area measurements will be discussed later when we discuss scaling.

Consider the geometry shown in Fig. 3.1 consisting of a target disk on which the impulse is to be determined, imbedded in an infinite plane. Assume that the laser spot size is small compared to the disk radius, and also that the distance the LSD or radiation wave travels in the laser pulse time, ct_p , is also small compared to the disk radius. We approximate the laser interaction by a spherical point detonation in the center of the disk in the half plane.

If the energy ahead of the shock wave can be neglected, Sedov² has shown that the solutions for the flow are self similar, meaning that the profiles of p , ρ and T behind the wave change in scale as the wave moves but not in shape; that is the pressure p is such that $P/p_s = f(r/r_s)$ where p_s the pressure at the shock point and the r_s position of the shock point vary with



CONTRIBUTION TO IMPULSE COMES FROM TIME WHEN SHOCK WAVE IS
ON TARGET PLUS TIME WHEN IT IS OFF TARGET

Fig. 3.1 Laser intensity used in wall pressure calculation.

time but the function f does not change. As the shock wave continues to expand the energy per unit mass in the gas behind the wave decreases and a point is reached where the energy per unit mass of the gas ahead of the shock is no longer negligible and the spatial profiles will depend upon the energy of the gas ahead of the shock wave. The distance at which this occurs can be estimated by setting the energy in the original point explosion equal to the energy in the background gas the shockwave has engulfed.

$$\frac{4\pi r_s^3}{3} P_1 = E_0$$

and thus we define a distance r_0 by

$$r_0 = \frac{E_0}{P_1}^{1/3} \quad \text{and} \quad \ell = \frac{r_s}{r_0}$$

such that the effects of the energy ahead are important when ℓ is of order 1. The change in the self-similar pressure profile for ℓ near one has been given by Sedov² and is reproduced in Fig. 3.2. An actual pressure curve using the curves and table of Fig. 3.2 is shown in Fig. 3.3 for the value of $\ell = .7566$. Notice that the pressure at the origin is negative, that is below atmospheric. At this time the impulse on the target is decreasing with time. This will be shown to be an important effect for large targets, that is, targets whose size is comparable to r_0 the energy radius. This effect is probably not important for cases of interest for damage because the pressures are quite low, approximately the ambient pressure. They are important for interpreting experimental data; for example all of the 10.6 μ single pulse data was in this regime.

For large energies simple blast wave scaling is appropriate. This scaling conserves total energy. Combining this with conservation of momentum across the shock wave the impulse scaling laws can be obtained.

Conservation of energy $\rho r^3 \approx E$

Conservation of momentum $\rho c^2 \approx P$

ONE-DIMENSIONAL UNSTEADY MOTION OF A GAS

$l = \frac{r_2}{r_1}$	$\tau = \frac{t}{r_1^2}$	$\frac{p_2}{p_1}$	Notation for l
Self-similar curves		∞	l_0
0.1867	0.01403	21.1	l_1
0.2669	0.03230	10.81	l_2
0.3342	0.05431	4.967	l_3
0.4890	0.1231	3.056	l_4
0.6003	0.1842	2.321	l_5
0.6812	0.2333	2.010	l_6
0.7566	0.2807	1.835	l_7
0.9566	0.3667	1.615	l_8
0.9801	0.4323	1.521	l_9
1.2524	0.6296	1.338	l_{10}
1.3210	0.6811	1.315	l_{11}
1.5171	0.8299	1.255	l_{12}
1.8751	1.1080	1.185	l_{13}
1.3222	1.4636	1.136	l_{14}
2.8641	1.8973	1.102	l_{15}
3.6963	2.7763	1.066	l_{16}
7.0791	5.3764	1.032	l_{17}
9.6424	7.5180	1.022	l_{18}

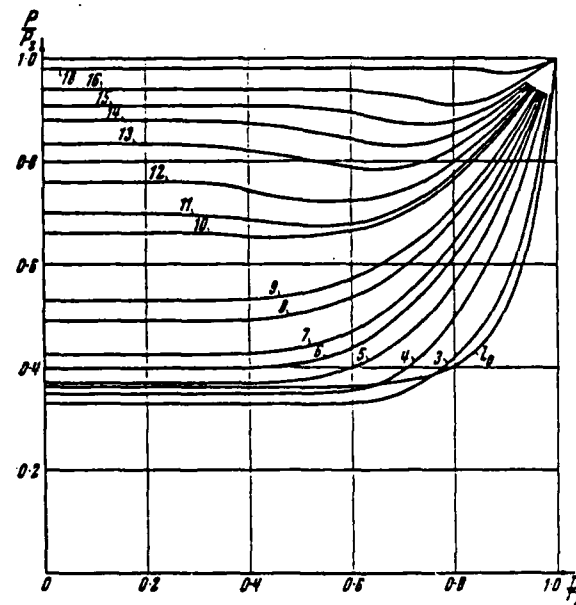


FIG. 84. Pressure distribution in a point explosion.

Fig. 3.2 One-dimensional unsteady motion of a gas.

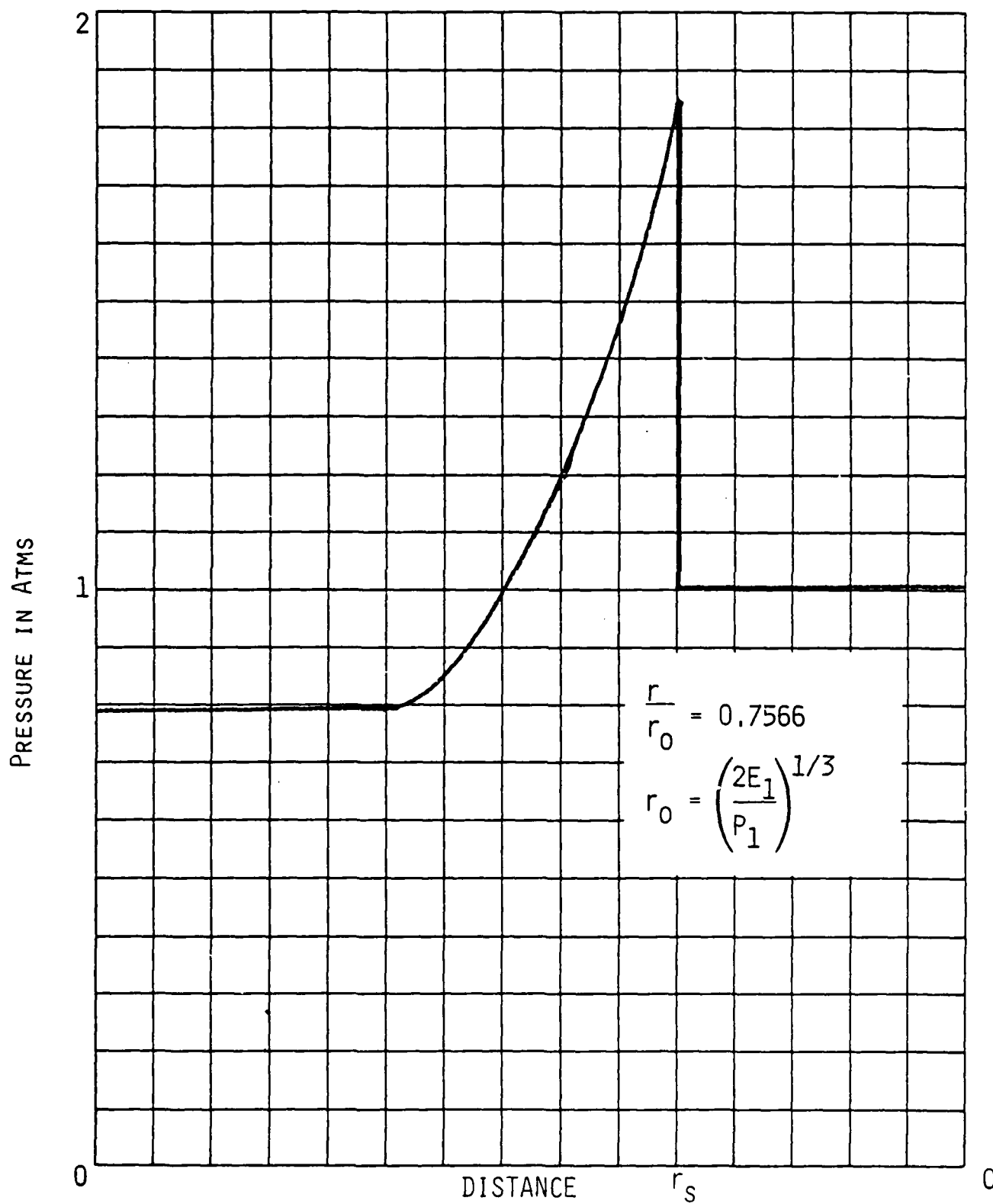


Fig. 3.3 Pressure behind spherical blast wave.

where p is the pressure behind the wave
 r is the position of the wave
 E is the energy put in by the laser
 ρ is the gas density ahead of the wave
 c is the velocity of the wave

To obtain the impulse on the target we wish to evaluate

$$I = \int_0^{\infty} p A dt$$

In this integral, A is the target area, and the integral is best evaluated by considering two times, early times when the shock wave is still on the target and late times when it is off the target. To do this it is easiest if the substitution

$$dt = \frac{dr}{c} \quad \text{is made.}$$

$$I = \int_0^{r_T} p A \frac{dr}{c} + \int_{r_T}^{\infty} p A \frac{dr}{c}$$

where r_T is the target radius

$$I \approx \int_0^{r_T} \left(\frac{E}{r^3} \right) r^2 \frac{dr}{\left(\frac{E}{\rho r^3} \right)^{1/2}} + \int_{r_T}^{\infty} \left(\frac{E}{r^3} \right) r_T^2 \frac{dr}{\left(\frac{E}{\rho r^3} \right)^{1/2}}$$

Notice both integrals are such that their major contribution derives from the time the blast wave radius is equal to the target radius. One can then write,

$$I \approx .93 r_T^{3/2} E^{1/2} \rho^{1/2}$$

where the constant has been derived from more detailed calculations^{3,4}. Thus we have, that as long as we stay with large laser energies, the impulse coupling coefficient I/E is expected to decrease as the inverse square root of the energy and as the square root of the density.

If an attempt is made to evaluate the impulse per unit area in a similar manner the integral diverges, the high blast wave pressure at early time dominates. In contrast to the case for the impulse where the early time details were unimportant, the early time details determine the impulse per unit area. Remember damage depends on both of these quantities. PSI has examined the blast wave scaling in more detail so as to avoid this difficulty and at the same time remove the earlier detailed restrictions, $r_s < r_T$ and $ct_p < r_T$. This work is described in the next section. This enables us to determine the impulse under more general conditions and also to determine the impulse per unit area and how it scales. However the PSI theory restricts itself to the strong shock limit; negative pressures are not considered as they are not interesting for damage as mentioned earlier. Koslova, et al.³ have carried the simple spherical blast wave analysis into this region and these results can be used to interpret the 10.6 μ m data which was taken in this regime. They found that using an ideal gas and a point explosion recreates the general effects but were higher than the data by a factor of two. They were required to use a distributed explosion and real gas effects to reproduce the data.

An interesting question is how much less than r_T , r_s has to be in order to ignore it and approximate the solution by a spherical blast wave solution. For the impulse per unit area the answer is never, as was stated before. For the impulse the data and PSI theory indicate that even for laser spot sizes equal to the target radius the simple spherical blast wave solution is good enough. For ct we have no data as ct was always much less than the target radius.

Figure 3.4 shows the 1.06 μ m data taken at Battelle on aluminum and compares it to the PSI theory appropriate for high laser energies, to the theory of Kozlova and also to the Russian data which has been summarized by the dashed curve. Note that the effect of the late time negative processes is noticeable at values of r_T/r_0 as low as .2. Figure 3.5 shows the data for Grafoil. Figure 3.6 compares the 10.6 μ m impulse data with the Russian 1.06 μ m data. The laser energy has been multiplied by 0.56 for the 10.6 μ m data to account for our best estimate as to the absorbed portion. Notice that this data is predominately in the large target regime.

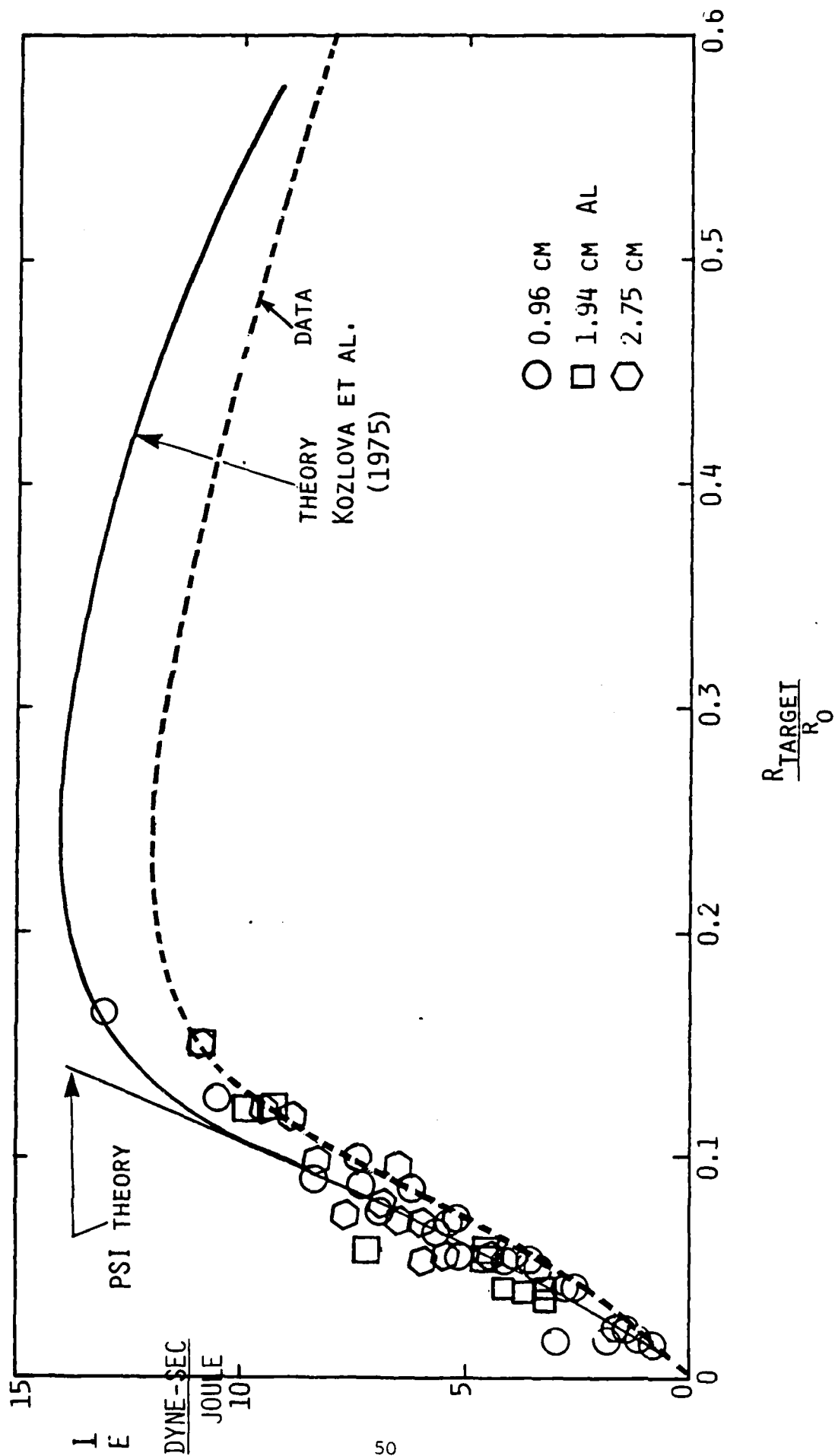


Fig. 3.4 Impulse Coupling 1.06 μ .

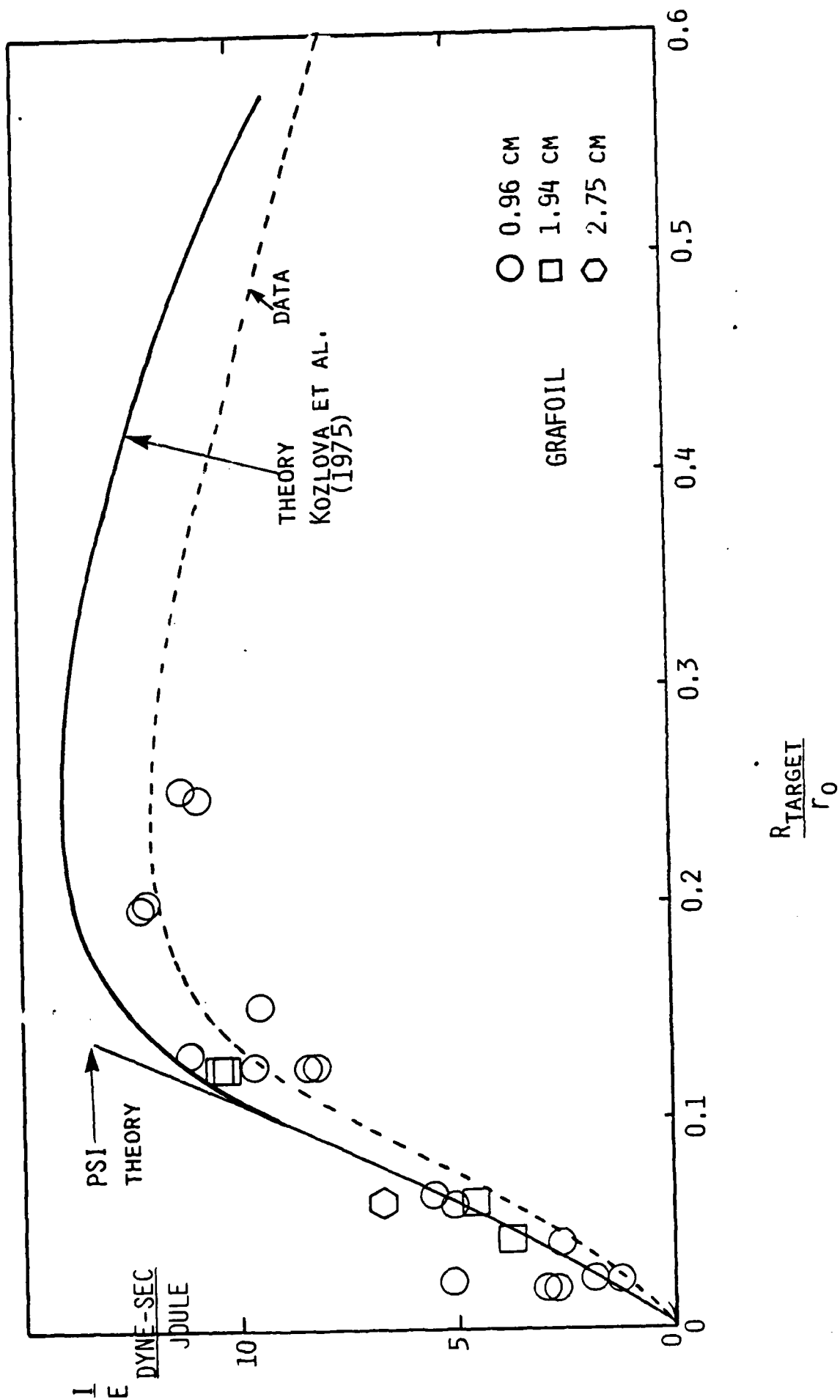
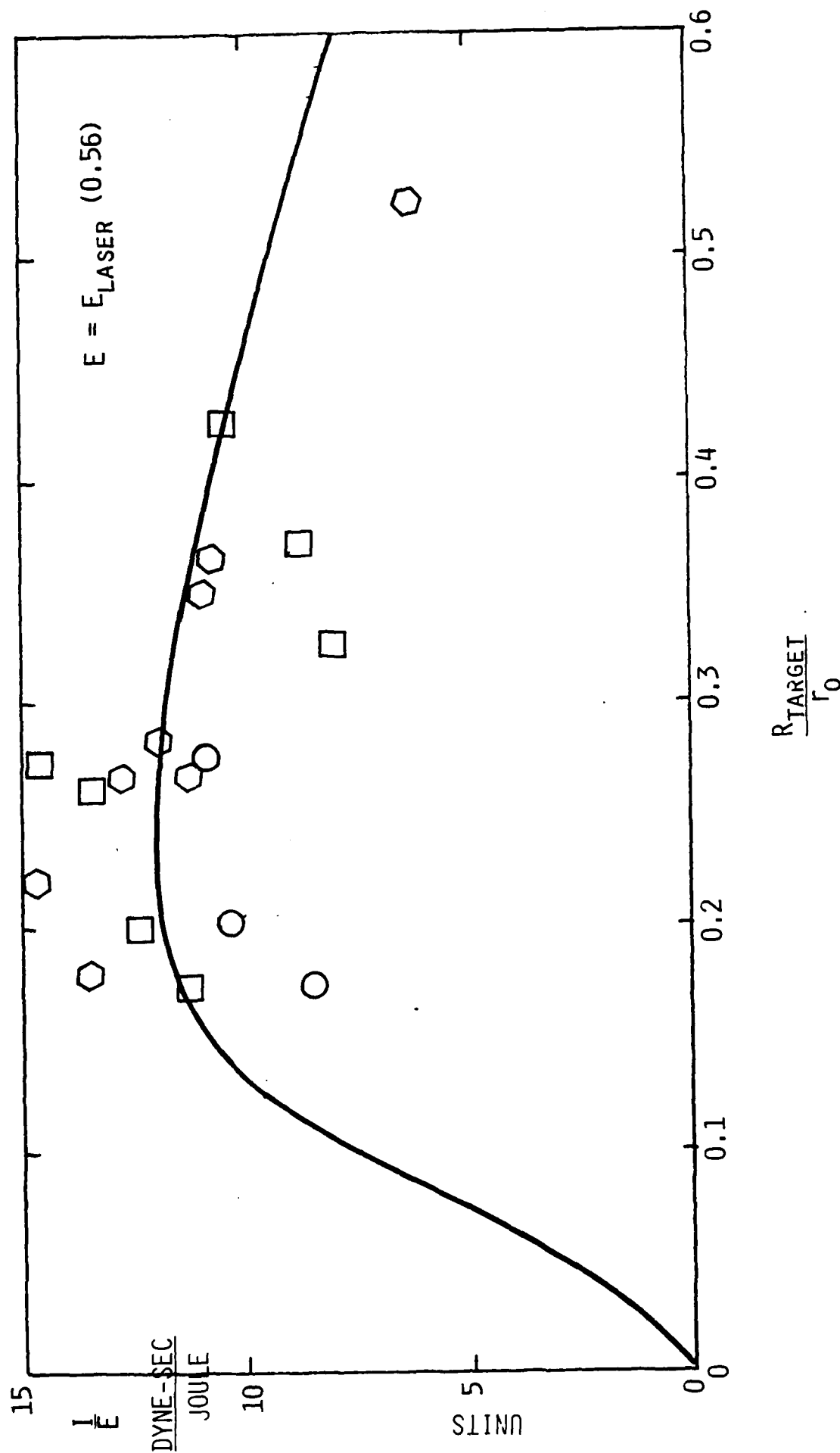


Fig. 3.5 Impulse Coupling 1.06 μ .

Fig. 3.6 Impulse Coupling 10.6 μ .

IMPULSE SCALING
REFERENCES

1. H.E. Lindberg, "Critical Loads to Destroy Reentry Vehicles with X-Rays, Blast, or Directed Beams," J. Defense Research. 9, 1, April 1977, p. 1 (SECRET).
2. L.I. Sedov, "Similarity and Dimensional Methods in Mechanics," Academic Press, New York and London, 1959.
3. N.N. Kozlova, et al., "Measurement of Recoil Momentum for a Laser Beam Interacting with an Absorbing Solid Surface in Air," Fizika Goreniya i Vzryva, 11, No. 4, pp. 650-654, July-August 1975.
4. G.A. Simons, "Asymptotic Theory for the Momentum Transfer to a Surface when Irradiated by a High Power Laser," Physical Sciences Inc., Andover, Ma., PSI SR-157, Appendix A.

4. SUPERSONIC RADIATION WAVES

When a piston travels down a cylinder filled with a gas, it pushes the gas ahead of it compressing and heating it. The compression and heating is accomplished by gas collisions in a narrow region known as a shock wave. If the piston travels at a constant velocity, the shock wave moves ahead of it at a constant, higher velocity creating a region of compressed heated flow. The properties of the gas in this region can be determined by conserving mass, momentum and energy across the wave. For strong shocks where the gas energy ahead of the wave can be neglected the conservation equations are:

$$u = \left(1 - \frac{\rho_0}{\rho}\right) \quad \text{Mass} \quad (4.1)$$

$$p = \rho_0 D u \quad \text{Momentum} \quad (4.2)$$

$$\rho_0 D \left(e - \frac{u^2}{2}\right) = J_0 \quad \text{Energy} \quad (4.3)$$

$$e = e(p, \rho) \equiv \frac{1}{\gamma - 1} \frac{p}{\rho} \quad \text{Gas Law} \quad (4.4)$$

Where

ρ_0 = Gas density ahead of the shock wave.

D = Shock wave velocity.

u = Gas velocity behind the wave in laboratory coordinates.

p, ρ, e = Pressure, density and internal energy behind the wave.

γ = The ratio of specific heats and is defined by the second equality.

J_0 = Represents an energy input per unit time and area from an external source, i.e., a laser.

For the case of the piston, the gas velocity u is equal to the piston velocity, $J_0 = 0$ and the source of energy compressing and heating the gas is the work being done by the piston $W = pu$. If the piston's velocity changes to a new constant velocity, this fact is communicated to the shock front at the speed of sound and eventually the shock strength adjusts to the new piston velocity. There is no difficulty doing this as $u + a > D$, that is sound waves leaving the piston at velocity a can overtake the shock wave.

If another source of energy (chemical or from a laser) exists, ($J_0 \neq 0$) this simple connection between the piston velocity and the shock velocity is lost. There is an unsteady flow field between the shock and the piston and the velocity at the piston is not usually the same as the velocity u , just behind the shock wave. With u no longer known the four equations now have five unknowns and another relation is required. The possible solutions to the conservation equations are shown with p and ρ_0/ρ as coordinates in Fig. 4.1 for air with an absorbed laser intensity J of 2×10^9 W/cm². For comparison the same curve for $J = 0$ is shown in the lower left hand corner. (Notice that the vertical scale has been divided by 100).

Combining Eq. 4.1 and 4.2 the relation $p = \rho_0 D^2 \left(1 - \frac{\rho_0}{\rho}\right)$ is obtained. Thus the slope of a line starting at $(0, 1)$ in the $p, \rho_0/\rho$ plane measures the quantity $\rho_0 D^2$. The minimum value of D is given by the line shown tangent to the curve at A. Jouquet (1905) pointed out this minimum velocity satisfies the condition that

$$u + a = D. \quad (4.5)$$

Strong detonations, corresponding to intersection points to the left of A, have $u + a > D$, thus information generated at the piston can reach the shock front; these provide solutions to the flow for large piston velocities $u_p > u_A$ where u_A is the gas velocity at the point A. Weak detonations, corresponding to intersection points to the right of A, have $u + a < D$ and imply an indeterminacy in specifying the flow for piston velocities $u_p < u_A$. (Usually the gas piston velocity is zero for the cases of interest for laser target interactions.) Chapman and Jouquet hypothesized that the wave would not run in this indeterminate region but at the point A and these waves satisfying Eq. 4.5 are called Chapman-Jouquet detonation waves. Using arguments based upon a combustion process propagation mechanism, von Neuman (1942) demonstrated that the weak detonation waves were in fact impossible. If the waves are to run in this region a propagation mechanism other than collisions (the combustion process) is required.

The addition of Eq. (4.5) to the original set of four now completes the set and the equations can be solved. The gas velocity just behind the wave can be determined and the unsteady flow field between the wave and the piston can be calculated.

When collisions are the mechanism of propagation for the wave, use of Eq. 4.5 closes the set of equations. However, if another propagation mechanism exists the Hugoniot curve shown in Fig. 4.1 admits higher velocity solutions such as the one shown for point B. Notice that the faster solutions have $\frac{p_0}{\rho} \rightarrow 1$ and from Eq. (4.1) this implies that the gas velocity is close to zero. This is a wave that goes very quickly through the gas, raising its pressure, density and velocity only slightly. Radiation can provide a mechanism for propagation of such a wave.

The wave absorbs the laser radiation, which is coming from in front of the wave, producing a hot gas of temperature T_f with internal energy E_f . This hot gas radiates energy forward (and backward), heating the gas in front of the wave. The heated gas becomes ionized and can in turn absorb the laser radiation through inverse bremsstrahlung, thus providing a mechanism for propagating the wave forward. Although in front of the wave, the unheated gas cannot absorb the laser radiation, but does absorb the radiation from the hot gas behind the wave which radiates predominantly in the deep ultraviolet. The physics just outlined can be expressed by

$$\rho_0 D e^* = \epsilon \sigma T_f^4 \quad (4.5A)$$

where

e^* is the energy required by the air in front of the wave before it can absorb the laser radiation

ϵ is the emissivity of the laser heater gas

σ is the Stefan-Boltzmann constant

Bergel'son et. al.¹ points out that as all the laser energy is assumed to be absorbed at the wave, there will be an overshoot in energy at the wave front equal to e^* , the energy radiated ahead, so that the energy right at the wave front e_f is given by

$$e_f = e + e^*$$

where as before E is the internal energy behind the wave. Such a situation is shown in Fig. 4.2. Notice that we have used the fact that the gas velocity goes to zero to neglect its square in the energy equations below. The energy Eq.(4.3) can now be rewritten

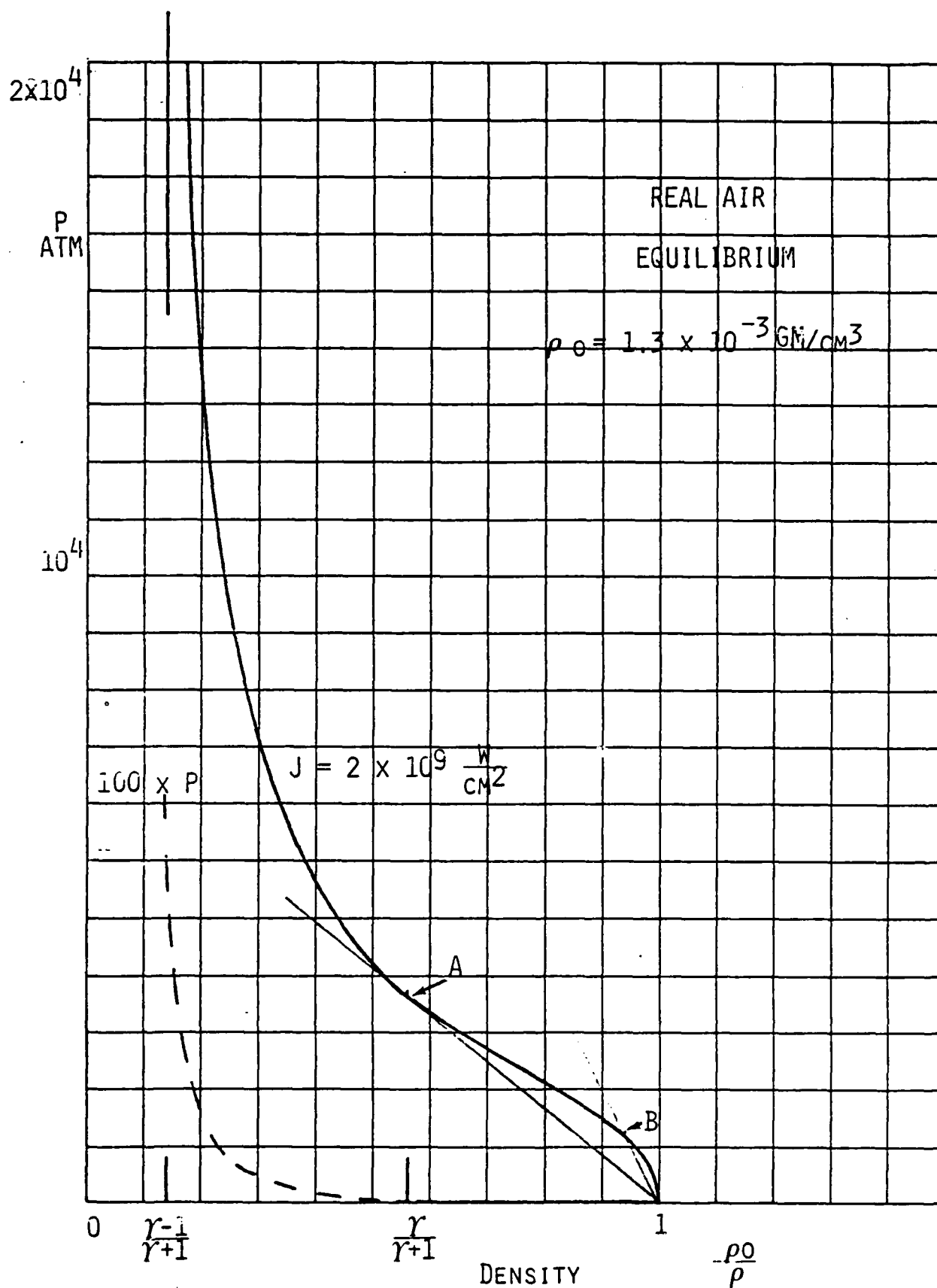
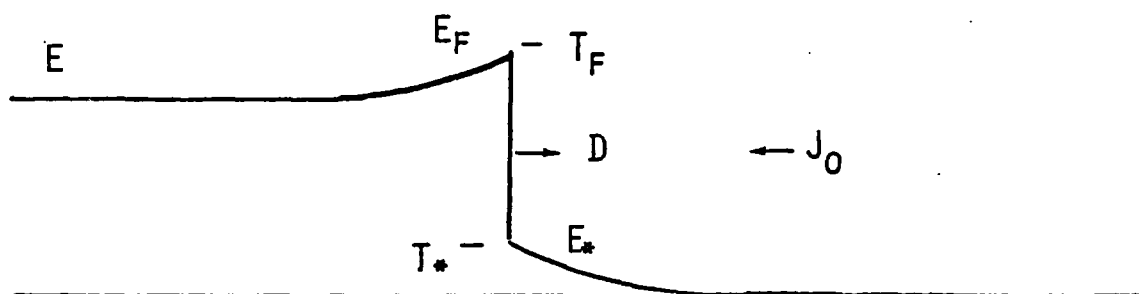


Fig. 4.1 Shock Hugoniot.

RADIATION WAVES



RADIATION FORWARD DRIVES WAVE

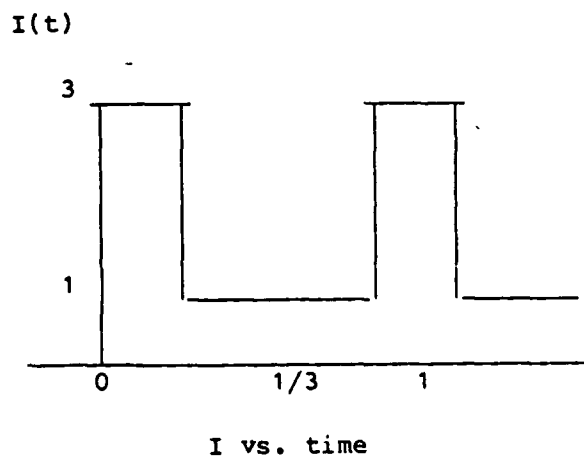


Fig. 4.2 Radiation forward drives wave.

$$\rho_0 D (e_f - e^*) = J_0 \quad (4.3A)$$

The set of Eqs. (4.1, 4.2, 4.3A & 4.4), plus Eq. (4.5A) makes a complete set and can again be solved for the five unknowns (e_f , p , ρ , u and D). The new propagation mechanism equation 5A has replaced equation (5). Notice that for these waves $u + a < D$, collisions no longer can play a role in the propagation mechanism.

The solution of this last set of equations has been considerably simplified by neglecting the square of the gas velocity in the energy equation in as much as only the two equations, 3A & 5A remain to be solved simultaneously. The determination of the energy e^* depends upon the absorption properties of the heated air, and thus depends upon a length scale l and the gas density.

For 1.06μ radiation the absorption is due to inverse bremsstrahlung. An absorption length of 1mm, a reasonable scale for waves traveling a centimeter or more requires a gas temperature of 2eV at one atmosphere density. Using e^* as 2eV and $\epsilon = 1$ the velocity and temperature as a function of laser intensity has been determined from equations 3A, 5A and the gas equation of state. In practice, since it is $e(T, \rho)$ that is calculated for real gases and ρ is fixed in this approximation, a value of T_f is chosen, D is determined from equation 5A and the required laser intensity from 3A. The results of such a calculation for real air at one atmosphere for 1.06μ radiation are shown in Figs. 4.3 and 4.4, where they are compared to results for an LSD wave. These results are compared with velocity data from the Batelle test series² in Fig. 4.5.

Calculations for a 10.6μ wavelength are similar. However, as the electron density required for absorption is proportional to $1/\lambda^2$ a significantly lower gas temperature is required at 10.6μ . Previous work on ignition³ indicated that when the gas temperature reaches 0.5 eV the absorption rises rapidly, and this temperature has been chosen for T^* for the 10.6μ calculations.

There is one further complication that must be addressed before comparing with the 10.6μ results at NRL. The NRL laser pulse was partially mode

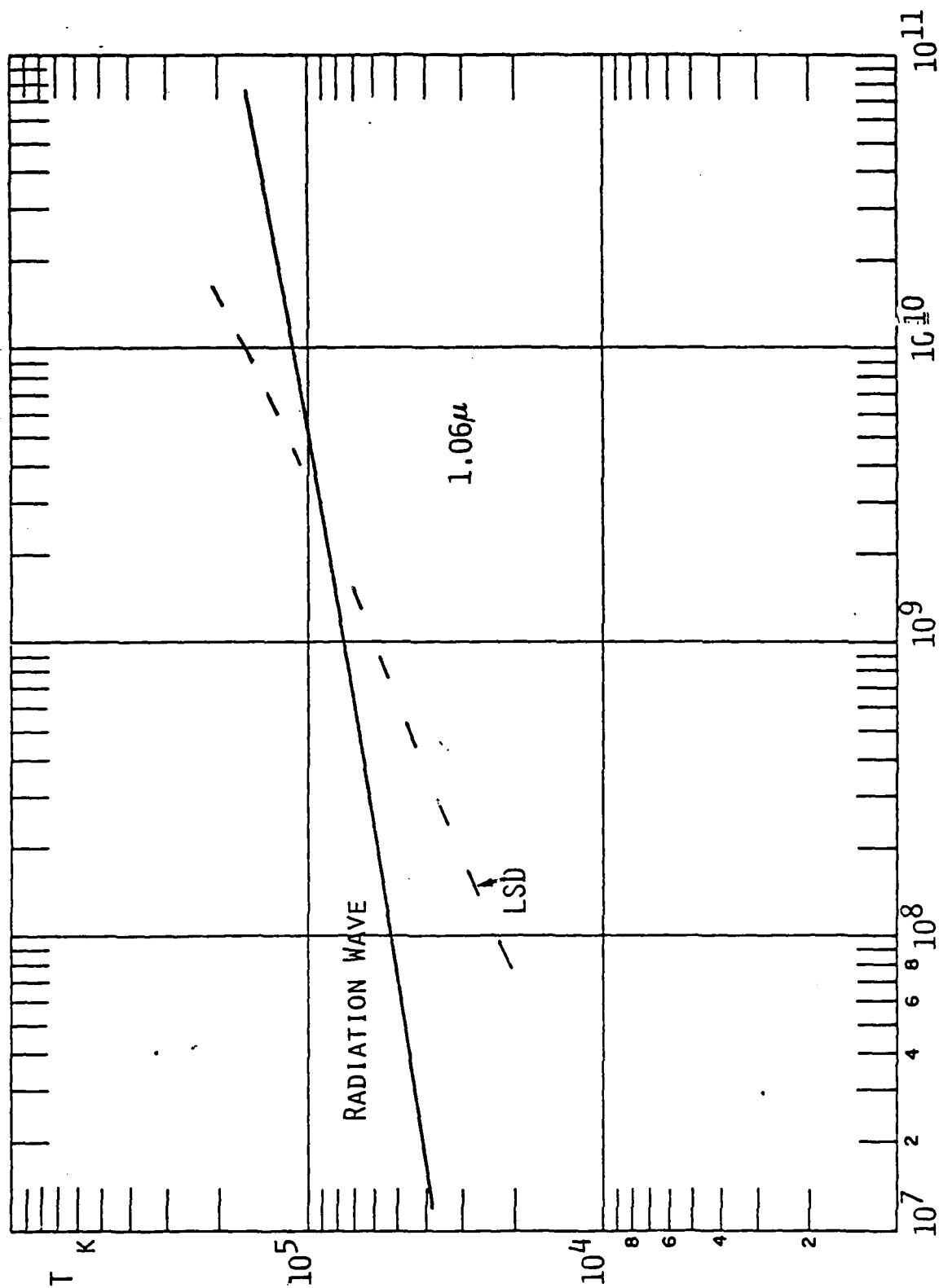


Fig. 4.3 Supersonic radiation wave.

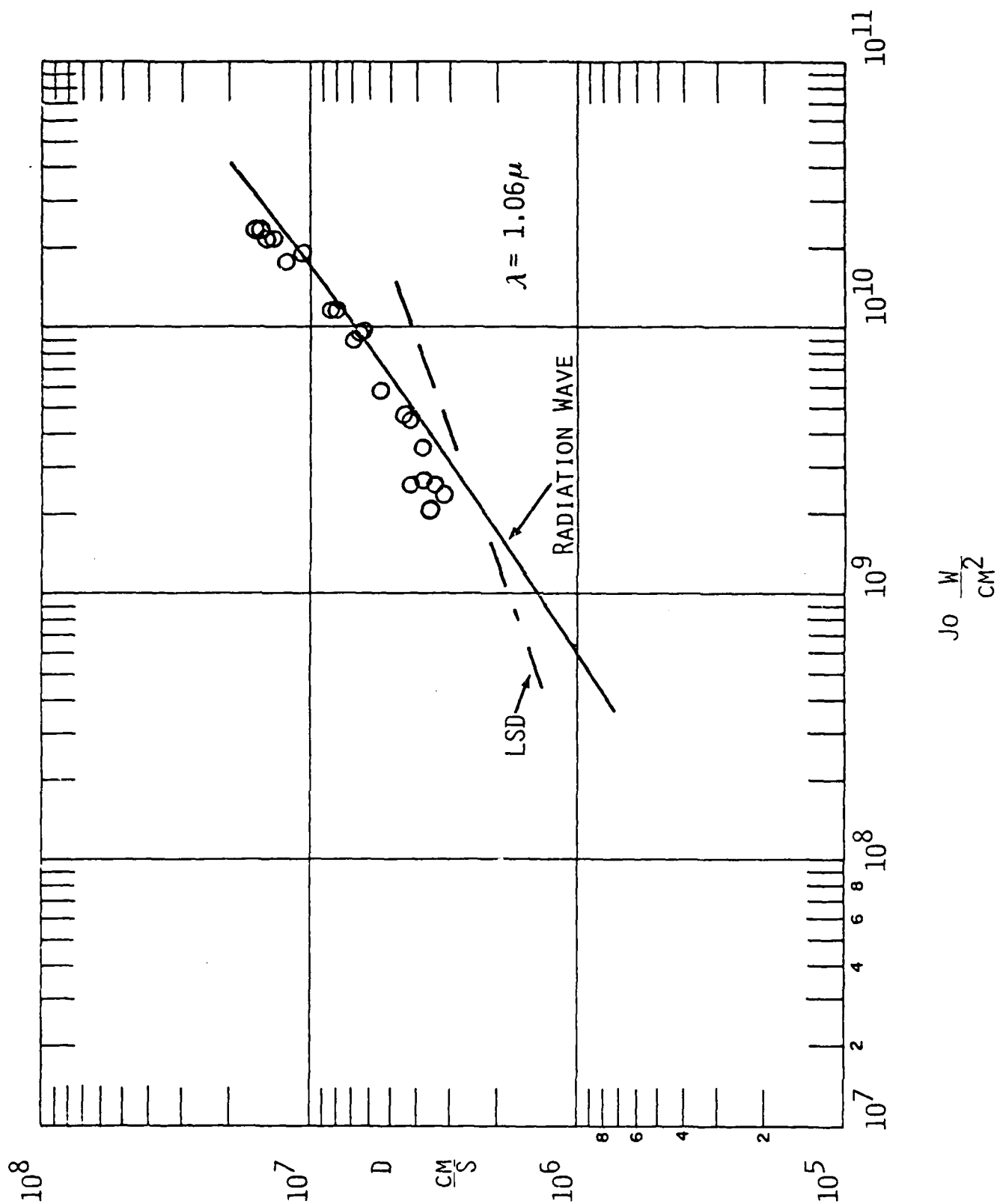


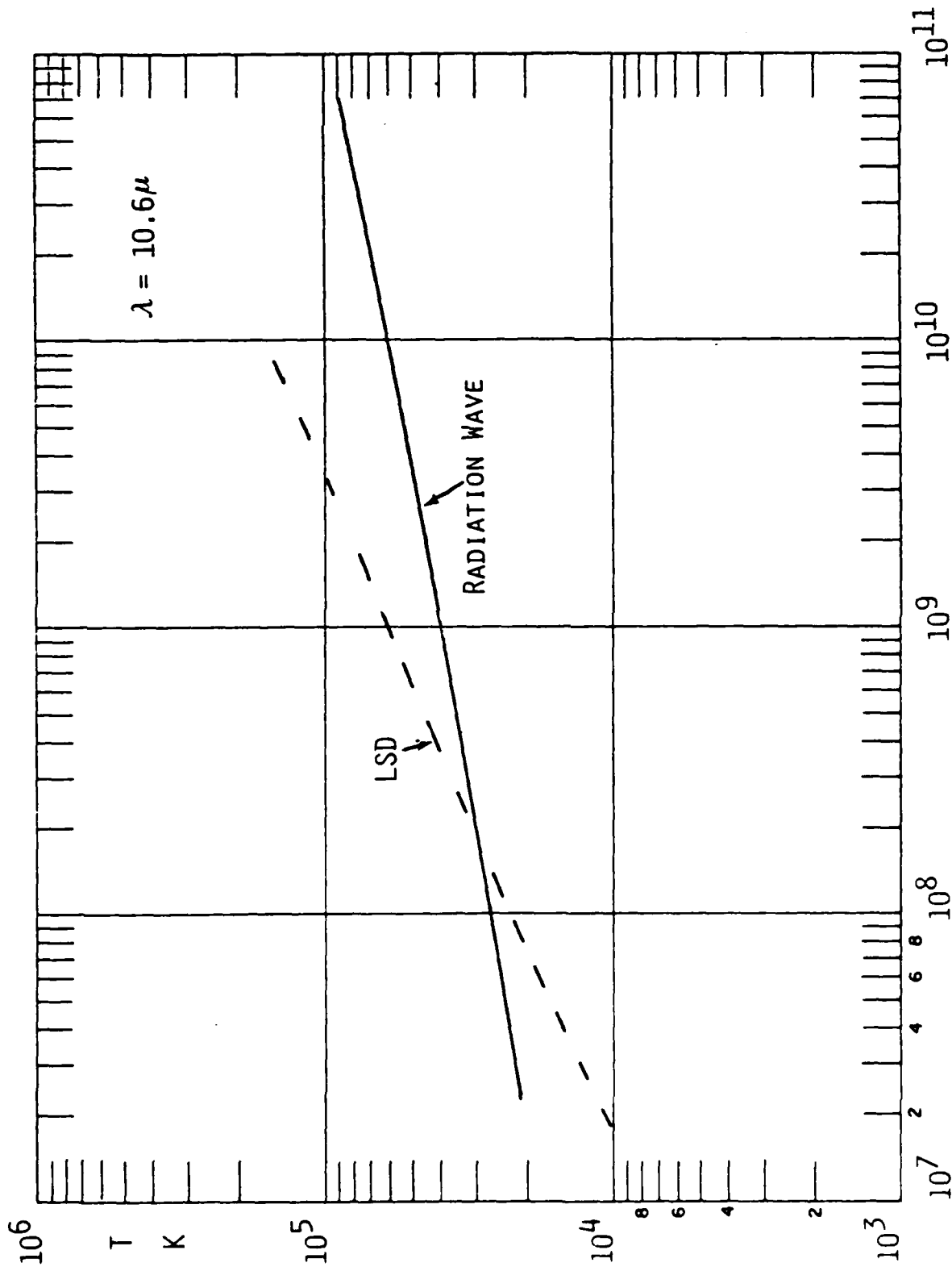
Fig. 4.5 Theory and Experiment.

locked giving rise to a modulated laser intensity. The radiation level is very sensitive to this variation as it scales the gas temperature to the fourth power. In evaluating this effect it is assumed that the fluctuations are sufficiently fast ($\tau_f \sim 10$ ns) compared to the propagation time scale, which is approximately the absorption length of the hot gas radiation in the air out front divided by the wave velocity $\sim \frac{10^{-1} \text{cm}}{10^6 \text{cm/s}}$, that the wave velocity does not react to the fluctuations instantaneously but rather only through a perceived higher emissivity. As the absorption length in the air has only been estimated this may be a poor approximation and should be considered as the maximum effect these fluctuations can have. We define an effective emissivity multiplier as $\epsilon_m = \frac{\langle T_f^4 \rangle}{\langle T_f \rangle^4}$ and evaluate these time averages by approximating the energy equation as $\rho_0 D e_f = J_0$ where e_f and J_0 are functions of time but not $\rho_0 D$. e_f is related to T_f by an approximate equation of state

$$e_f = C_v T_f^{3/2}$$

Thus $T_f \sim J_0^{2/3}$ and $\epsilon_m = \frac{\langle J_0^{8/3} \rangle}{\langle J_0 \rangle^{8/3}}$. If we assume a pulse shape as shown in Fig. 4.2b then $\epsilon_m = 2.22$. With this value of ϵ_m , a value of ϵ of 1, and $e^* = 0.5$ eV the velocity and temperature for a 10.6μ radiation driven wave has been calculated and is shown in Figs. 4.5 and 4.6. This calculation for velocity is compared with data taken on the NRL device in Fig. 4.7. The analysis of the data from NRL is described in Section 4.1.

The calculations following Bergel'son et. al. just described for 1.06μ and 10.6μ may be considered as placing approximate limits on the intensity region in which supersonic radiation waves are expected to be found, in as much as the 10.6μ predictions were performed for a minimum value for T^* and what is probably a maximum value for ϵ_m and the 1.06μ calculation prediction was performed for what is probably a maximum value for temperature. The measured velocity for the 1.06μ data is in good agreement with theory indicating that radiation is the important propagation mechanism in this intensity region. The 10.6μ data again leads to this conclusion, but here the agreement is not so good with the measured velocities even faster than those predicted using this simple theory.



$$Jo \frac{W}{CM^2}$$

Fig. 4.6 Supersonic radiation wave.

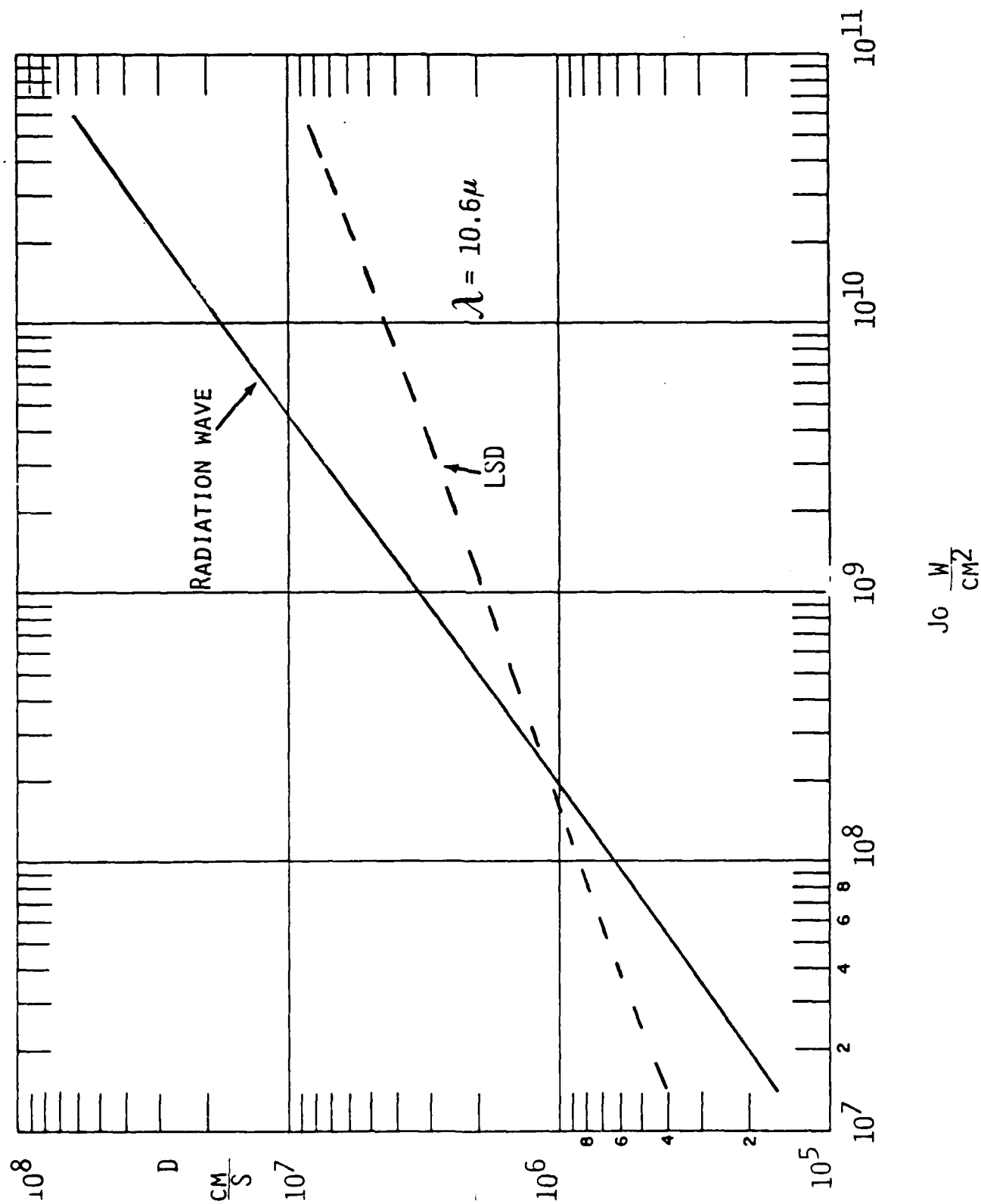


Fig. 4.7 Supersonic radiation waves 10.6μ

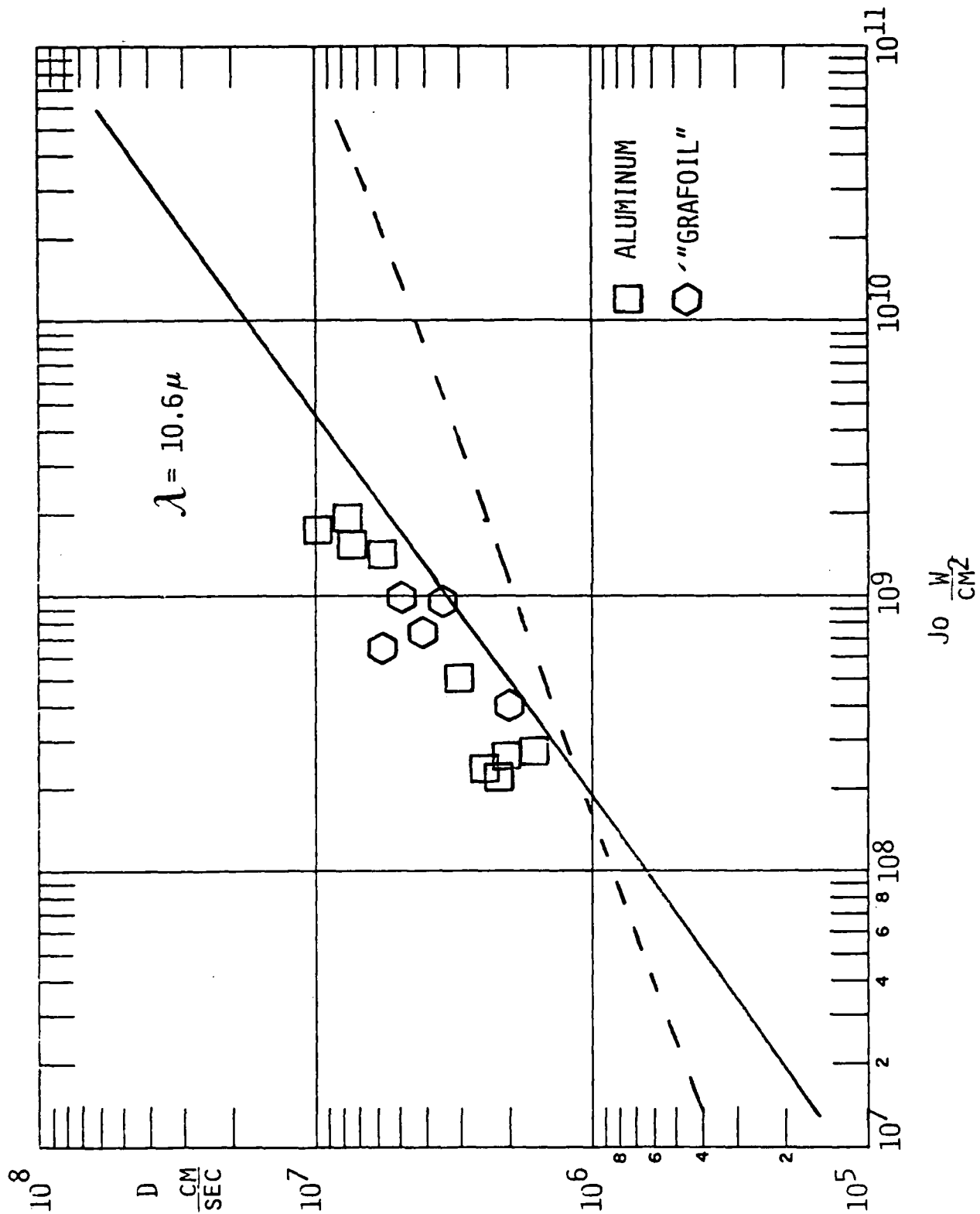


Fig. 4.8 Theory and experiment 10.6μ .

4.1 Analysis of Streak Photograph Data

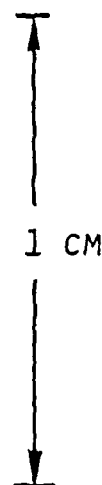
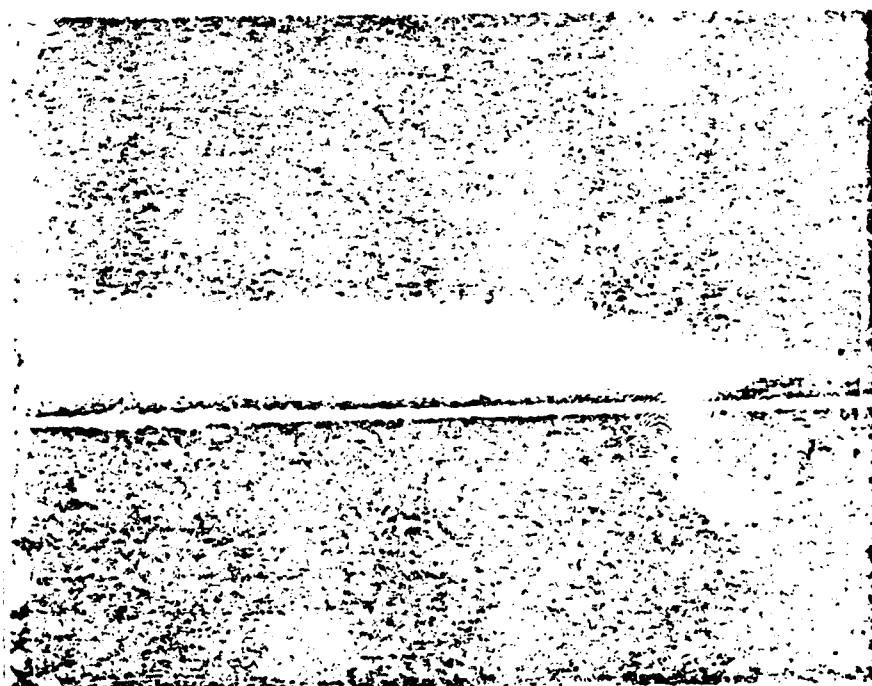
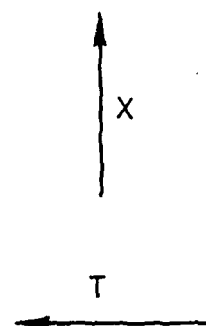
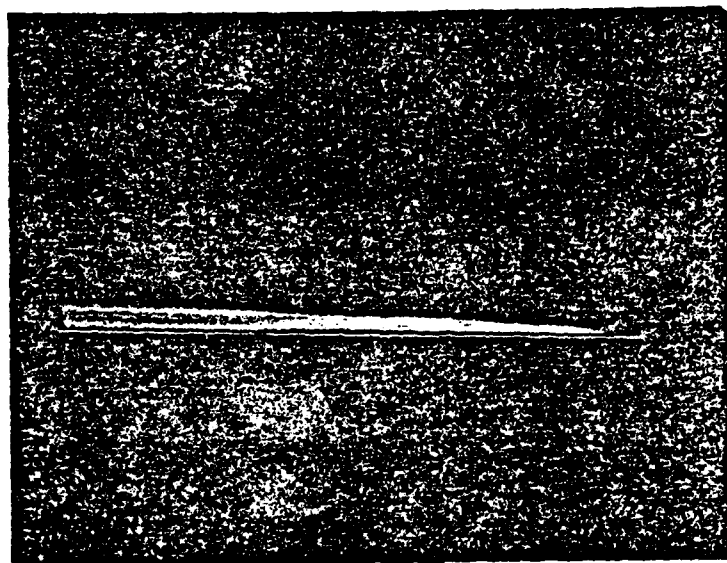
The analysis of the streak photograph data began with enlarging the streak photographs as shown in Fig. 4.9. As seen the luminous front moves at a very rapid velocity at early times, while the laser is on, followed by a considerably lower velocity at later times, when the laser is off. This is shown more clearly in Fig. 4.10 which plots distance versus time for the first few hundred ns from the photograph of Fig. 4.9.

For two of the runs at the highest intensity, $I = 2 \times 10^9 \frac{\text{W}}{\text{cm}^2}$, the distance that the front moved during the laser pulse was sufficient that the derivative of the distance versus time curve could be taken and such a velocity plot is shown in Fig. 4.11. For comparison the laser intensity is also shown in this figure. There is no time index on the streak pictures so that the time axis for the velocity has been arbitrarily positioned to place the maximum velocity at the point in time of maximum intensity. This positioning would lead to an ignition time of 40 ns, a very reasonable value.

For runs at lower intensity an approximate maximum slope was measured as well as the position of the front at a fixed time, taken to be 200 ns. For the lowest intensities only the position of the front at the fixed time could be determined with any degree of accuracy. Therefore the position of the front at fixed time was correlated to the slope velocity and the peak velocity as measured on the two highest intensity runs. This correlation is shown in Fig. 4.12. Using this correlation peak velocities have been determined from the distance at the fixed time for all laser intensities. These peak velocities have been plotted versus peak intensities from reference 1 in Fig. 4.8 and compared with theory.

STREAK PHOTOGRAPHS

RUN #178
3 CM SPOT



200 NS 100 NS 0

Fig. 4.9 Streak photographs.

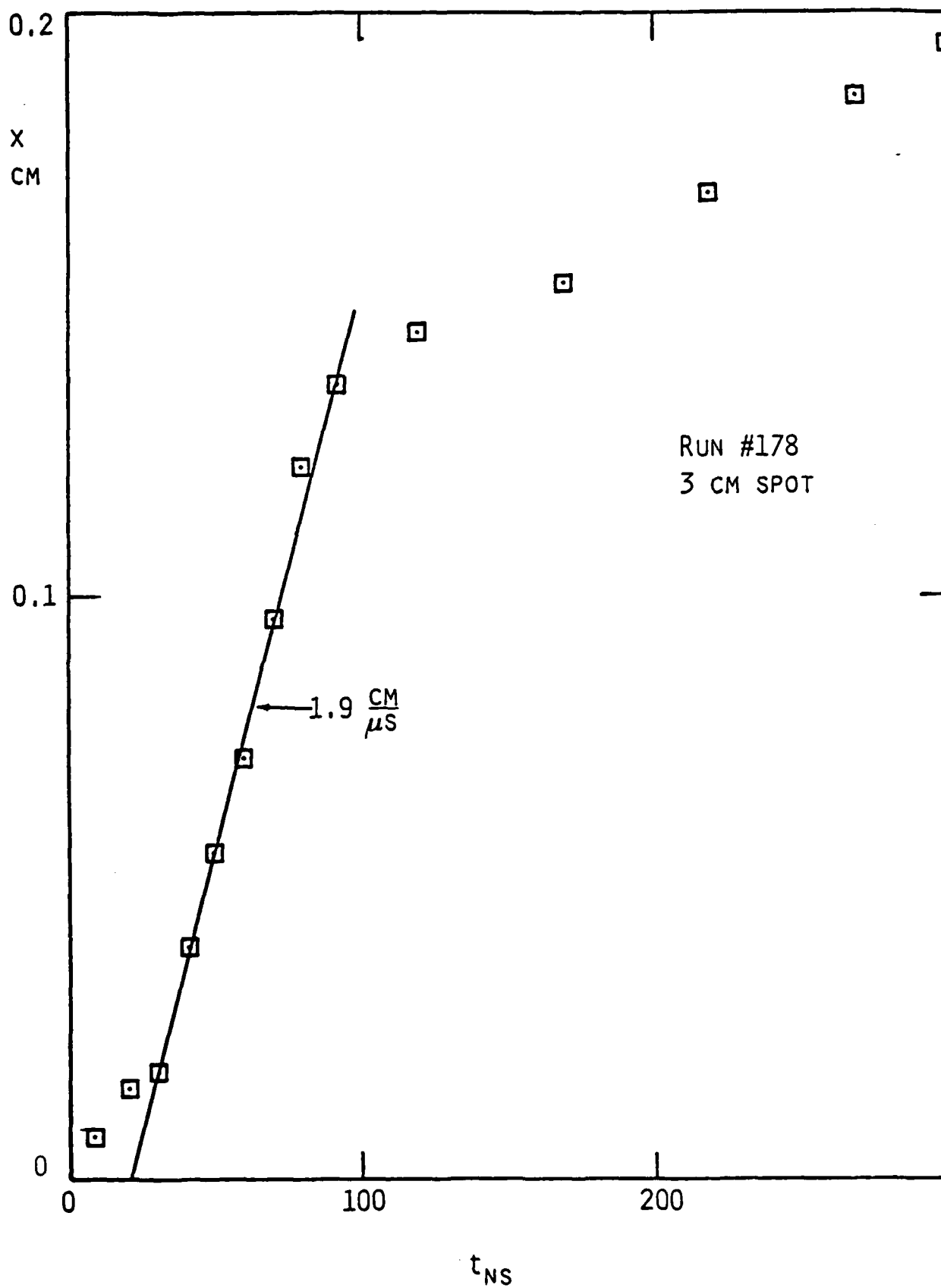


Fig. 4.10 Distance vs. velocity.

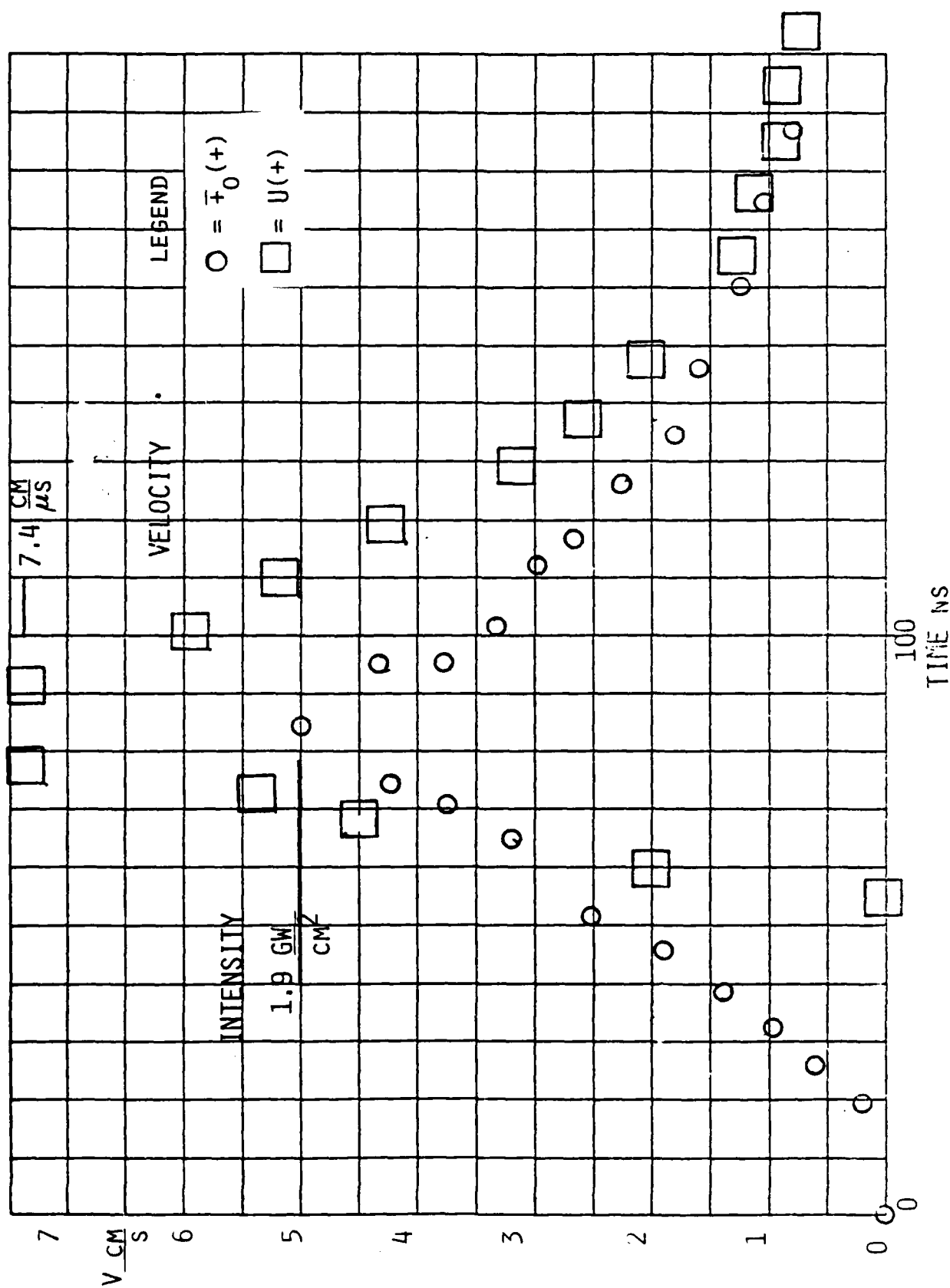


Fig. 4.11 Velocity as function of time.

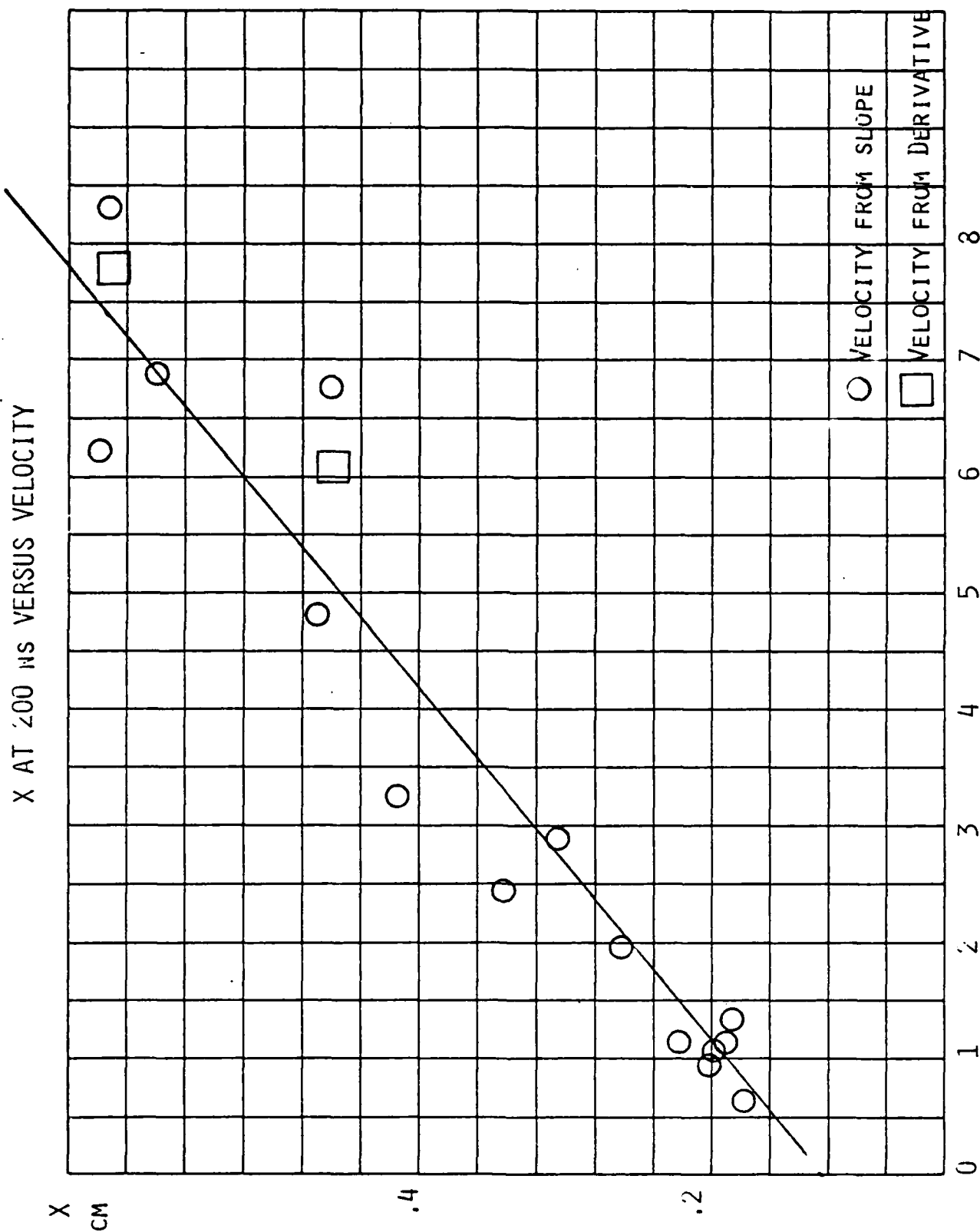


Fig. 4.12 X at 200 ns versus velocity.

SUPERSONIC RADIATION WAVES
REFERENCES

1. V. I. Bergel'son, T. V. Loseva, I. V. Nemchinov and T. I. and T. I. Orlova., "Propagatin of plane supersonic radiation waves," Sov. J. Plasma Phys., Vol. 1, No. 6, Nov.-Dec. 1975.
2. To be published.
3. G. Weyl, A. Pirri, R. Root, "Laser Ignition of Plasma off Aluminum Surfaces," AIAA Journal, Vol. 19, No. 4, April 1981, p. 460.

APPENDIX A

SYMPTOTIC THEORY FOR THE MOMENTUM TRANSFER
TO A SURFACE WHEN IRRADITATED BY A HIGH POWER LASER

ASYMPTOTIC THEORY FOR THE MOMENTUM TRANSFER
TO A SURFACE WHEN IRRADIATED BY A HIGH POWER LASER

GIRARD A. SIMONS

PHYSICAL SCIENCES INC.
RESEARCH PARK
ANDOVER, MA 01810

ABSTRACT

A simplified model is developed to predict the impulse imparted to a surface when irradiated by a high power laser. A high pressure plasma is created by a laser supported detonation (LSD) wave traveling toward the energy source. The multi-dimensional expansion of the high pressure region is described by patching one, two and three-dimensional blast wave solutions to the LSD wave. The patching times are obtained by conserving energy between the wave solutions and are shown to be different from those used by previous authors. The pressure-time-space results are integrated to determine the net impulse delivered to the surface. A simplified procedure is outlined for converting target failure criterion to laser parameter requirements.

1. INTRODUCTION

When a single pulse high power laser irradiates a target surface, a laser supported detonation wave (LSD) forms above the target surface and propagates into the background gas. The high pressure gas behind the LSD wave transfers momentum to the target and represents a potential damage mechanism. A measure of the efficiency with which momentum is imparted to the target is the coupling coefficient, defined as the impulse per unit laser energy. Several authors⁽¹⁻⁴⁾ have sought to evaluate and optimize the coupling coefficient with respect to the laser beam diameter, pulse duration and energy.

The impulse imparted to the target during irradiation is a small fraction of the total impulse delivered. Hence, an accurate description of the momentum transfer must include the decay of the LSD wave into a hydrodynamic blast wave. The transition from an LSD wave to a blast wave has been described^(1,3,4) by patching the blast wave and LSD wave solutions together at an intermediate time. Hydrocode simulations⁽²⁾ have confirmed this approach but a unique choice for the patch time was not established. It is shown herein that various choices for the patch time results in variations in the energy in the blast wave. Since the energy in the blast wave must be equal to the laser energy deposited in the LSD wave, the patch time may be established by specifying the energy in the asymptotic blast wave. Using this technique to determine the patch time, it is shown that the laser energy required to deliver a fixed impulse to a target may, in some limits, be a factor of five greater than previously assessed.

2. PATCHED SOLUTIONS

The high pressure plasma generated by the LSD wave imparts momentum to the target until a relaxation wave penetrates the plasma from the surrounding low pressure ambient environment. The relaxation may occur from the axial (laser beam) direction in time τ_z or laterally in time τ_{2D} . The time scales τ_z and τ_{2D} , and the pressure decay laws between these time scales, control the total momentum imparted to the target by the laser. The LSD wave is patched to conventional one, two and three-dimensional blast wave solutions at the times, τ_z and τ_{2D} . The patching sequence varies with the relative magnitude of these time scales.

If the axial relaxation time τ_z is less than τ_{2D} (Case I) the LSD wave will propagate at constant velocity and pressure until time τ_z when the wave forms a one-dimensional blast wave (1DBW). The 1DBW will propagate to time τ_{2D} , at which time it will form a three-dimensional blast wave (3DBW). These patched solutions are normalized to pressure p_s which represents the pressure of the LSD wave on the surface of the target. For Case I,

$$t < \tau_z : p = p_s, \quad \text{LSD} \quad (1)$$

$$\tau_z < t < \tau_{2D} : p = p_s \left(\frac{\tau_z}{t} \right)^{2/3}, \quad \text{1DBW} \quad (2)$$

$$\tau_{2D} < t : p = p_s \left(\frac{\tau_z}{\tau_{2D}} \right)^{2/3} \left(\frac{\tau_{2D}}{t} \right)^{6/5}, \quad \text{3DBW} \quad (3)$$

Similarly, for $\tau_{2D} < \tau_z$ (case II), the LSD wave forms a two-dimensional blast wave (2DBW) at time τ_{2D} and a 3DBW at time τ_z . The solutions for the pressure in case II are

$$t < \tau_{2D} : p = p_s, \quad 1\text{DLSD} \quad (4)$$

$$\tau_{2D} < t < \tau_z : p = p_s \left(\frac{\tau_{2D}}{t} \right), \quad 2\text{DBW} \quad (5)$$

$$\tau_z < t : p = p_s \left(\frac{\tau_{2D}}{\tau_z} \right) \left(\frac{\tau_z}{t} \right)^{6/5}, \quad 3\text{DBW} \quad (6)$$

The critical element in utilizing the patched solution is that of specifying τ_z and τ_{2D} . Pirri⁽¹⁾ required that axial relaxation occurred when the laser pulse terminated, i.e., τ_z equals the duration of the laser pulse, τ_p . Ferriter⁽²⁾ argued that axial relaxation could not occur until an acoustic wave traveled from the LSD wave to the target surface, notifying the target that the laser pulse was off. Neglecting the finite velocity of the gas behind the LSD wave, Ferriter obtained $\tau_z = 2.83 \tau_p$ whereas τ_z is shown to be $3.23 \tau_p$ when the finite velocity of the gas is included.⁽⁴⁾ Similar arguments have been utilized to evaluate τ_{2D} . Since the velocity of sound behind an LSD wave is of the order of the velocity of the wave, V_w , τ_{2D} is of the order of R_s/V_w where R_s is the radius of the irradiated spot.

The above choices for τ_z and τ_{2D} do not insure that the asymptotic description of the blast wave is valid. The blast wave solution for the pressure may be expressed as $p(E, t)$ where E is the deposition energy. Various

choices for τ_z and τ_{2D} in Eqs. (2), (3), (5), and (6) will inadvertently alter the energy in the blast wave. This suggests that there must be appropriate values of τ_z and τ_{2D} that constrain the energy in the blast wave to be equal to that deposited by the LSD wave. Below, the values of the patch times are determined via this criterion. In some cases, the patch times and blast wave solutions are distinctly different from those discussed above.

3. ASYMPTOTIC EVALUATION OF THE PATCHING TIMES

The variables in the patched pressure solutions [Eqs. 1-6] are determined directly from the LSD and blast wave solutions. The LSD wave is expressed in terms of the laser intensity I_0 , gas density ρ , and the ratio of specific heats γ . The velocity v_w and pressure p_w of the LSD wave,⁽⁵⁾ and the pressure p_s on the target⁽¹⁾ are

$$v_w = a_1 (I_0 / \rho)^{1/3} ,$$

$$p_w = a_2 (I_0^2 \rho)^{1/3} ,$$

and

$$p_s = a_3 (I_0^2 \rho)^{1/3} ,$$

respectively, where

$$a_1 = [2(\gamma^2 - 1)]^{1/3} ,$$

$$a_2 = a_1^2 / (\gamma + 1) ,$$

and

$$a_3 = \left(\frac{\gamma + 1}{2\gamma} \right)^{\frac{2\gamma}{\gamma - 1}} a_2 .$$

The time scale τ_2 may be obtained from Eq. (2) and the known⁽⁶⁾ 1DBW solution for the pressure at the point of the energy deposition

$$p \doteq 0.11 \rho \left(\frac{E_1}{\rho t} \right)^{2/3} ,$$

where the constant has been evaluated for $\gamma = 1.2$ and E_1 is the energy per unit area deposited by the laser

$$E_1 = I_0 \tau_p .$$

The above expression for $p(E_1, t)$ at the target surface is identical to that given by Eq. (2) if and only if

$$\tau_z = \alpha \tau_p \quad (\text{Case I}) \quad (7)$$

where

$$\alpha \doteq 0.6 ,$$

for $\gamma = 1.2$.

Note that the axial relaxation time is less than the laser pulse duration. This is clearly incorrect when viewed locally at time τ_p . However, the dominant momentum transfer occurs during the asymptotic portion of the blast wave and the local details are sacrificed in order to accurately predict the asymptotic behavior.

When the lateral relaxation time is short compared to the axial relaxation time, a cylindrical blast wave forms above the target surface while the LSD wave continues to move toward the laser. The energy deposited per unit length perpendicular to the target surface is

$$E_2 = I_0 \pi R_s^2 / V_w .$$

and the asymptotic blast wave solution is⁶

$$p \doteq 0.05 \rho \left(\frac{E_2}{\rho} \right)^{1/2} \frac{1}{t}$$

for $\gamma = 1.2$. Comparing this expression for $p(E_2, t)$ to Eq. (5), τ_{2D} becomes

$$\tau_{2D} \doteq \alpha R_s / V_w, \quad (\text{Case II}) \quad (8)$$

which is again slightly shorter than one would assess from a local analysis.

The axial relaxation time τ_z , as given by Eq. (7), is valid only for $\tau_z < \tau_{2D}$, whereas the lateral relaxation time τ_{2D} , as given by Eq. (8), is valid only for $\tau_{2D} < \tau_z$. In both cases, the expansion fan propagates through the hot, high density gas with a velocity approximately equal to V_w . The length scales corresponding to τ_z and τ_{2D} are $V_w \tau_p$ and R_s , respectively. Hence, the relaxation times are approximately τ_p and R_s/V_w , respectively.

If the lateral relaxation occurs first, the axial relaxation τ_z must be greater than given by Eq. (7) because the axial expansion is now occurring in a colder, lower density gas. Similarly, if the axial relaxation occurs first, the lateral relaxation time τ_{2D} must be greater than given by Eq. (8) because now the lateral expansion is occurring in a colder, lower density gas. To evaluate these limits, both Eqs. (3) and (6) are required to be identical to the asymptotic 3DBW solution. This requirement yields

$$\tau_{2D} = \alpha \left[\frac{R_s^3}{\tau_p^3 V_w^3} \right]^{1/2} \quad (\text{Case I}) \quad (9)$$

and

$$\tau_z = \alpha V_w \tau_p^2 / R_s. \quad (\text{Case II}) \quad (10)$$

Equations (7)-(10) represent a complete set of time scales for the patched pressure solutions [Eqs. (1)-(6)] and clearly define the range of validity of Case I and Case II in terms of the known variables τ_p , R_s and V_w .

Case I ($\tau_z < \tau_{2D}$): $\tau_p < R_s/V_w$

Case II ($\tau_{2D} < \tau_z$): $R_s/V_w < \tau_p$

The solution for the total momentum imparted to a target surface may be generated through spatial and temporal integrations of the patched pressure solutions. To accomplish this, patched solutions for the spatial extent of the blast wave must first be developed.

4. PATCHED SOLUTIONS FOR THE SPATIAL EXTENT OF THE BLAST WAVES

The expressions for the lateral extent of the high pressure zone are obtained by again patching blast wave solutions. For $\tau_z < \tau_{2D}$ (Case I), the lateral coordinate R is equal to the spot radius R_s during the LSD wave and the 1DBW, followed by the 3DBW solution for $t > \tau_{2D}$. This is expressed as

$$t < \tau_{2D} : R = R_s , \quad \text{LSD, 1DBW} \quad (11)$$

and

$$\tau_{2D} < t : R = m_1 R_s \left(\frac{t}{\tau_{2D}} \right)^{2/5} , \quad \text{3DBW} \quad (12)$$

where m_1 is a constant of order unity. Equation (12) is identical to the 3DBW solution if and only if

$$m_1 \doteq 1.0 .$$

Similarly, for Case II ($\tau_{2D} < \tau_z$), the lateral extent of the high pressure zone is given by

$$t < \tau_{2D} : R = R_s , \quad \text{LSD} \quad (13)$$

$$\tau_{2D} < t < \tau_z : R = m_2 R_s \left(\frac{t}{\tau_{2D}} \right)^{1/2} , \quad \text{2DBW} \quad (14)$$

$$\tau_z < t : R = m_3 R_s \left(\frac{\tau_z}{\tau_{2D}} \right)^{1/2} \left(\frac{t}{\tau_z} \right)^{2/5} . \quad \text{3DBW} \quad (15)$$

Matching the above blast wave solutions to the conventional solutions⁶ yields

$$m_2 \doteq 1.0$$

and

$$m_3 \doteq 1.0.$$

The 2DBW solution appropriate to Case II is valid if and only if the two-dimensional shock radius R is less than or equal to the target radius R_t . Beyond R_t , the blast wave becomes three-dimensional, independent of τ_z . Defining τ_e as the time at which $R = R_t$, Eq. (14) yields

$$\tau_e = \alpha R_t^2 / R_s V_w, \quad (16)$$

and the Case II solutions are valid only if $\tau_z < \tau_e$. In this limit, the blast wave undergoes transition from 2D to 3D before it reaches the edge of the target.

Whenever $\tau_e < \tau_z$, the blast wave undergoes transition from 2D to 3D at the edge of the target, prior to time τ_z . In this limit, modifications to the Case II solutions are necessary. The 3DBW solution must be continuous with Eqs. (5) and (14) at $R = R_t$. The 3D solutions become

$$P = P_s \left(\frac{\tau_{2D}}{\tau_e} \right) \left(\frac{\tau_e}{t} \right)^{6/5} \quad \text{3DBW} \quad (17)$$

and

$$R = R_s \left(\frac{\tau_e}{\tau_{2D}} \right)^{1/2} \left(\frac{t}{\tau_e} \right)^{2/5}, \quad \text{3DBW} \quad (18)$$

respectively. This solution does not allow the laser and blast wave energies to be identical. Laser energy is still being deposited by the LSD wave when

the cylindrical blast wave reaches the edge of the target. Only that portion of the laser energy deposited in time τ_e is contained in the 3DBW.

The above limit suggests that Case II can be restricted to $\tau_{2D} < \tau_z < \tau_e$ and Case III be defined to describe the limit of $\tau_e < \tau_z$. Expressions for τ_z and τ_{2D} appropriate to Case III are identical to those in Case II. The Case III solutions for $p(t)$ and $R(t)$ are the Case II solutions, with Eqs. (17) and (18) replacing Eqs. (6) and (15), respectively. The time at which the 2DBW solution transforms into a 3DBW is now τ_e rather than τ_z . The Case I, II, and III solutions are illustrated in Figs. 1-3, respectively, and have been expressed in a form that will be used to determine the net momentum transferred to the target.

5. MOMENTUM IMPARTED TO THE TARGET

The total impulse (I) imparted to the target is the spatial and temporal integral of the pressure times the area.

$$I = \int_{\text{all } t} \int_0^R p(t) 2\pi r dr dt . \quad (19)$$

The patched solutions for $p(t)$ and $R(t)$ are illustrated in Figs. 1-3 for laser pulses of increasing time duration. The Case I solutions, appropriate for short laser pulses, are illustrated in Fig. 1 and depict an LSD wave transforming into a 1DBW at τ_2 and then into a 3DBW at τ_{2D} . For intermediate pulses (Fig. 2), the LSD wave transforms into a 2DBW and then into a 3DBW before reaching the edge of the target. The long pulse solution (Fig. 3) is identical to the intermediate pulse, except the 2DBW reaches the edge of the target before decaying into a 3DBW. Spatial integration of the pressure over the target surface must be terminated at either the laser spot radius R_s , blast wave radius R , or the target radius R_t , whichever is appropriate at time t . Time integrations must be terminated at the value of time for which $p(t)$ decreases to the ambient value, p_∞ . There are eight distinct subcases corresponding to different values of the ambient pressure in each of the three cases. They are

- Case Ia : $p \rightarrow p_\infty$ in 1DBW,
- Case Ib : $p \rightarrow p_\infty$ in 3DBW with $R < R_t$,
- Case Ic : $p \rightarrow p_\infty$ in 3DBW with $R > R_t$,
- Case IIa : $p \rightarrow p_\infty$ in 2DBW,
- Case IIb : $p \rightarrow p_\infty$ in 3DBW with $R < R_t$,
- Case IIc : $p \rightarrow p_\infty$ in 3DBW with $R > R_t$,

Case IIIa: $p \rightarrow p_\infty$ in 2DBW,

and

Case IIIb: $p \rightarrow p_\infty$ in 3DBW .

Each subcase corresponds to different values of the laser and target parameters. The laser parameters specify the target surface pressure p_s , wave velocity V_w , pulse duration τ_p and spot size R_s . The regions of parameter space corresponding to each subcase are illustrated in Fig. 4. Before elaborating on the solutions corresponding to each of the eight subcases, it is appropriate to discuss the approximations made in the spatial and temporal integrations of Eq. (19).

The pressure immediately behind the blast wave, p_w , is generally a factor of three greater than that at the target surface, p_s . Since the pressure decays quite rapidly behind the blast wave, the high pressure region of the pulse is not included in the spatial integration of Eq. (19). This approximation is extremely accurate when the blast wave expands beyond the target and only the uniform pressure, p_s , is applied to the target. However, the impulse can be underestimated by "order one" if the blast wave does not expand beyond the target [cases Ib, IIa, IIb, IIIa].

The temporal integration of Eq. (19) is terminated when the pressure on the target surface decays to the ambient value. However, the blast wave solution is valid only for strong shocks ($p_s \gg p_\infty$) and underestimates the pressure as $p_s \rightarrow p_\infty$. This results in an underestimate of the impulse which is appreciable ("order one") only if the integral of $prdr$ is dominated by the limit at p_∞ . This occurs only when the blast wave does not expand beyond the target surface as in the cases cited above.

The impulse calculations should also include the negating effect of the ambient pressure opposing that of p_s on the opposite side of the target.⁽⁴⁾ This is appreciable (again, "order one") when the integral of $prdr$ is dominated by the limit at p_∞ , i.e., for the same cases as cited above. While this tends to cancel the two effects considered above, one should expect as much as 50% errors for these cases.

Recognizing the approximations involved, the eight solutions for the total impulse imparted to the target are given below. It is straightforward to calculate p_s/p_∞ , R_t/R_s , $V_w \tau_p/R_s$ and utilize Fig. 4 to determine which of the following solutions is appropriate.

Defining

$$\zeta = \frac{\dot{I}}{p_s \pi R_s^2 \tau_p \alpha}, \quad (20)$$

and

$$\zeta^* = 5 \left(\frac{R_t}{R_s} \right)^{3/2} \left(\frac{R_s}{V_w \tau_p} \right)^{1/2} \left[\frac{4}{3} - \left(\frac{\left(\frac{R_t}{R_s} \right)^3 \left(\frac{R_s}{V_w \tau_p} \right)}{p_s/p_\infty} \right)^{1/6} \right], \quad (21)$$

the solutions are

$$\text{Case Ia: } \zeta = 3 \left(\frac{p_s}{p_\infty} \right)^{1/2} - 2 \quad (22)$$

$$\text{Case Ib: } \zeta = \frac{5}{3} \left(\frac{p_s}{p_\infty} \right)^{1/2} + \frac{4}{3} \left(\frac{R_s}{V_w \tau_p} \right)^{1/2} - 2 \quad (23)$$

$$\text{Case Ic: } \zeta = \zeta^* + \frac{4}{3} \left(\frac{R_s}{V_w \tau_p} \right)^{1/2} - 2 \quad (24)$$

$$\text{Case IIa: } \zeta = \left(\frac{P_s}{P_\infty}\right) \left(\frac{R_s}{V_w \tau_p}\right) \quad (25)$$

$$\text{Case IIb: } \zeta = \frac{5}{3} \left(\frac{P_s}{P_\infty}\right)^{1/2} - \frac{2}{3} \left(\frac{V_w \tau_p}{R_s}\right) \quad (26)$$

$$\text{Case IIc: } \zeta = \zeta^* - \frac{2}{3} \left(\frac{V_w \tau_p}{R_s}\right) \quad (27)$$

Case IIIa: Same as IIa

$$\text{Case IIIb: } \zeta = 5 \left(\frac{R_s}{V_w \tau_p}\right) \left(\frac{R_t}{R_s}\right)^2 \left[\frac{6}{5} - \left(\frac{(R_t/R_s)^2}{P_s/P_\infty} \right)^{1/6} \right] \quad (28)$$

The various solutions tabulated above illustrate that there is a variety of functional relationships between impulse, pulse duration, wave velocity, spot radius and target radius. Although the solution in each regime is relatively simple, the boundaries between the regimes are also variable and it is impossible to determine a general scaling law. A simple computer program has been written which utilizes Fig. 4 to determine the appropriate case and then calculates impulse using the corresponding analytic solution. Results are illustrated in Fig. 5 and are compared to the data of Kozlova et al.⁽⁷⁾ The theoretical predictions agree with data if one assumes that 50% of the laser energy is absorbed by the gas. The particular point to emphasize here is the confirmation of the value of 0.6 for the constant α . Impulse scales as $1/\alpha$ for all cases. Local theories^(2,4) predict that the value of α is of the order of three and the corresponding impulse predictions (via this model) are a factor of five higher. This would be consistent with the data if and only if the energy conversion efficiency were reduced to 10%.

The reader should be cautioned against concluding that the predictions of Ref. 4 are always a factor of five higher than those obtained here. There are several differences between the spatial and temporal solutions of the two models and there is only one limit (case Ia with $R_s = R_t$) in which this factor of five is completely apparent.

6. TARGET DAMAGE OPTIMIZATION

The analytic solutions for the impulse imparted by a high energy laser make it relatively easy to study the effects of parametric variation. Consider the laser energy E_0 , pulse duration τ_p and spot radius R_s as the independent laser parameters. The beam intensity I_0 is expressed as

$$I_0 = \frac{E_0}{\pi R_s^2 \tau_p},$$

and the wave velocity and target surface pressure become

$$v_w = a_1 \left(\frac{E_0}{\pi R_s^2 \tau_p \rho} \right)^{1/3},$$

and

$$p_s = a_3 \rho^{1/3} \left(\frac{E_0}{\pi R_s^2 \tau_p} \right)^{2/3},$$

respectively. The total impulse can, for every case, be expressed as

$$I = I(E_0, \tau_p, R_t, R_s/R_t). \quad (29)$$

Ferriter⁽²⁾ noted that maximum impulse is delivered when the laser beam diameter matches the size of the target ($R_s = R_t$). Expressing the total impulse imparted to a particular target R_t in the form of Eq. (29), it can be shown that all expressions for I [Eqs. (22)-(28)] approach a maximum as $R_s \rightarrow R_t$. However, the regimes in which these solutions are valid also vary with R_s/R_t and this variation is not considered in the comparison. The results of the complete model are illustrated in Fig. 6 for a 10^4 joule laser

irradiating a 10 cm target. These calculations clearly demonstrate that maximum impulse is imparted when the target is flood loaded ($R_s = R_t$). Such a conclusion is, of course, subject to the constraint that R_s is not so large as to reduce the beam intensity below the LSD threshold, nor is R_s so small that the plasma is overdense.

In the limit of $R_s = R_t$, Fig. 4 reduces to three regions corresponding to Cases Ia, Ic and IIIb. The expressions for the impulse per unit area under the spot are obtained by rewriting Eqs. (22), (24), and (28), retaining only the leading term:

$$\text{Case Ia: } \frac{I}{A} = 3\alpha p_s \tau_p \left(\frac{p_s}{p_m} \right)^{1/2},$$

$$\text{Case Ic: } \frac{I}{A} = 8\alpha p_s \tau_p \left(\frac{R_s}{v_w \tau_p} \right)^{1/2},$$

$$\text{Case IIIb: } \frac{I}{A} = \frac{6\alpha p_s R_s}{v_w}.$$

Structural failure of a target requires that the imparted impulse I/A exceeds some minimum value corresponding to some minimum pressure p_s . A typical failure curve is illustrated in Fig. 7. All combinations of p_s and I/A in excess of the critical level (curve ABCD) will insure failure. Since I/A and p_s are known functions of (E_0, τ_p, R_s) , it is relatively straightforward to invert the solutions to determine the E_0 and τ_p required to yield a specific combination of I/A and p_s on spot radius R_s . The inversions yield

$$\text{Case Ia: } E_o = \frac{\pi R_s^2 (I/A)}{3 \alpha a_3} \left(\frac{p_\infty}{\rho a_3} \right)^{1/2}, \quad (30)$$

$$\tau_p = \frac{(p_\infty)^{1/2} (I/A)}{3 \alpha p_s^{3/2}}, \quad (31)$$

$$\text{Case Ic: } E_o = \frac{\pi R_s a_1 (I/A)^2}{64 \alpha^2 \rho a_3^2}, \quad (32)$$

$$\tau_p = \frac{a_1 (I/A)^2}{64 \alpha^2 p_s^{3/2} R_s (\rho a_3)^{1/2}}, \quad (33)$$

$$\text{Case IIIb: } \frac{E_o}{\tau_p} = \frac{\pi R_s^2 p_s^{3/2}}{a_3 (\rho a_3)^{1/2}}, \quad (34)$$

$$\text{on } \frac{I}{A} = \frac{6 \alpha R_s (\rho a_3 p_s)^{1/2}}{a_1}. \quad (35)$$

Cases Ia and Ic correspond to regions in $(I/A, p_s)$ space separated by

$$\frac{I}{A} = \frac{64 \alpha R_s (p_\infty \rho a_3)^{1/2}}{3 a_1}, \quad (36)$$

whereas Case IIIb reduces to a single curve in $(I/A, p_s)$ space corresponding to particular values of E_o/τ_p . The regions are illustrated in Fig. 7. Parameter space $(p_s, I/A)$ is separated into the three regions by direct application

of Eqs. (35) and (36). That portion of the failure curve denoted by AB corresponds to Case Ia. This portion of the failure curve may be transformed into (E_0, τ_p) space via Eqs. (30) and (31). Similarly, curve BC corresponds to Case Ic and may be transformed into (E_0, τ_p) space via Eqs. (32) and (33). The single point on the failure curve denoted by C corresponds to a particular value of E_0/τ_p [Eq. (34)] and completes transformation of the failure curve into (E_0, τ_p) space. [Note that there is no binary combination of laser energy and pulse duration that can achieve the conditions on curve CD].

A relatively simple computational procedure [Eqs. (30)-(36)] has been outlined to transform the failure curve (p_g vs. I/A) for an arbitrary target into the corresponding laser requirements (E_0 vs. τ_p). An illustration of this procedure is presented in Fig. 8. The required laser energy always increases with increasing pulse duration. This is a consequence of the fact that the imparted impulse always decreases with increasing pulse duration. The laser failure criterion has three distinct segments corresponding to the three possible cases. [Note that Case Ia need not exist if the minimum value of I/A for target failure lies in the Case Ic region]. The scaling of the laser energy with the constant α varies in each region. The energy scaling law for Case IIb is a function of the shape of the target failure curve. The energy scales as $1/\alpha$ and $1/\alpha^2$ in Cases Ia and Ic, respectively. The asymptotically derived value of α ($\alpha = 0.6$) is a factor of five smaller than that determined from local analysis ($\alpha \approx 3$). Hence, the laser energy required to induce structural failure of the target may be five or more times greater than that which would be determined using other models. Although the asymptotic value of $\alpha = 0.6$ was confirmed above with momentum transfer data,⁽⁷⁾ its implications with respect to the required laser energy have not been confirmed.

7. CONCLUSIONS

An existing technique⁽¹⁻⁴⁾ of patching blast wave solutions together to describe the pressure field above a laser irradiated target has been modified. The impulse imparted to the target and the laser energy required to impart that impulse is a strong function of the patching times. Local analyses do not uniquely determine these times. In the present work, the conservation of energy is used to determine the patching times in a more rigorous and self-consistent manner (the value of α varies 20% depending upon which property of the blast wave is matched). Results suggest lower impulse per unit energy than previously suggested. The solutions for impulse have been reduced to simple analytic expressions which readily invert target failure criterion (pressure-impulse) into laser requirements (energy, pulse duration, spot size) for target failure.

REFERENCES

1. Pirri, A. N., "Theory for Momentum Transfer to a Surface with a High Power Laser," *The Physics of Fluids*, Vol. 16, Sept. 1973, pp. 1435-1440.
2. Ferriter, N., Maiden, D. E., Winslow, A. M., and Fleck, J. A., Jr., "Laser Beam Optimization for Momentum Transfer by Laser on Supported Detonation Waves," *AIAA Journal*, Vol. 15, Nov. 1977, pp. 1597-1603.
3. Pirri, A. N., Root, R. G., and Wu, P. K. S., "Plasma Energy Transfer to Metal Surfaces Irradiated by Pulsed Lasers," *AIAA Journal*, Vol. 16, Dec. 1978, pp. 1296-1304.
4. Reilly, J. P., Ballantyne, A., and Woodroffe, J. A., "Modeling of Momentum Transfer to a Surface by Laser Supported Absorption Waves," *AIAA Journal*, Vol. 17, Oct. 1979, pp. 1098-1105.
5. Raizer, Yu P., "Heating of a Gas by a Powerful Light Pulse," *Soviet Physics JETP*, Vol. 21, Nov. 1965, pp. 1009-1017.
6. Sedov, L. I., "Similarity and Dimensional Methods in Mechanics," (M. Holt, ed.), Academic Press, New York, 1959.
7. Kozlova, N. N., A. I. Petrukhin, Yu. E. Pleshanov, V. A. Rybakov and V. A. Sulyaev, "Measurement of Recoil Momentum for a Laser Beam Interacting with an Absorbing Surface in Air," Translated from *Fizika Goreniya i Vzryva* 11, 650 (1975), Plenum Publishing Corporation, New York.

ACKNOWLEDGEMENT

Work supported by U. S. Department of Defense, Defense Nuclear Agency,
and monitored by the U. S. Naval Research Laboratory under contract N00014-
81-C-2394.

LIST OF ILLUSTRATIONS

Fig. 1 Solutions for short laser pulses ($\tau_p < R_s/V_w$, Case I).

Fig. 2 Solutions for intermediate laser pulses ($R_s/V_w < \tau_p < R_t/V_w$, Case II).

Fig. 3 Solutions for long laser pulses ($\tau_p > R_t/V_w$, Case III).

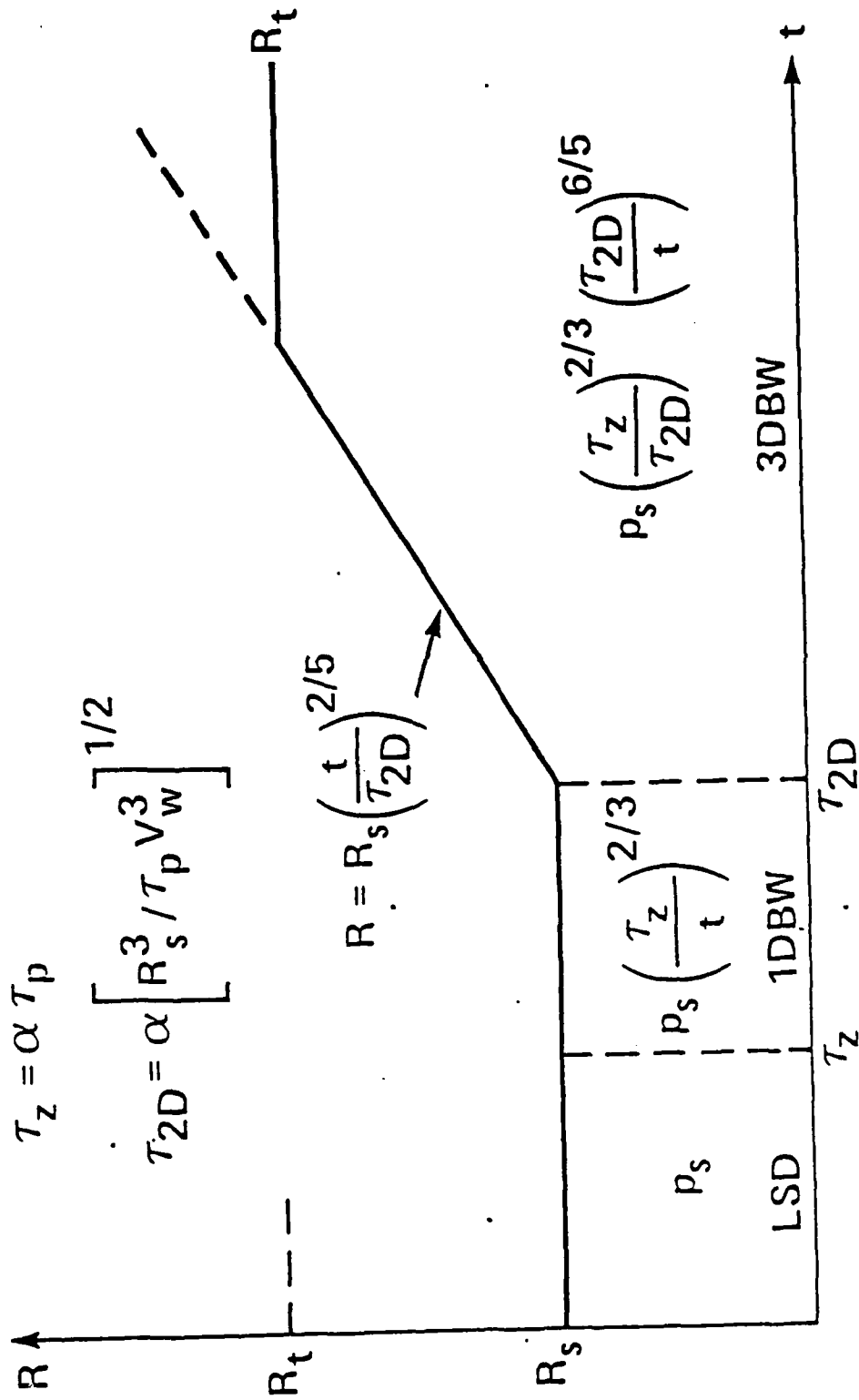
Fig. 4 Range of parameter space appropriate to each solution.

Fig. 5 Comparison of predicted impulse to data⁷ for $\alpha = 0.6$.

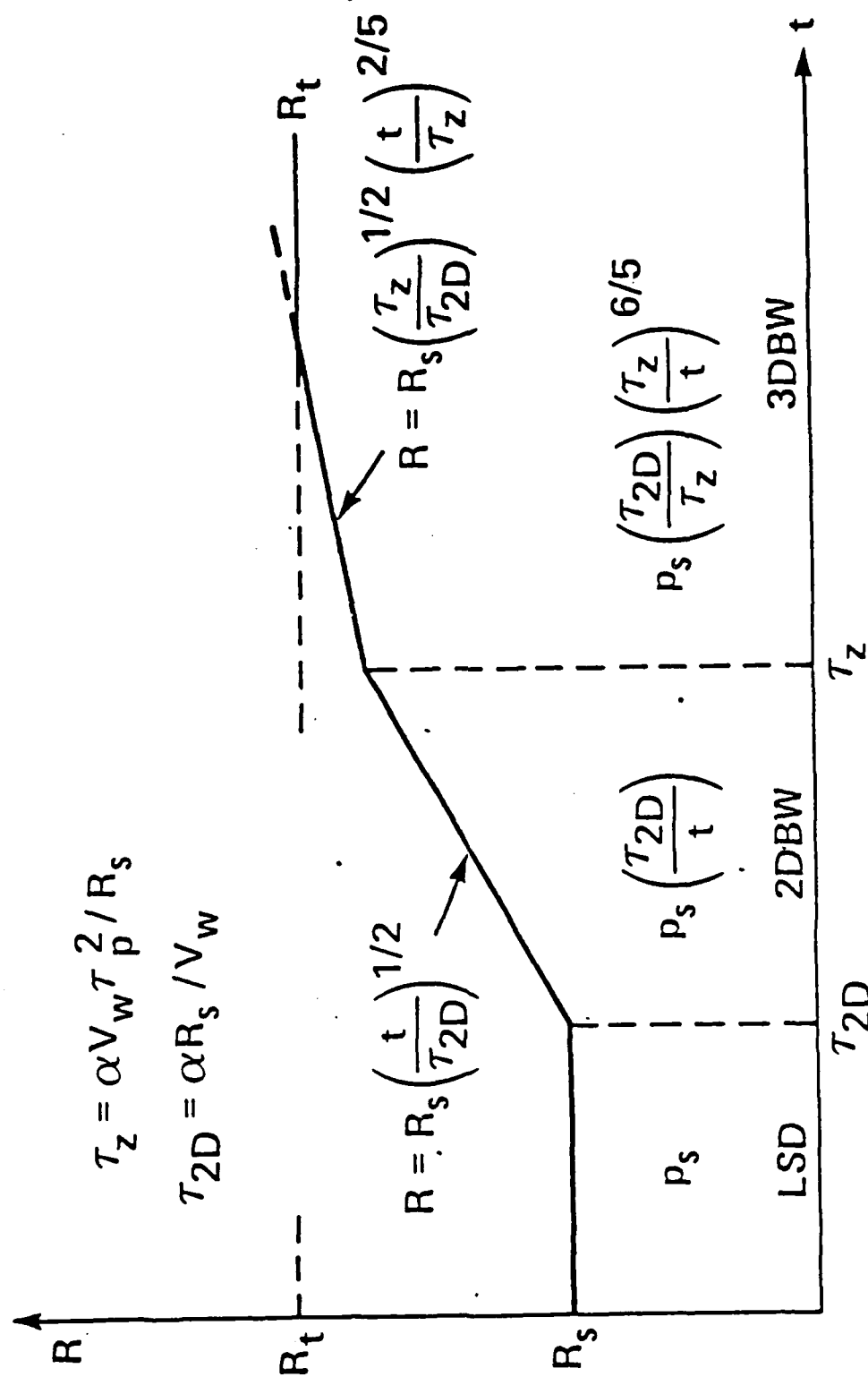
Fig. 6 Impulse imparted by a 10^4 joule laser on 10 cm target.

Fig. 7 Target failure criterion ($R_s = R_t$).

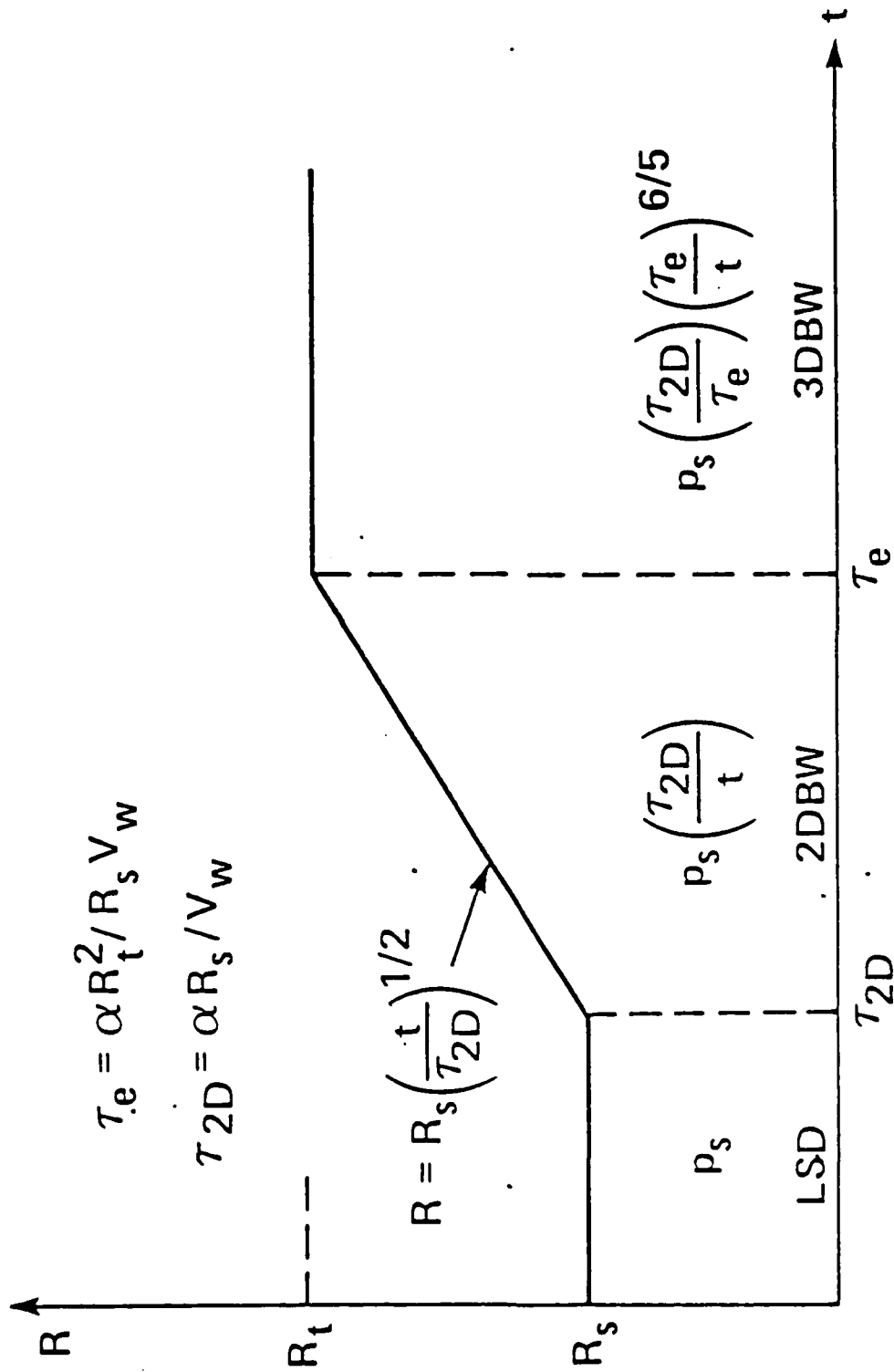
Fig. 8 Laser failure criterion ($R_s = R_t$).



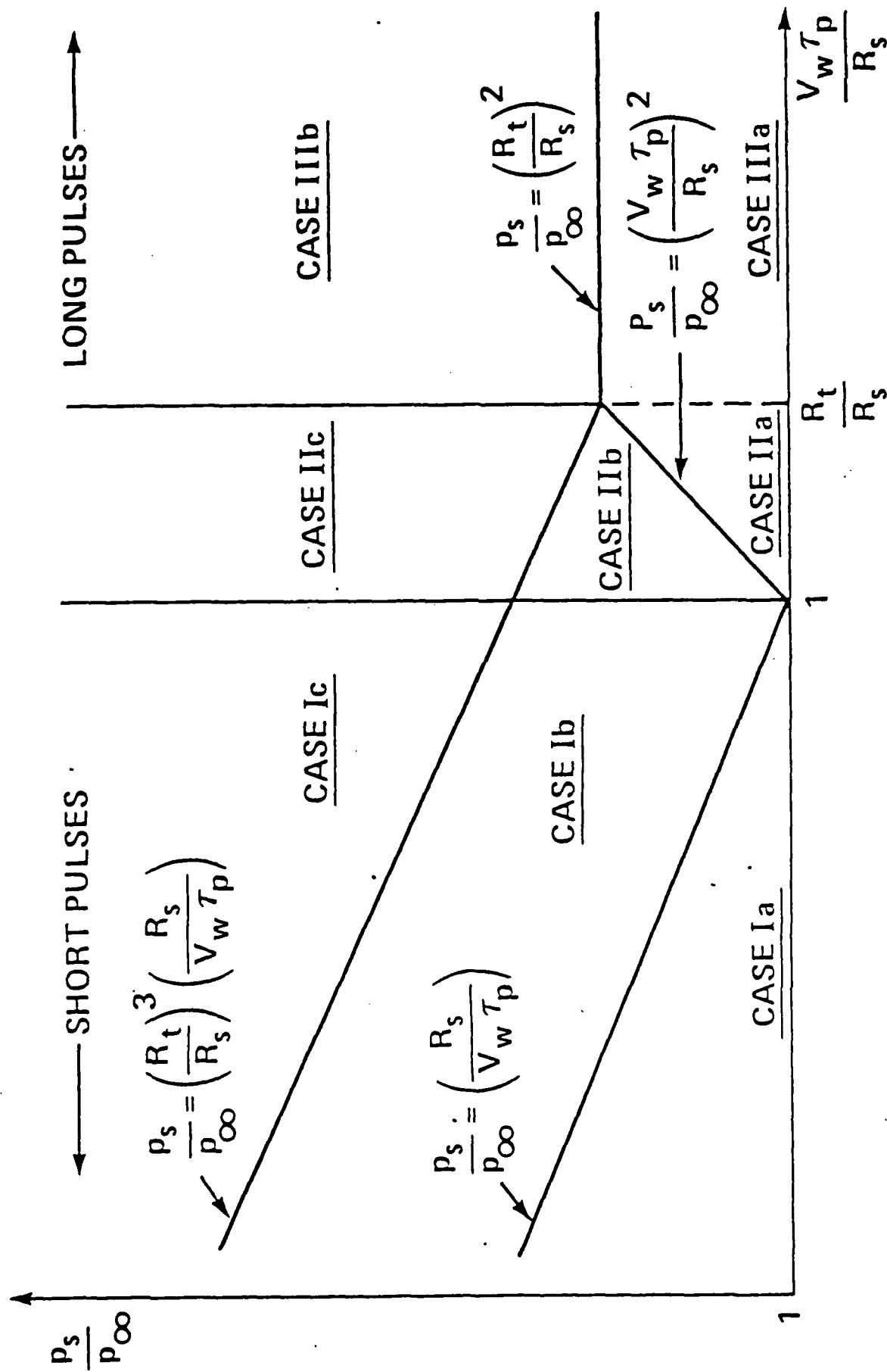
G. Simons
PSI SR-157
Fig. 1



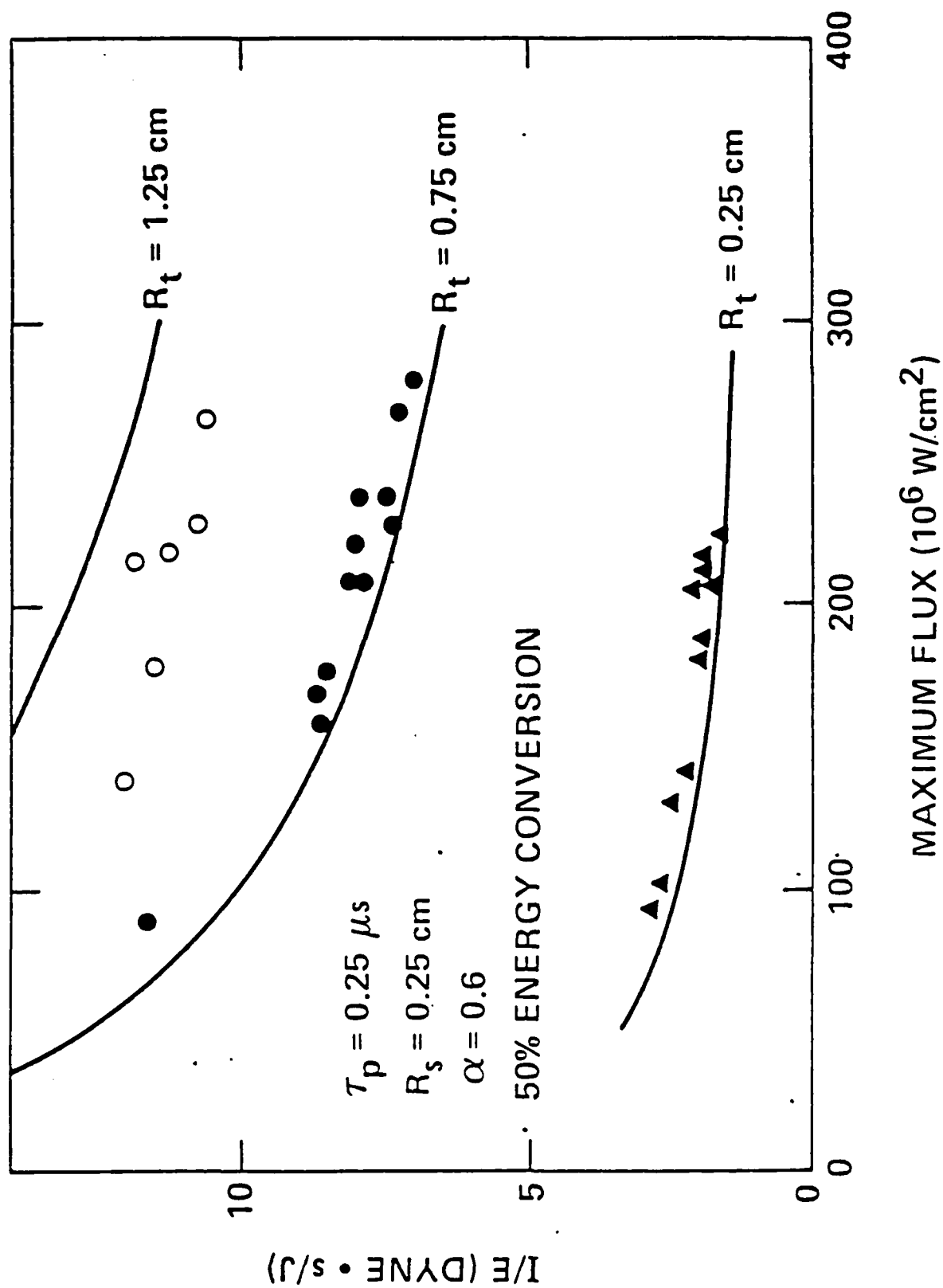
G. Simons
 PSI SR-157
 Fig. 2



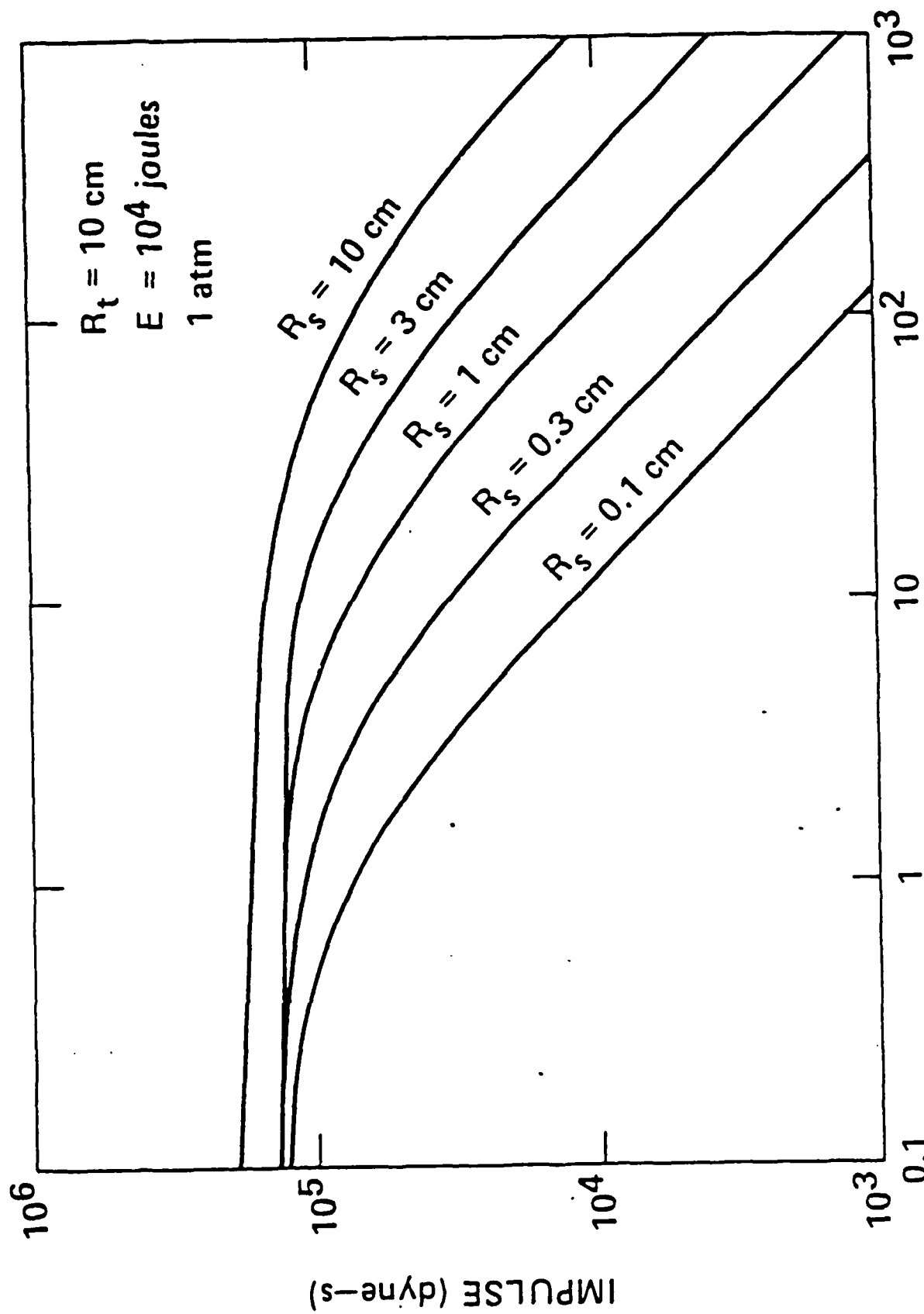
G. Simons
 PSI SR-157
 Fig. 3



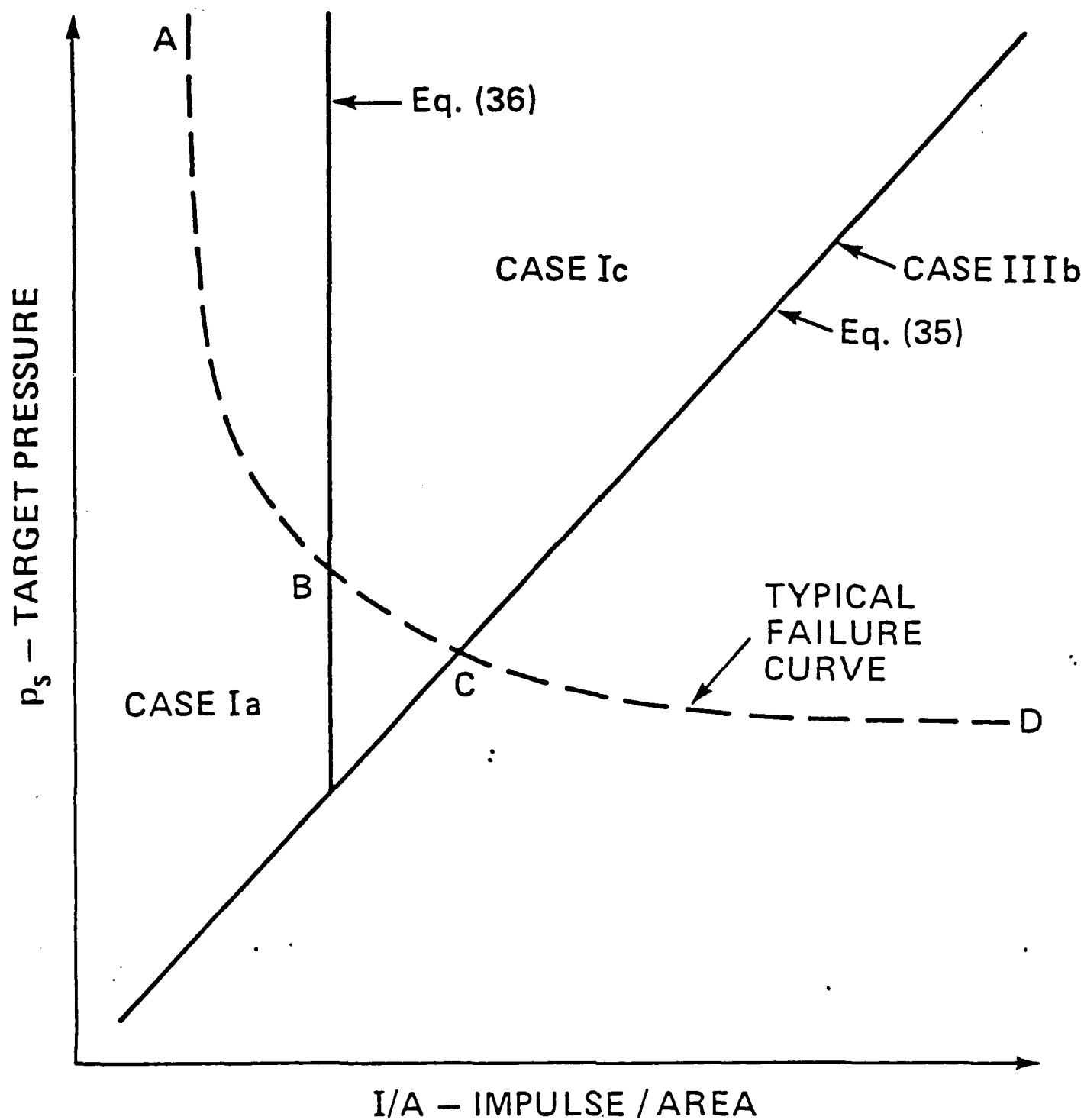
G. Simons
PSI SR-157
Fig. 4

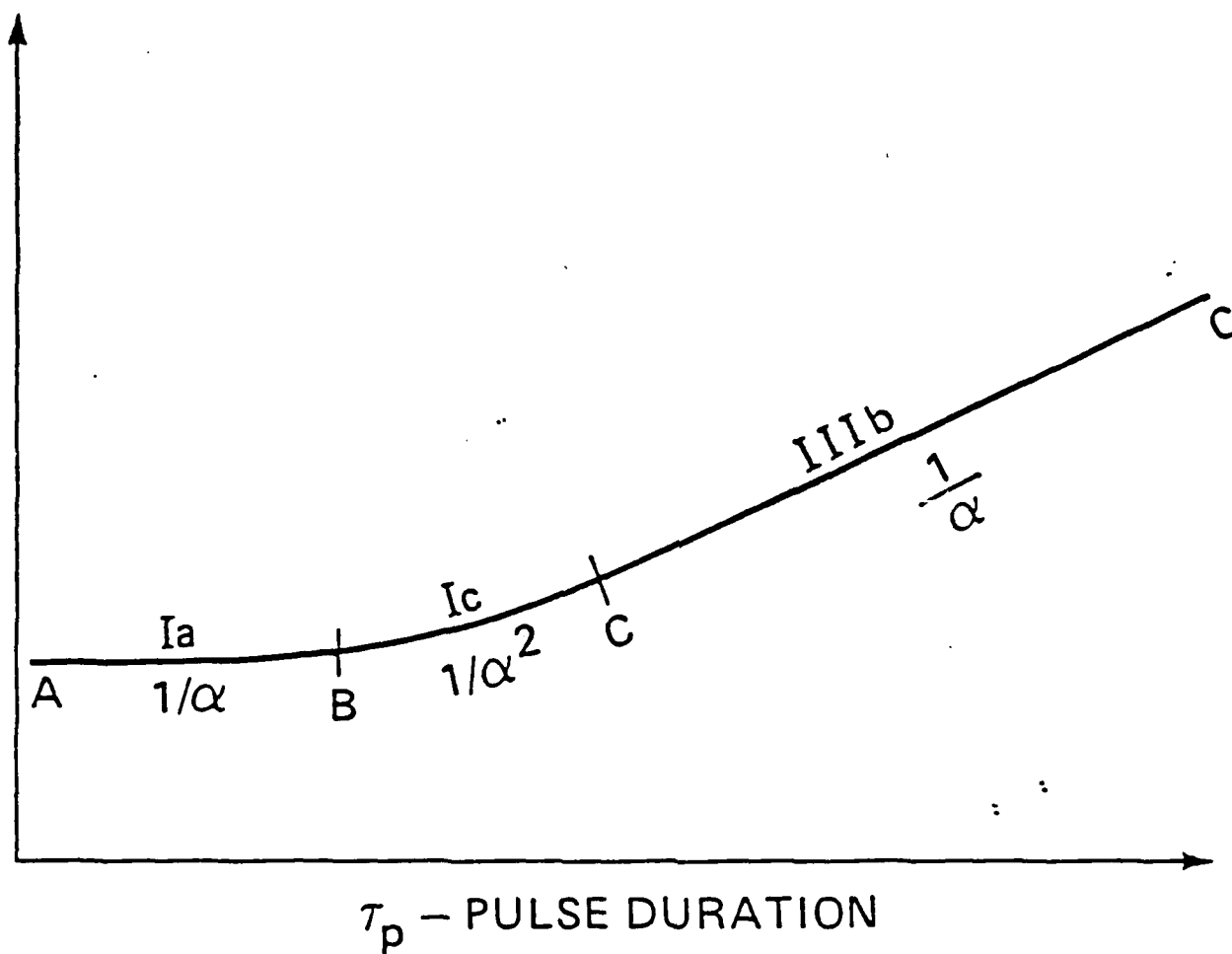


G. Simons
PSI SR-157
Fig. 5



G. Simons
PSI SR-157
Fig. 6





G. Simons
PSI SR-157
Fig. 8